MODELING OF PHOTO-INDUCED DISCHARGE IN AMORPHOUS SEMICONDUCTORS

A Thesis

Submitted to the College of Graduate Studies and Research

in Partial Fulfillment of the Requirements

for the Degree of

Master of Science

in the

Department of Electrical Engineering

University of Saskatchewan

Saskatoon

by

Don Brinkhurst

Saskatoon, Saskatchewan

January, 1998

PERMISSION TO USE

In presenting this thesis in partial fulfillment of the requirements for a Postgraduate degree from the University of Saskatchewan, I agree that the Libraries of this University may make it freely available for inspection. I further agree that permission for copying of this thesis in any manner, in whole or in part, for scholarly purposes may be granted by the professor or professors who supervised my thesis work or, in their absence, by the Head of the Department or the Dean of the College in which my thesis work was done. It is understood that any copying or publication or use of this thesis or parts thereof for financial gain shall not be allowed without my written permission. It is also understood that due recognition shall be given to me and to the University of Saskatchewan in any scholarly use which may be made of any material in my thesis.

Requests for permission to copy or to make any other use of the material in this thesis in whole or in part should be addressed to:

Head of the Department of Electrical Engineering
University of Saskatchewan
Saskatoon, Canada S7N 0W0.

UNIVERSITY OF SASKATCHEWAN

Electrical Engineering Abstract

MODELING OF PHOTO-INDUCED DISCHARGE IN AMORPHOUS SEMICONDUCTORS

Student: Don Brinkhurst Supervisor: Dr. S.O. Kasap

M. Sc. Thesis Presented to the

College of Graduate Studies and Research

January 1998

ABSTRACT

The characteristics of charge transport in amorphous materials are of great importance because they determine the performance of xerographic devices. Transport in amorphous materials is dramatically affected by the presence of localized states in the mobility gap. In order to design efficient photoreceptor materials, a detailed understanding of trapping processes in amorphous materials is required. Considerable work has been performed in this area. However, no complete model for photo-induced discharge in the presence of arbitrary trapping and carrier injection exists.

In this work, a general theoretical model for photo-induced discharge in amorphous materials is developed from the point form representations of Ohm's Law, Gauss' Law, Maxwell's equation for the total current and the trapping rate equation. The rate equation incorporates arbitrary strengths of trapping, release, and trap saturation for a single level of traps. These equations were combined to create a second-order non-linear partial differential equation which governs the behaviour of the electric field during photo-induced discharge.

The differential equation was then solved numerically using boundary conditions which are representative of pulsed-illumination. Solutions were obtained under low injection (0.1%) and high injection (10%, 50%, and 90%) conditions. Trapping parameters which are representative of shallow traps were used. In each case, the mechanics of the simulated discharge were monitored by calculating the trapped and untrapped charge densities at regular intervals throughout the discharge. The rate of change of the surface voltage, dV/dt, was also monitored, because it is an experimentally accessible quantity that provides insight into trapping processes.

Results obtained under low injection conditions demonstrated that the dispersion in the charge packet increased with larger values of the mobility reduction factor θ and smaller values of the trapping and release rates, ω and r. Increased charge packet dispersion was seen to cause increased dispersion in dV/dt near the transit time. The temporal spread of arrival times predicted by the Schmidlin equation was found to be in good agreement with simulation results.

TABLE OF CONTENTS

LIST OF TABLES

LIST OF FIGURES

LIST OF ABBREVIATIONS

a-Se	amorphous selenium
DOS	density of states
FWHM	full-width half-maxima
IFTOF	interrupted-field time-of-flight
K-B	Kanazawa and Batra
PID	photo-induced discharge
TOF	time-of-flight
XTOF	xerographic time-of-flight

1. INTRODUCTION

1.1 Xerographic Process

In the 1930's, only two methods existed for making copies of original documents. The first was to have photographic reproductions made, which was a time-consuming and laborious process. The only alternative was to have manual copies made, which had obvious disadvantages. In the mid 1930's, Chester F. Carlson set out to find an alternative method that would allow copies to be made at low cost and in a short amount of time. His efforts finally met with success on October 22, 1938, when he invented a process that he called "electrophotography" [1]. This process was renamed "xerography" when it was incorporated into the first commercially available copier, the Xerox Copier Model A[1]. Although modern copiers are much more sophisticated, the basic principles of operation have remained the same.

The basic elements of the xerographic process are depicted in Figure 1.1 [2]. The central element of this process is a thin film of photosensitive material on a conducting substrate called the photoreceptor. The basic steps involved in making a copy are described below:

(1) **Sensitization.** The photoreceptor is sensitized by charging the surface with a corona discharge device. This device sprays the surface of the film with positively charged ions. After the charging process is complete, the field within the film has been raised to approximately 10^5 V/cm.

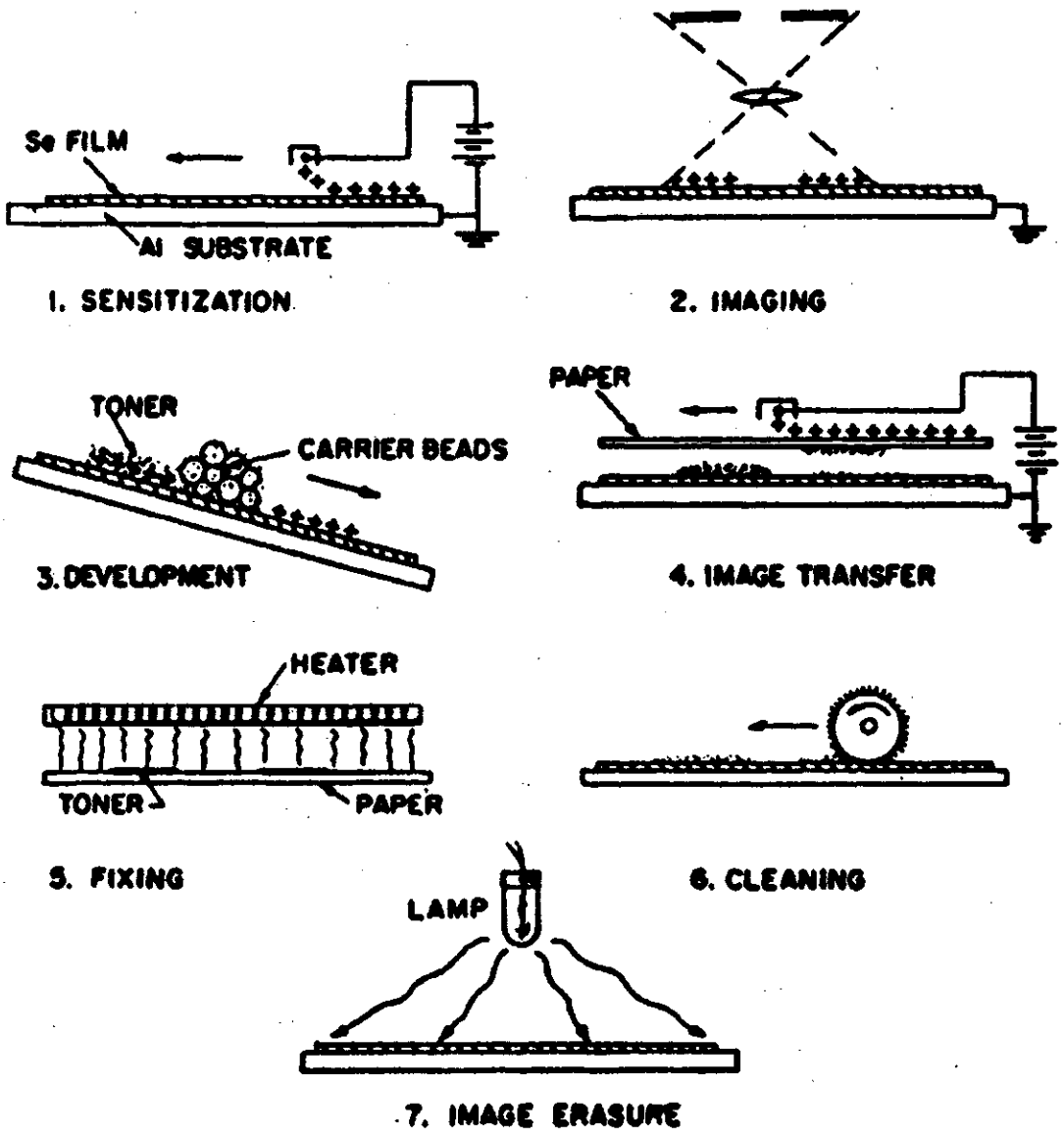

Figure 1.1. Basic Elements of the Xerographic Process (after [2]).

(2) **Exposure.** The original document is projected onto the surface of the photoreceptor. Wherever light strikes the surface, the local conductivity in the film is increased and current flows normal to the surface. This reduces the surface potential in the regions that have been exposed. As a result, an electrostatic image of the original document is created on the photoreceptor.

(3) **Development.** The electrostatic image is developed by spreading a mixture of toner and carrier beads over the surface of the film. The toner particles are triboelectrically charged and are attracted to the areas of the surface that have a high potential, i.e. where light did not strike the surface.

(4) **Transfer.** The paper is positively charged with another corona discharge device. The toner particles are attracted to the paper, and hence are transferred from the surface of the film to the surface of the paper.

(5) **Fixing.** The toner is fixed to the surface of the paper. This is done through the application of heat, heat and pressure, or solvent vapors.

(6) **Cleaning.** Any toner that remains on the surface of the photoreceptor is removed by cleaning the surface of the film. This is performed through mechanical or electrostatic techniques.

(7) **Erasure.** The electrostatic image remaining on the photoreceptor is erased by exposing the surface to intense light. At this point, the photoreceptor is ready for the next cycle.

It is evident that the photoreceptor plays a critical role in the xerographic process.

1.2 Properties of an Ideal Photoreceptor

The purpose of the photoreceptor is to convert an optical image projected onto its surface into an electrostatic image. In order for a photoreceptive material to be useful in the xerographic process, its properties must approximate those of an ideal photoreceptor, which are summarized below [2,3].

(1) The surface voltage is linearly related to the surface charge density with the capacitance per unit area being the constant of proportionality.

(2) Every photon striking the surface causes one unit of charge to be removed from the surface and transported through the entire thickness of the film to the substrate. Together with property (1), this guarantees that the drop in the surface potential is linearly related to the exposure, as illustrated in Figure 1.2. This is a desirable characteristic because the amount of toner deposited is linearly related to the surface potential [3]. Therefore, the ideal photoreceptor guarantees that the original image density is recreated in the copy.

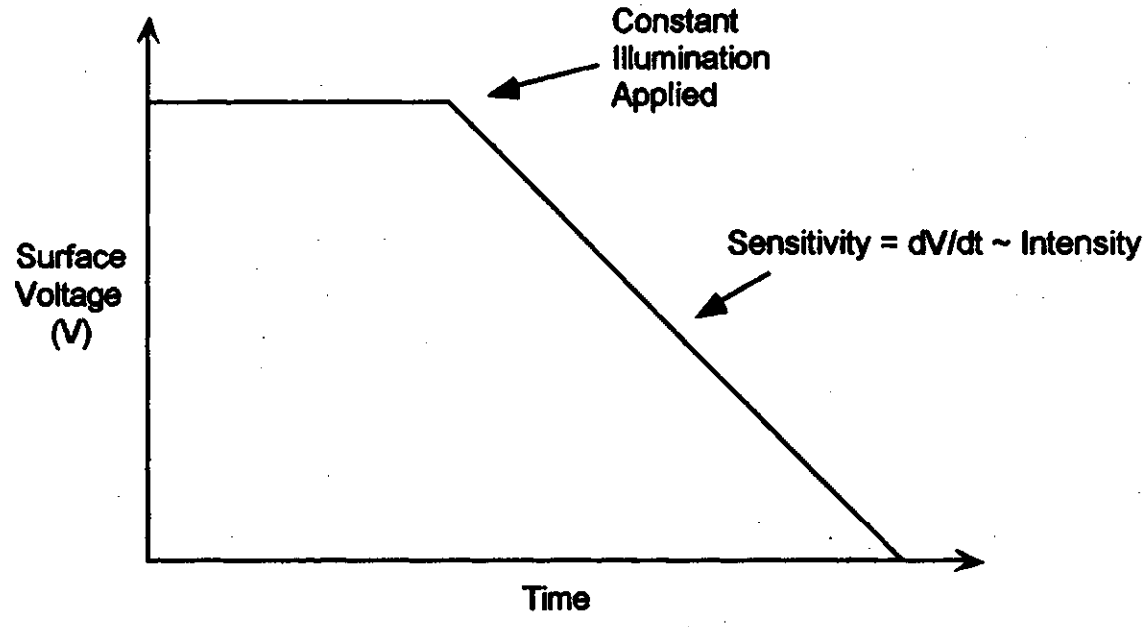

Figure 1.2. Ideal Photoreceptor Response (after [3]).

(3) The only mobile carriers are photogenerated, i.e. there are no thermally generated carriers. This prevents the electrostatic image from decaying in the absence of light between the sensitization, imaging and development steps.

(4) The positive charge lying on the surface cannot enter the bulk or move laterally on the surface. This property also prevents the electrostatic image from changing in the absence of light.

(5) The properties of the photoreceptor do not change with cycling, allowing the photoreceptor to be used repetitively.

(6) The photoreceptor must be able to be manufactured reliably. It must be manufacturable over areas comparable to the size of the original document. The properties of the film must not vary over the surface.

Practical photoreceptors approach these properties only approximately and over a limited usage time (e.g. 10^5 copies for an amorphous selenium photoreceptor, and 10^4 copies for an organic photoreceptor.)

1.3 Practical Photoreceptors

The most obvious requirement of a practical photoreceptor is basic photoconductivity. Crystalline semiconductors are well known for having photoconductive properties, but are unsuitable for use in xerographic applications because it is infeasible to grow large document-sized crystals. Amorphous semiconductors that exhibit photoconductive properties are well suited to xerographic applications because they have a disordered structure. This absence of a regular structure allows amorphous semiconductors to be grown in large areas of arbitrary shape with much less stringent growth conditions [1].

Another advantage of amorphous semiconductors is that they have high resistivities in comparison with their crystalline counterparts. Amorphous selenium has a dark resistivity of greater than 10^{14} Ω-cm, whereas the crystalline forms of silicon only

have dark resistivities on the order of 10^4 Ω-cm. As a result of its high resistivity, it takes several minutes (e.g. 30 min.) for a charged a-Se photoreceptor to decay to half-potential in the absence of light [4]. This extremely slow rate of decay allows the photoreceptor to remain charged between the sensitization and exposure phases.

During the exposure phase, the function of the photoreceptor is to discharge the surface in regions where light strikes the surface, creating an electrostatic image. This process can be broken down into two basic steps: photogeneration and transport, as depicted in Figure 1.3.

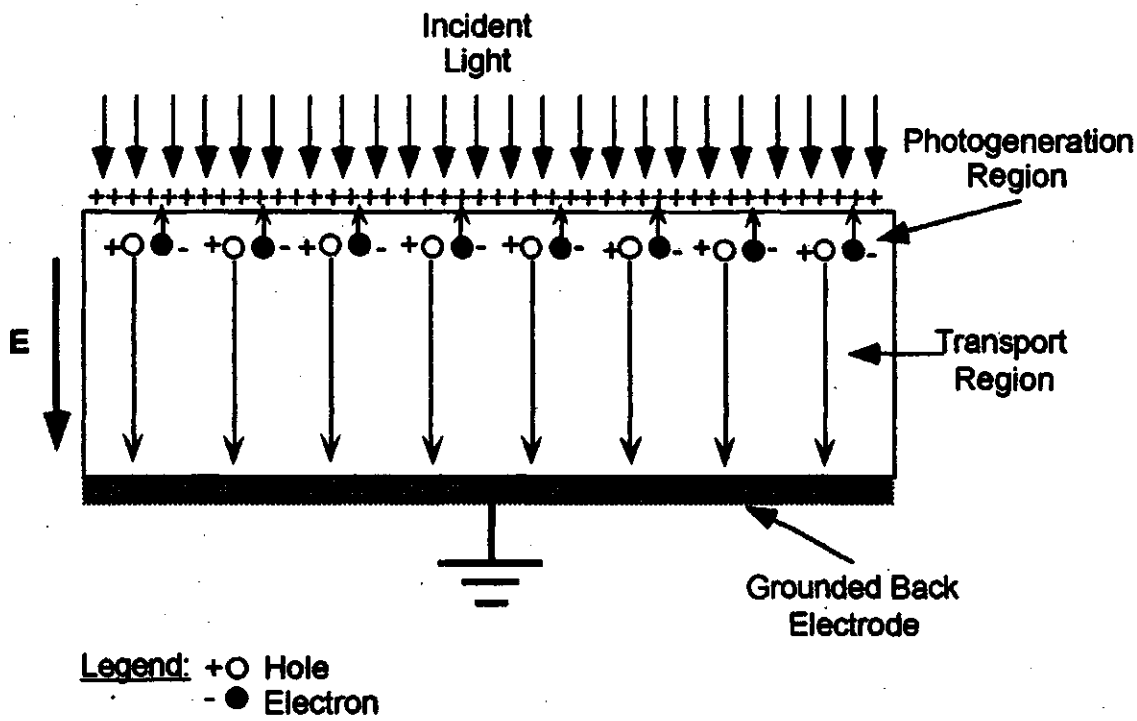

Figure 1.3. Photogeneration and transport during xerographic discharge.

In the photogeneration process, incident photons are converted into mobile carriers. Ideally, the photogeneration process would be 100% efficient over all wavelengths, with one carrier generated for each incident photon striking the surface. Of

course, this is not the case in any practical photoreceptor. In amorphous selenium, the range of usable photogeneration extends from about 550 nm and into the ultraviolet [4]. For wavelengths where strong photogeneration occurs, the incident light is absorbed in a thin region near the surface[4], and mobile carriers are created within this region. Outside of this wavelength range, the light passes through the material and no appreciable amount of photogeneration takes place. This photosensitivity range is useful for copying black or grey originals, but is not suitable for copying coloured originals. Considerable work has been done in attempt to alleviate this problem, including investigations involving different photoreceptor structures and materials.

The second basic step of the exposure process involves the transport of the photogenerated carriers across the thickness of the film to the substrate. The photogenerated carriers are created in electron-hole pairs (see Figure 1.3). Once created, the electron and hole carriers start to drift under the influence of the electric field resulting from the sensitization process. The electrons drift towards the surface and reduce the positive surface charge placed there during the sensitization process. The holes drift across the film towards the substrate. Since the electron-hole pairs are created in a thin region near the surface, the electrons only have a short distance to travel until they reach the surface. The holes must travel all the way across the film until they reach the substrate. Once the hole has reached the substrate, one unit of charge has effectively been removed from the surface, thereby discharging the photoreceptor.

The speed of the discharge is limited by either photogeneration or transport, whichever is slower. If the rate of discharge is limited by the rate of photogeneration , the discharge is said to be "injection limited". If the rate of discharge is limited by the transport process, the discharge is said to be "transport limited". In many practical xerographic systems, including laser printers, the photoreceptor is illuminated with a

short, intense flash of light of a duration which is shorter than the time it takes for the holes to traverse the sample. Therefore, in many practical xerographic systems, the discharge is transport limited. Since holes have the greatest distance to travel, the efficiency of hole transport in the photoreceptor dominates the characteristics of the discharge.

In an ideal photoreceptor, the photogenerated holes would drift across the thickness of the film in zero time, and the rate of discharge would only be limited by the rate of photogeneration. If an amorphous semiconductor is used as the photoreceptor material, there are two basic factors that limit the efficiency of the transport process. The first limiting factor is the drift mobility, or simply mobility. The mobility, μ_0, is defined as drift velocity, v_d, per unit applied electric field, E, i.e.

$$\mu_0 = v_d/E \tag{1.1}$$

The mobility of holes in a-Se is approximately 10^{-1} cm^2/Vs, which is orders of magnitude lower than the mobilities of the charge carriers in copper ($\sim 10^1$ cm^2/Vs) and crystalline silicon (10^3 cm^2/Vs)[1].

The mobility of charge carriers in a material sets the value of a key xerographic parameter, called the transit time, that can be derived as follows:

$$t_0 = \frac{L}{v_d} \tag{1.2}$$

$$v_d = \mu_0 E = \frac{\mu_0 V_0}{L} \tag{1.3}$$

$$t_0 = \frac{L}{\mu_0 V_0 / L} = \frac{L^2}{\mu_0 V_0} \tag{1.4}$$

where L = photoreceptor thickness

V_0 = initial photoreceptor voltage

The transit time is useful as a first estimate of the time it takes for the photoreceptor to discharge during the exposure stage. Consider an a-Se photoreceptor of 50 μm thickness that has been charged to a voltage of 500 Volts during the sensitization process. Using the mobility for a-Se, the transit time in this scenario is:

$$t_0 = \frac{(500\ \mu m)^2}{(0.1\ cm^2/Vs) \times (10^4 \mu m/1\ cm)^2 \times 500\ V} = 0.5\ \mu s \qquad (1.5)$$

From this calculation, we can see that it would take around 0.5 μs for this photoreceptor to discharge. This value in itself is acceptable because the time between the exposure and development phases is generally larger than this value.

The effective carrier transit time and the resulting discharge time is actually much longer than the value determined by the mobility, due to an effect that is unique to amorphous solids. The disordered nature of these materials allows for many different kinds of defects. Unsatisfied or dangling bonds and other kinds of defects exist with densities that are high enough to significantly degrade the transport process. These defects can capture mobile carriers, effectively removing them from the conduction process. This process known in the literature as "trapping", and the corresponding defects are known as trapping centers or "traps". This effect drastically alters the characteristics of the discharge.

Traps are generally categorized into two different types: shallow and deep. If the carriers remain trapped for a time that is much shorter than the transit time, the carriers are called "shallow traps". The effect of these traps is to reduce the apparent mobility, thus increasing the transit time and the time scale of the discharge. In the case of deep traps, the carrier remains captured in the defect for a time that is much longer than the transit time. This carrier is permanently trapped when viewed against the time scale of

the discharge. As a result, a fraction of the carriers created near the surface are permanently trapped in the bulk and never reach the back electrode. A consequence of this is that the photoreceptor is not completely discharged, because a complete discharge would involve transferring all of the surface charge through the bulk to the back electrode. Instead, the photoreceptor decays to a voltage called the "residual potential". This residual potential accumulates every time the photoreceptor is cycled as more and more charge is trapped in the bulk. Practical photoreceptors must have small residual potentials in order to be useful.

1.4 Thesis Objectives

The photoreceptor plays a key role in the xerographic process. In order to operate efficiently, any practical photoreceptor must at least approximate the qualities of the ideal photoreceptor. We have seen how the processes of photogeneration and transport deviate from the ideal case and how this affects the performance of a practical photoreceptor. The characteristics of transport are of particular interest, because they play a part in determining the speed and efficiency of the discharge.

When amorphous semiconductors are used as the photoreceptor material, transport is greatly affected by trapping as the carriers travel through the bulk. Clearly, the effects of trapping need to be taken into account when designing efficient photoreceptors. In order to achieve this goal, a detailed understanding of the trapping process is required. Considerable work has been done in this area over the last 30 years, and many different models have been devised that deal with various aspects of trapping[7,8,9,10,11]. However, not many complete models exist that allow one to investigate the effects of the various trapping parameters on the discharge. The complexity of the complete problem creates complicated non-linear differential

equations which cannot be solved analytically. Researchers in the past had to settle for incomplete or simplified models that could be solved analytically with relative ease.

It is clear that a comprehensive model of photo-induced discharge in the presence of trapping effects is needed. The purpose of this work was to:

(1) Develop a detailed mathematical description of photo-induced discharge that includes the effects of trapping,

(2) Derive a general partial differential equation that describes the discharge kinetics from the mathematical description obtained in (1),

(3) Construct a set of boundary conditions that reflect a range of conditions that can occur in xerographic systems,

(4) Describe a numerical method that can be used to obtain a solution to the differential equation under specified boundary conditions,

(5) Solve the differential equation under a variety of trapping characteristics and boundary conditions, and

(6) Discuss the significance of the results and compare them with those obtained from previous models.

2. ELECTRONIC BAND STRUCTURE OF AMORPHOUS SOLIDS

2.1 Introduction

In order to understand and model the transport processes that occur in amorphous semiconductors during xerographic discharge, a suitable theoretical framework is required. In the early 1930's, quantum mechanics was applied to the problem of crystalline solids, giving rise to the band theory of solids. The band theory was the first theory that was able to explain the existence of the three main classes of solids: metals, insulators, and semiconductors. The band theory was also able to explain a broad range of phenomena that occurred in these devices, including one of specific interest to us: photoconductivity[1].

2.2 Atomic Structure

In order to develop a detailed band model for a particular type of solid, one must have detailed knowledge about its atomic structure. The structure of amorphous semiconductors is best described in comparison with the idealized structure of crystalline semiconductors. A two-dimensional representation of the structure of crystalline and amorphous solids is shown in Figure 2.1. The black dots in the figure represent the equilibrium positions of the atoms. Three important statements about the structure of amorphous solids can be made (refer to Figure 2.1):

(1) In the crystal, the bond angles are all identical, causing the structure to be periodic. In contrast, the bond angles and lengths in the amorphous solid are slightly distorted, destroying long-range order.

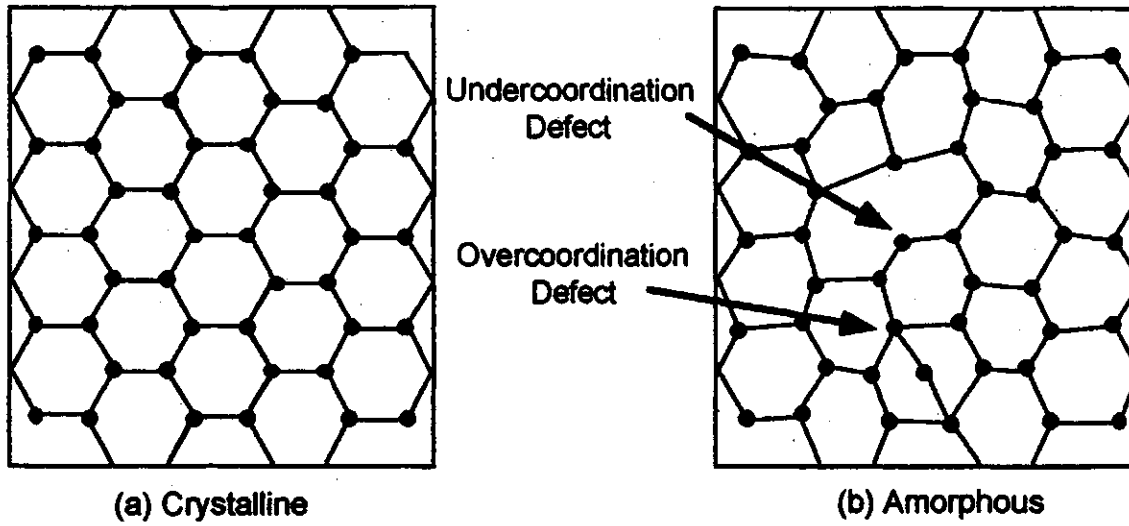

Figure 2.1. Structure of Crystalline and Amorphous Solids.

(2) In the crystal, the nearest neighbor environment of each atom is identical. In the amorphous solid, the nearest neighbor environment of a large percentage of the atoms is essentially the same and short-range order is preserved [2]. The short-range environment of the amorphous solid is basically the same as its crystalline counterpart.

(3) In the amorphous solid, some of the atoms can also be over- or under-coordinated, causing defects. The disordered structure of the amorphous solid allows for a relatively high density of these defects in comparison with the crystalline case.

These basic features of atomic structure in amorphous solids have a profound effect on their electronic band structure, which in turn greatly affects transport in these solids.

2.3 Electronic Band Structure and Density of States

The band theory of solids is, in essence, the quantum theory of electron behavior in solids. According to the band theory, the regular atomic structure of the solid causes the allowable electron energies to be arranged into energy bands. These bands can be described quantitatively through a function called the density of states (DOS). This quantity, denoted g(E), describes the number of electron states per unit energy per electron at energy E. The density of states for the case of a crystalline semiconductor is depicted in Figure 2.2. In this figure, there are two principal bands, the valence and conduction bands, which are separated by a band gap. The detailed structure of the density of states in a material, coupled with the theory of electron statistics, plays a large role in determining its electronic properties.

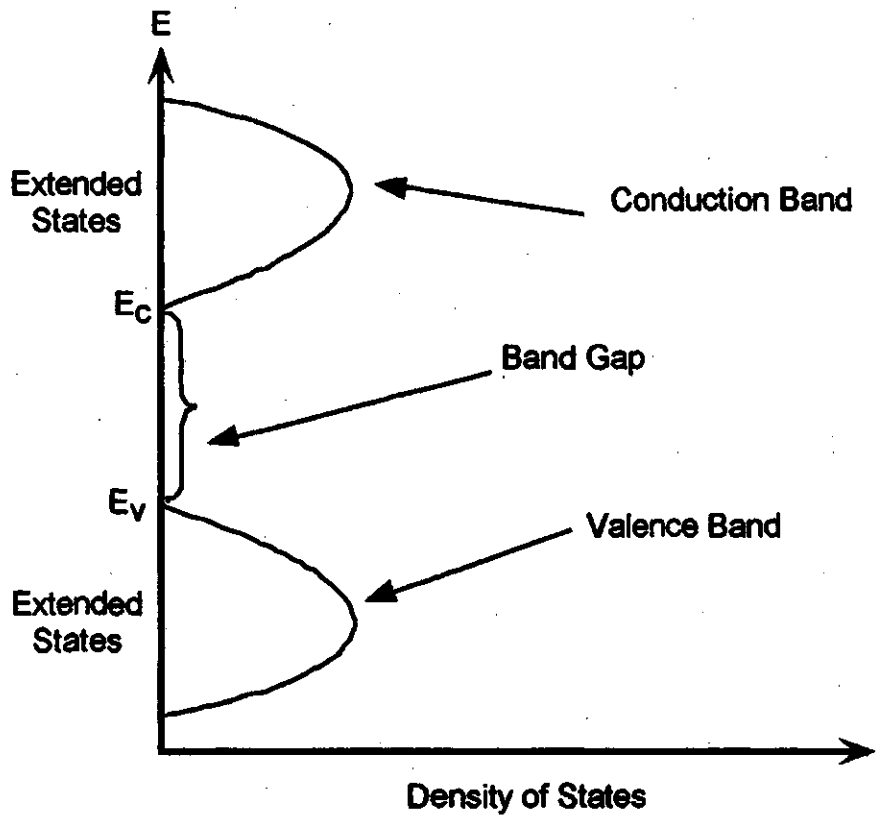

Figure 2.2. Density of States in a crystalline semiconductor.

The band theory was originally developed for the case of crystalline solids, where the rigid periodicity was used to simplify the mathematics of the theory. For some time, it was thought that the band theory did not apply to amorphous solids because these materials do not exhibit long range order. This opinion was later abandoned when amorphous solids were found to have the same basic electronic and optical properties as their crystalline counterparts[2]. It was concluded that only short range order is required for the band theory to be applicable.

The disordered structure of amorphous solids has a profound effect upon the density of states[2]. The accepted view of the density of states in a amorphous semiconductor, such as amorphous selenium, is depicted in Figure 2.3[1].

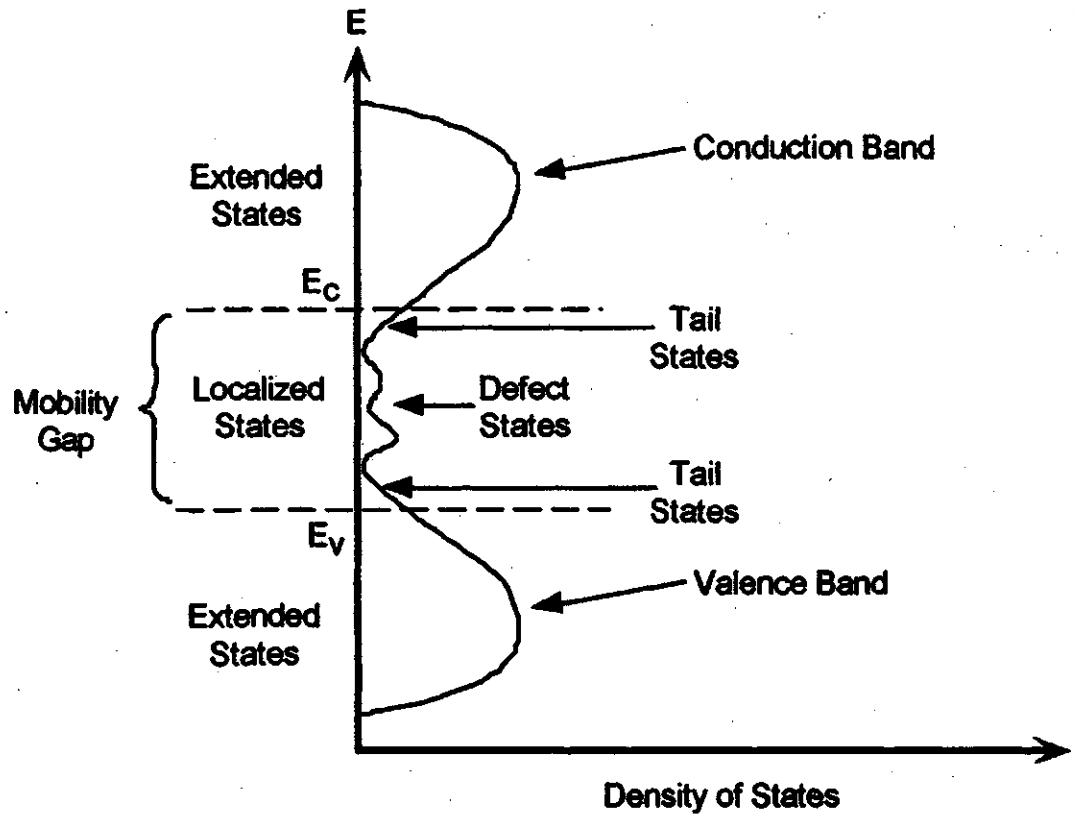

Figure 2.3. Density of States in an Amorphous Semiconductor.

Note that the basic aspects of the DOS are similar to those of a crystalline semiconductor. The two bands of states, the conduction and valence bands, are still present. The similarities vanish when one looks at the region of the DOS between the bands. In the crystalline case, the DOS in this region is identically equal to zero. In the amorphous case, the density of states in the gap is small but finite. The mobility of electrons in these gap states is much lower than in the valence and conduction bands. This greatly reduced mobility is due to the fact that the gap states are localized in space; i.e. an electron occupying such a state is not free to move throughout the solid. The small amount of conduction that occurs here is solely due to hopping between localized states. The states comprising the conduction and valence bands are not localized but are extended throughout the solid, and therefore have much higher mobilities. These two classes of states are referred to as "localized states" and "extended states". The region of reduced DOS and mobility between the bands is called the "mobility gap" in an amorphous semiconductor because of the dramatic reduction in mobility. The term "band gap" is not strictly correct because the DOS is not zero.

The localized states in the mobility gap can be divided into two basic categories: tail states and defect states (see Figure 2.3). The tail states occupy the regions near the edge of the valence and conduction bands. The defect states lie deep within the mobility gap. These two categories derive from different aspects of the atomic structure. Tail states are the result of a phenomenon called Anderson localization. In an amorphous solid, the bond angles are slightly distorted and long-range order is destroyed. Theoretically, the electrons can be viewed as being surrounded by a randomly perturbed periodic potential. Anderson [5] demonstrated that under these conditions, tails of localized states are created at the band edges. A critical energy exists (E_v and E_c), where the states change from being extended to being localized. These points mark the edges of the mobility gap where the mobility drops sharply.

Defect states, as the name implies, are created by the presence of over- and under-coordination defects. In a crystalline solid, these defects create discrete energy levels in the band gap. In an amorphous solid, however, the defects are surrounded by a random distribution of host atoms. This causes the discrete defect energy levels to be smeared, creating maxima in the DOS deep in the mobility gap (see Figure 2.3) [1]. The presence of large densities of localized states in the mobility gap of amorphous semiconductors has a profound effect on transport in these materials.

2.4 Transport in Amorphous Semiconductors

The modern theory of conduction in amorphous semiconductors can be explained in terms of the band theory. Both the extended and localized states play a central role in determining the nature of transport in these materials.

2.4.1 Conduction in the Extended States

In most solids, conduction primarily takes place in the extended states. In a semiconductor, both the valence and conduction bands play a role. The conductivity in the extended states for a semiconductor can be calculated from the general equation:

$$\sigma = en\mu_e + ep\mu_h \tag{2.1}$$

where e = electron charge
n = free electron concentration in the conduction band
p = free hole concentration in the valence band
μ_e = electron mobility
μ_h = hole mobility

In the absence of light, free electrons and holes are created through a process called thermal generation. In this process, the thermal vibrations of the lattice cause electrons to be excited out of the valence band into the conduction band, creating free electron-

hole pairs. The concentration of thermally generated electron-hole pairs can be determined from Fermi-Dirac statistics and the density of states, as depicted in Figure 2.4.

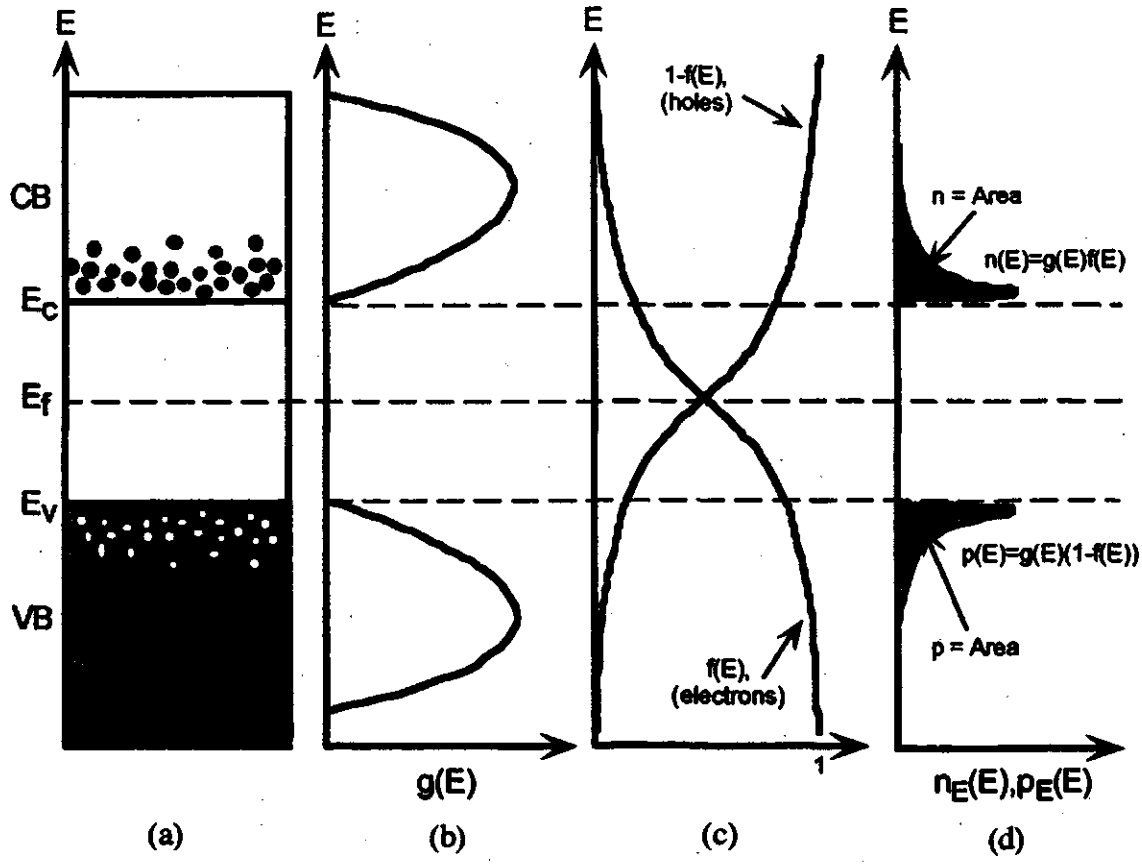

Figure 2.4 Thermal Electron Occupancy in a Semiconductor (after [6])
(a) Schematic Representation
(b) Density of States, g(E)
(c) Probability of occupancy given by Fermi-Dirac Distribution
(d) Electron and Hole Concentrations

In the case of photoconductivity, photons incident on the material excite electrons from the valence band into the conduction band, as shown in Figure 2.5. This process creates electron-hole pairs and thereby increases the free hole and electron densities.

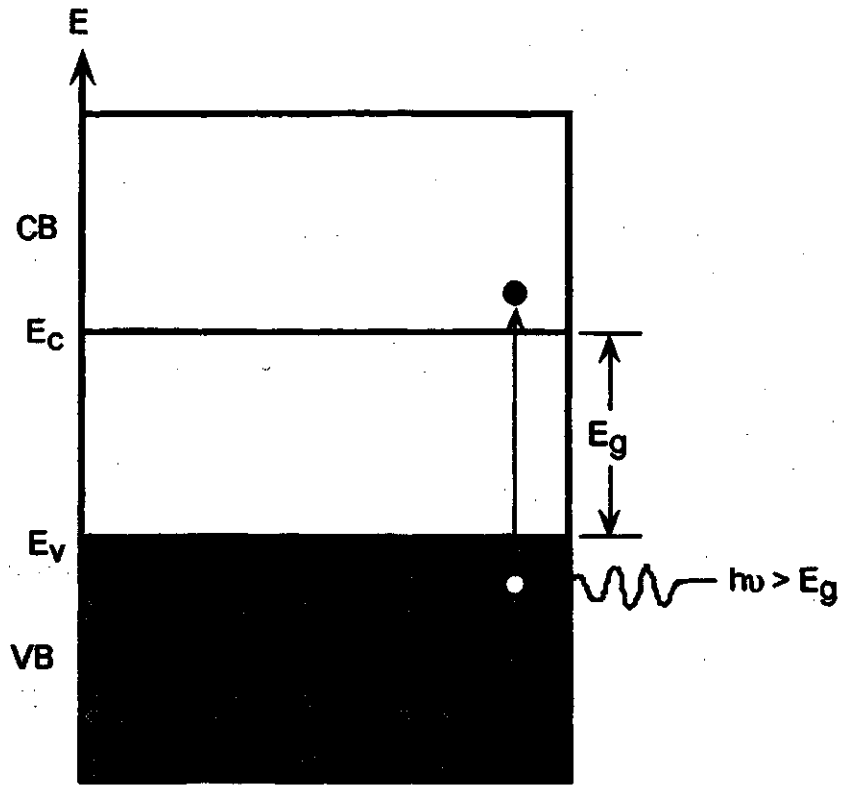

Figure 2.5. Photogeneration of Electron-Hole Pairs.

Free electron-hole pairs, once created, can drift under the influence of an applied electric field, as depicted in Figure 2.6. The holes drift with the electric field; the electrons drift against it. The applied electric field causes the energy band diagram to be "bent" since the electron potential energy increases in the direction of the electric field. For simplicity, this aspect of the band diagram is not shown in Figure 2.6.

The resulting conduction current density is given by the following relation:

$$J = \sigma E = (en\mu_e + ep\mu_h)E = env_e + env_h \qquad (2.2)$$

where $v_e = \mu_e E$ = electron drift velocity

$v_h = \mu_h E$ = hole drift velocity

From this relation, it is evident that the hole and electron mobilities are the second quantity, in addition to the carrier concentrations, that affect the magnitude of the

conduction current. The electron and hole mobilities are limited by the mean time between carrier scattering events (e.g. from lattice vibrations and defects). In amorphous solids, this time is much shorter than in crystalline solids, due to significant scattering from random potential fluctuations. As a result, the mobility in amorphous solids is several orders of magnitude lower than in crystalline solids. For example, the mobility of holes in amorphous selenium is approximately 10^{-1} cm^2/Vs, whereas the mobility of crystalline silicon is around 10^3 cm^2/Vs.

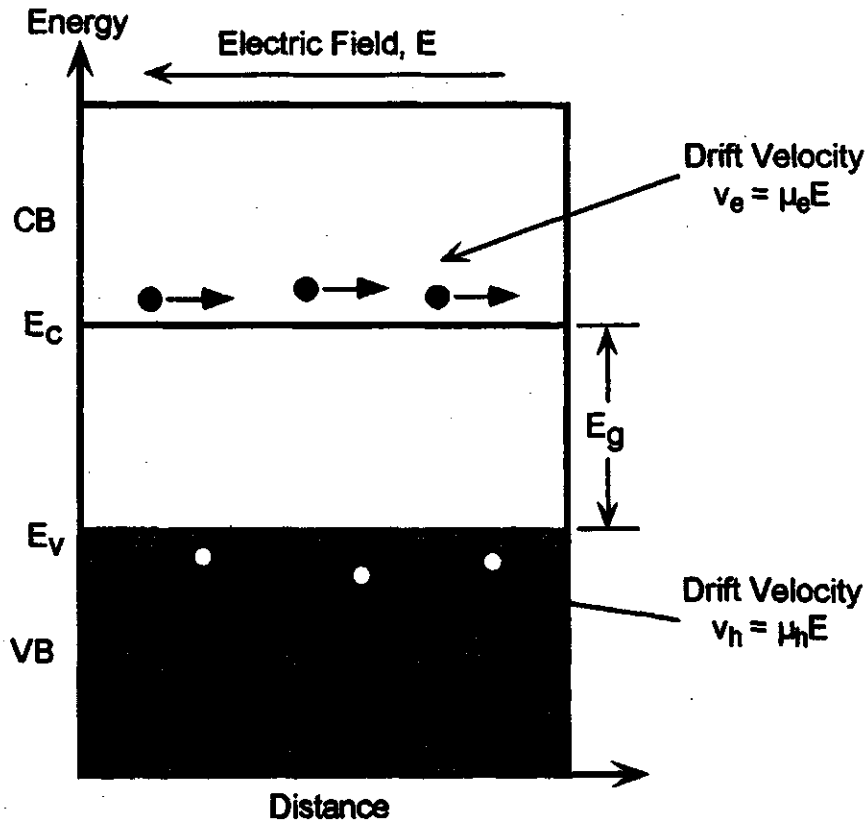

Figure 2.6. Electron and Hole Drift. Band bending caused by the applied electric field is not shown.

2.4.2 Role of Localized States

Conduction in amorphous solids is greatly affected by the presence of significant densities of localized states located in the mobility gap. These states can act as trapping centers that can capture free carriers drifting in the extended states. Strictly speaking, the free carriers interact with a continuum of localized states located in the mobility gap. For the purposes of a discussion of trapping effects, however, it is useful to classify the localized states into two categories: shallow tail states and deep defect states.

Associated with each of these categories are two sets of traps, one for electrons drifting in the conduction band and another for holes drifting in the valence band. This creates four different types of traps, as shown in Figure 2.7. Electrons drifting in the conduction band can become trapped by shallow and deep traps located below the band. A similar situation exists for holes drifting in the valence band. Associated with each set of traps is a capture and release lifetime. The capture lifetime is defined as the mean time that a mobile carrier can drift in the extended states before becoming trapped. The release lifetime is defined as the mean time that a mobile carrier will remain in a trap before being released back into the extended states. These capture and release lifetimes define the dynamics of the trapping process.

The capture process is controlled by the same mechanism that controls scattering of charge carriers[6]. Therefore, the capture lifetime of a given trap type is defined by the relation

$$\tau_c = \frac{1}{\sigma v_{th} N_{avail}} \tag{2.3}$$

where σ = capture cross-section

v_{th} = thermal carrier velocity

N_{avail} = concentration of available or unfilled trapping centers

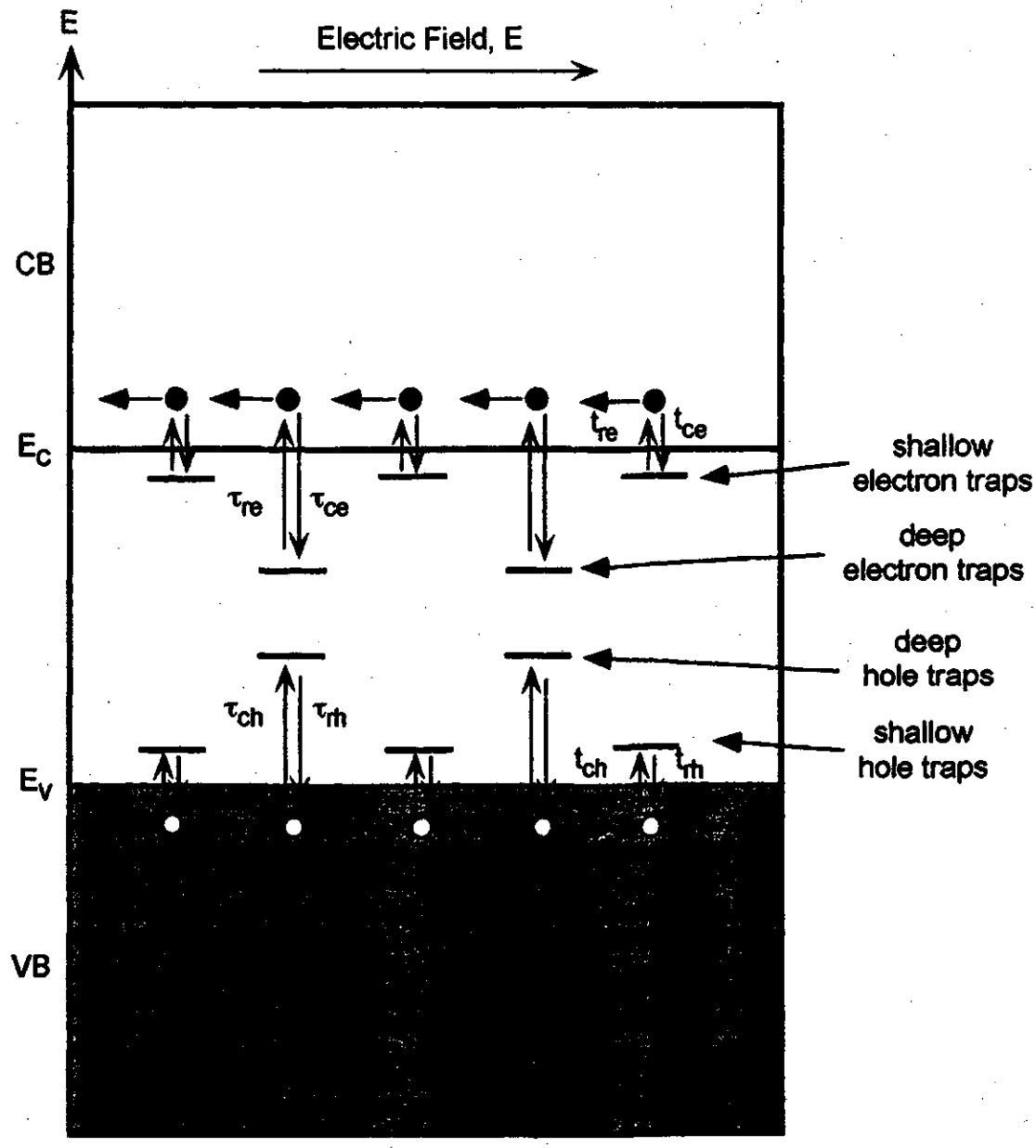

t_{ce} = lifetime for capture into shallow electron traps

t_{re} = lifetime for release from shallow electron traps

τ_{ce} = lifetime for capture into deep electron traps

τ_{re} = lifetime for release from deep electron traps

t_{ch} = lifetime for capture into shallow hole traps

t_{rh} = lifetime for release from shallow hole traps

τ_{ch} = lifetime for capture into deep hole traps

τ_{rh} = lifetime for release from deep hole traps

Figure 2.7. Four Categories of Trapping Centers and Associated Lifetimes. In this simplified sketch, band bending due the the applied electric field is ignored.

The thermal carrier velocity and the capture cross-section are essentially constant [7], and are often lumped into a single constant, C_t., called the capture coefficient. The capture lifetime can then be written as

$$\tau_c = \frac{1}{C_t N_{avail}} \tag{2.4}$$

From this relation we see that the capture lifetime is inversely proportional to the trap concentration of a given trap. Therefore, if the trap density is high, the associated capture lifetime will be short. Once a carrier has become trapped, it will remain there until an energetic lattice vibration imparts enough energy to the carrier to excite it back into the extended states. Release from deep traps requires more energy than release from shallow traps because deep traps lie deeper in the mobility gap. Since low energy lattice vibrations are much more probable than high energy lattice vibrations, the release lifetime from shallow traps, t_r, is much shorter than the release lifetime from deep traps, τ_r. The shallow trap release lifetime t_r is much shorter than the transit time, whereas the deep trap release lifetime τ_r can be much longer than the transit time.

The two different types of traps, shallow and deep, affect transport in very different ways because of the disparity in their release lifetimes (i.e. $t_r << \tau_r$). Specifically, we are interested in how they affect transport when an amorphous material is being used as a xerographic photoreceptor. The capture and release times for shallow traps are small enough in comparison with the time scale of a xerographic discharge that the effect of shallow traps on the discharge can be viewed as a reduction in mobility and an increase in the deep trap capture lifetime. This can be shown as follows. Let μ_o define the mobility of either type of carrier in the absence of shallow traps. This quantity is often referred to as the microscopic mobility. When viewed against the shallow traps, this carrier will spend, on average, t_c amount of time in the extended states

before it becomes captured by a shallow trap (see Figure 2.8). Once captured, it will spend t_r amount of time in the shallow trap, on average, before it is released back into the extended states. As a result, the fraction of time that the carrier spends drifting in the extended states is equal to

$$\frac{t_c}{t_c + t_r} \tag{2.5}$$

and the fraction of time that the carrier is trapped in a shallow trap is

$$\frac{t_r}{t_c + t_r} \tag{2.5}$$

Therefore, the resulting average or effective mobility is given by

$$\mu = \mu_o \frac{t_c}{t_c + t_r} + 0 * \frac{t_r}{t_c + t_r} = \mu_o \frac{t_c}{t_c + t_r} = \theta \mu_o \tag{2.6}$$

where $\theta = t_c / (t_c + t_r)$ is called the mobility reduction factor. Since the same carrier is only available to the deep trapping process for the same fraction of time, the deep trapping capture lifetime is enhanced by the same factor, i.e.

$$\tau_c = \frac{\tau_{co}}{\theta} \tag{2.7}$$

where τ_c = deep trap capture lifetime in the presence of shallow traps

τ_{co} = deep trap capture lifetime in the absence of shallow traps

Since the concentration of deep trapping centers, N_t, remains constant in the presence of shallow traps, the effect of shallow traps is viewed as a reduction in the capture coefficient, i.e.

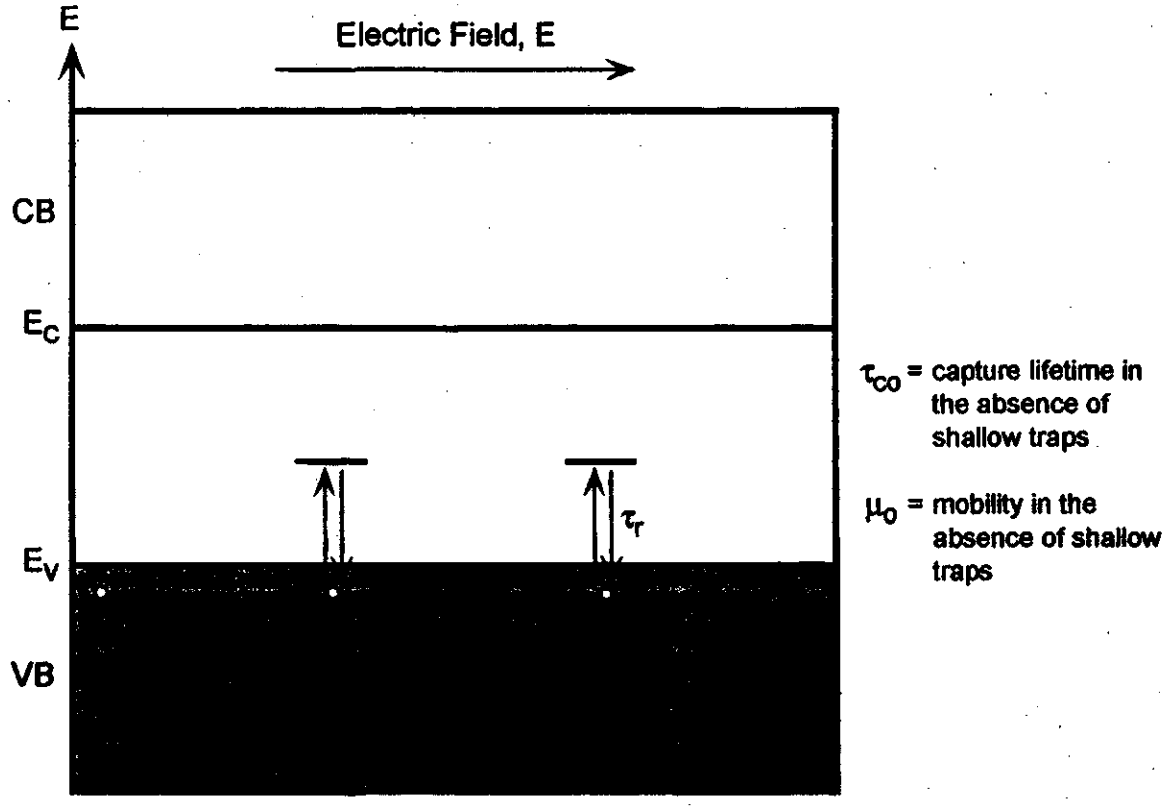

(a) In the absence of shallow traps

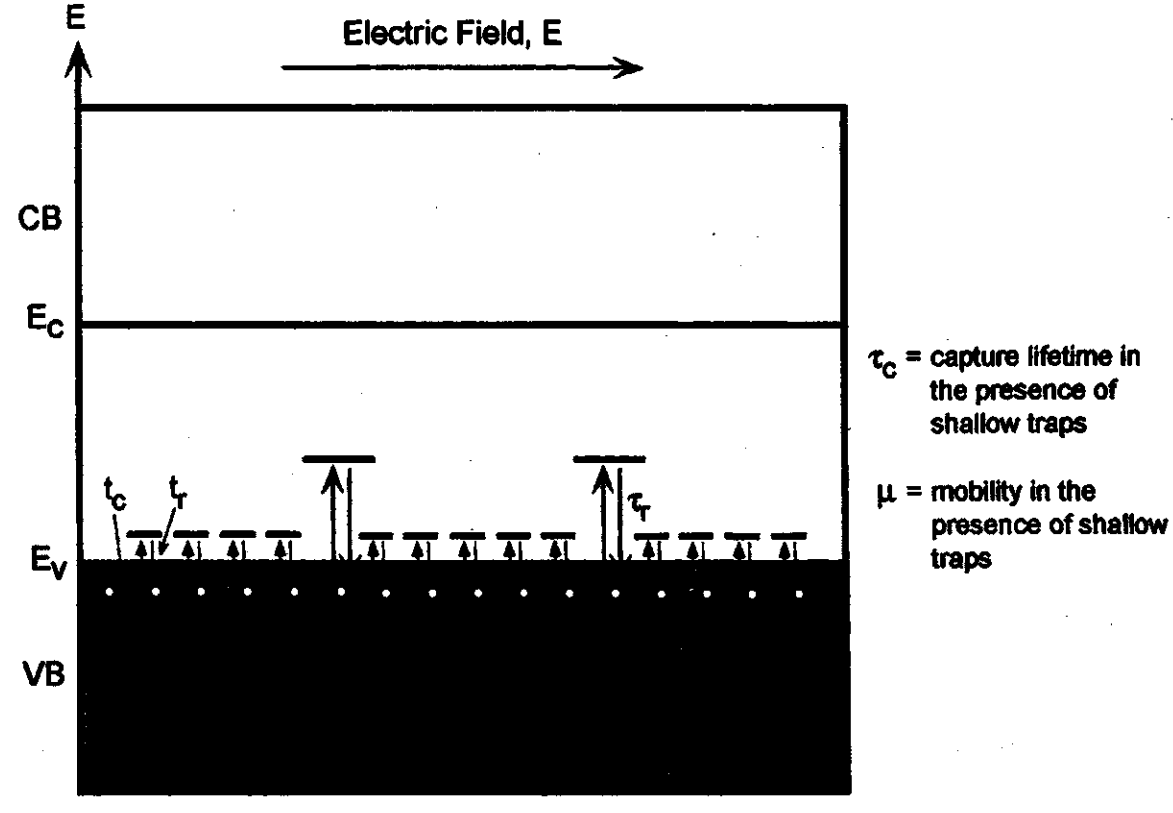

(b) In the presence of shallow traps

Figure 2.8. The effect of shallow traps on mobility and deep trapping capture lifetime (holes only).

$$C_t = \theta C_{to} \tag{2.8}$$

where C_t = capture coefficient in the presence of shallow traps

C_{to} = capture coefficient in the absence of shallow traps

This expression, when substituted into Equation (2.4), gives rise to Equation (2.7). To summarize, the effect of shallow traps is to create an apparent decrease in mobility and an increase in the deep trap capture lifetime. If a xerographic discharge is being considered, the effect is to increase the time scale of the discharge by $1/\theta$. This is not a problem unless the discharge time exceeds the required time between the exposure and development phases.

The effect of deep traps is much different. These traps have much longer release times because they lie deep within the mobility gap and thus have a high activation energy. The release time from deep traps may in fact be much longer than the time scale of a xerographic discharge. As a result, carriers trapped in deep traps are often viewed as being permanently trapped when considering their effect on a xerographic discharge. The presence of deep traps has a profound effect on the efficiency of the xerographic discharge. Any charge captured by deep traps remains there long past the duration of a single xerographic discharge. Charges remaining in deep traps prevent the photoreceptor from becoming discharged, creating what is called a residual potential. This residual potential will build up as the photoreceptor is cycled through many discharge cycles. If the density of deep traps is sufficiently high, the residual potential will become high enough to prevent the material from being used as a photoreceptor.

It is evident that trapping effects play a large role in determining the nature of transport in amorphous materials, and therefore must be included in any accurate model for xerographic discharge. The remainder of this thesis will focus on modeling how trapping affects the exact nature of the discharge.

3. THEORETICAL MODEL FOR PHOTO-INDUCED DISCHARGE

3.1 Introduction

Using the information put forth in the previous chapters we can assemble a more detailed idea of what occurs during a xerographic discharge. The photoreceptor starts from a sensitized state, with its surface charged to an initial potential of V_o, as shown in Figure 3.1 (a). Next, the surface of the photoreceptor is illuminated, creating electron-hole pairs in the bulk through the process of photogeneration. The electrons drift towards the surface and cancel out the positive charge. The holes drift towards the grounded back electrode. As the electrons and holes drift, they interact with localized trapping centers, as shown in Figure 3.1 (b). The net result of this process is to reduce the positive charge located on the surface, thereby discharging the photoreceptor. This process continues until the light is removed. At this point, any remaining untrapped carriers are swept out of the bulk and a fraction of the photogenerated carriers remain in deep traps, creating a residual potential, V_r, as shown in Figure 3.1 (c).

In order to create a tractable mathematical model of this process, the following simplifying assumptions can be made:

(1) The incident light is strongly absorbed in a very thin region located near the surface. This is justified because the absorption depth δ is much smaller than the thickness of the film, L. For example, in a-Se, δ is less than 0.1 μm at a wavelength of 450 nm or shorter. This is much smaller than the thickness of a typical photoreceptor (L=50 μm). An obvious consequence of this is that all

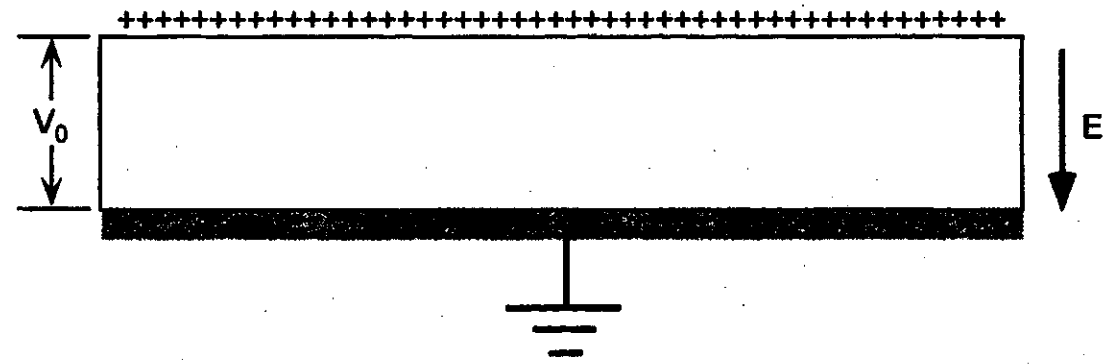

(a) Sensitized State

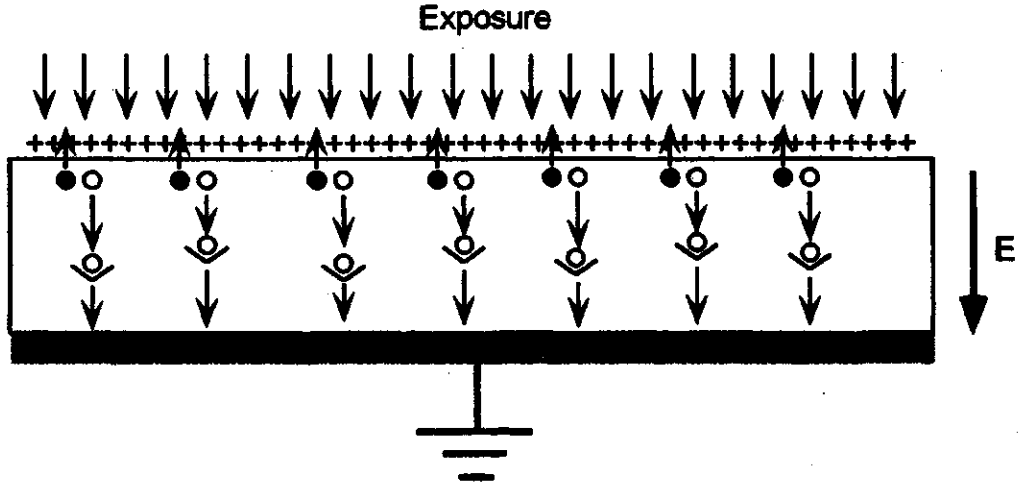

(b) Exposure and Transport

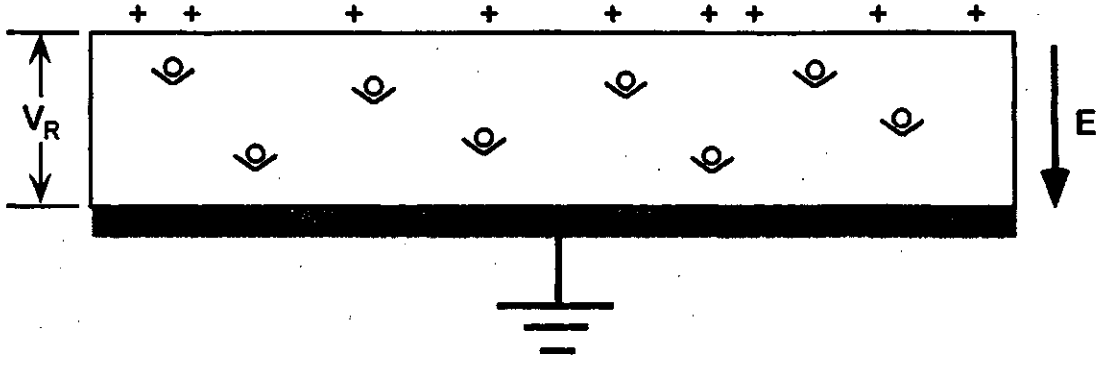

(c) Final State

V_R = Residual Potential

Legend: ○ Hole
● Electron
Trapped Hole

Figure 3.1. Three Stages of Photo-Induced Discharge.

photogeneration also occurs in the same thin layer. Since the electrons only have a small distance to travel before they reach the surface, it can be assumed that the electrons immediately travel to the surface and cancel out the positive charge, leaving the holes to drift towards the substrate.

(2) The density of thermally generated carriers is negligible in comparison to the number of photogenerated carriers at room temperature. This assumption is justified because the size of the band gap is large (i.e. greater than 2 eV) and therefore[6]

$$n_i, p_i = (N_v N_c)^{1/2} e^{-E_t / 2kT} << p_{ph}$$

where n_i = the density of thermally generated electrons
p_i = the density of thermally generated holes
p_{ph} = the density of photogenerated holes

(3) Charge is not injected from the surface or the rear contact in the absence of light and therefore the only carriers present are photogenerated. Note that this was previously identified as being a requirement necessary to all practical photoreceptors.

(4) Only one set of hole traps is present. This single set can be used to model the behaviour of a mono-energetic level of shallow or deep traps. If a model of deep trapping is being constructed, the effect of shallow traps can be incorporated as a reduction in mobility and an increase in the deep trap capture lifetime, as was demonstrated earlier. If shallow trapping is being modeled, deep trapping must be neglected.

(5) Recombination effects can be ignored since recombination coefficients are typically small.

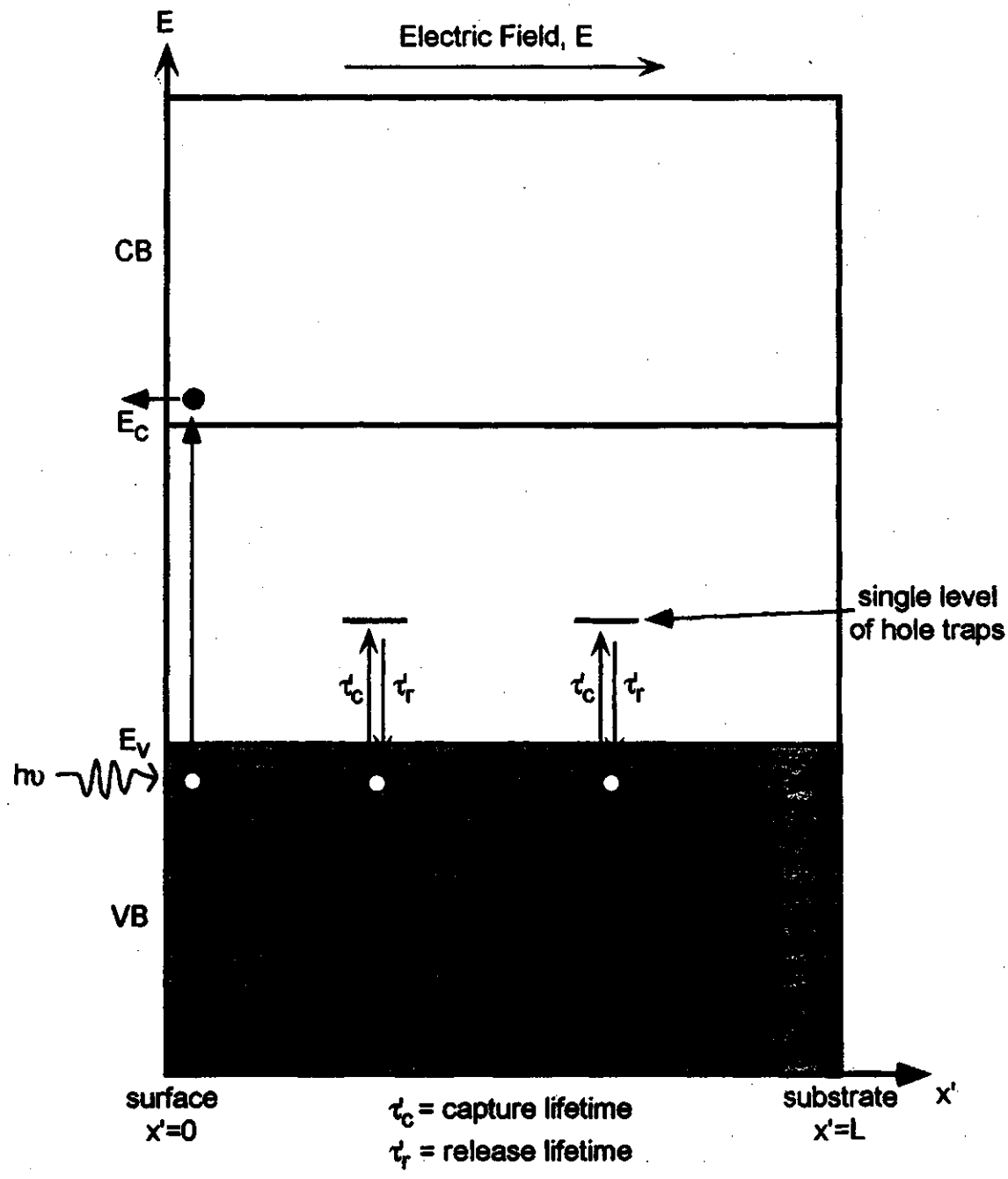

Figure 3.2. Band diagram used for photo-induced discharge modelling.

In light of these assumptions, we can create a simplified view of photoinduced discharge, as is shown in Figure 3.2. Note that only photogenerated hole transport and a single level of traps is being considered. This configuration is the basis for many previous models found in the literature. The key aspects of a few of these models are described below.

3.2 The Kanazawa-Batra (K-B) Model

One of the earliest theoretical treatments of photo-induced discharge is the model presented by Kanazawa and Batra [8], commonly known as the K-B model. In this model, a photoreceptor of thickness L is grounded at one surface (x'=L), while the other (x'=0) is charged to an initial voltage V_o. The entire surface at x'=0 is uniformly illuminated with strongly absorbed light for all times t'≥0. If the illumination is assumed to be uniform over the entire surface, the problem can be cast in one dimension. The equations governing the discharge in the K-B model are the following:

1) Conduction Current:

$$J_c(x',t') = ep'(x',t')\mu E'(x',t') \tag{3.1}$$

2) Total Current:

$$J(t') = J_c(x',t') + \frac{\varepsilon \partial E'(x',t')}{\partial t'} = 0 \tag{3.2}$$

3) Gauss' Law in point form:

$$\frac{\partial E'(x',t')}{\partial x'} = \frac{e}{\varepsilon}\left(p'(x',t') + p_t'(x',t')\right) \tag{3.3}$$

4) Deep Trapping Rate Equation

$$\frac{\partial p_t'(x',t')}{\partial t'} = \frac{p'(x',t')}{\tau_c'} \tag{3.4}$$

where $E'(x',t')$ = electric field

$p'(x',t')$ = free hole density

$p_t'(x',t')$ = trapped hole density

$\tau_c' = \frac{1}{C_t(N_t - p_t')}$ = deep trap capture lifetime

N_t = uniform deep trap concentration

C_t = capture coefficient

μ = hole mobility

ε = permittivity of the film

e = electron charge

A few comments should be made about these equations. In (3.1), we can see that only conduction due to holes is considered. The diffusion current

$$J_d(x',t') = -eD_p\frac{\partial p'(x',t')}{\partial x'} \tag{3.5}$$

has been neglected. This assumption is valid at room temperature since diffusion is a thermally activated process and kT/eV_o is negligible[7]. The total current given by (3.2) is equal to zero because the xerographic arrangement is an open circuit configuration. In (3.4), the release from traps is not considered, i.e. the trap release lifetime τ_r' is taken as being infinite. Also, in the K-B model, it is assumed that the density of trapped carriers p_t' is much smaller than the total trap density, N_t, so that the unfilled trap density is approximately N_t and the trap capture lifetime τ_c' can be assumed to be constant, i.e.

$$\tau_c' = \frac{1}{C_t(N_t - p_t')} \cong \frac{1}{N_tC_t} \quad \text{if } p_t' << N_t \tag{3.6}$$

Essentially, this means that the effect the trap filling is ignored. If deep trapping in the presence of shallow traps is being modeled, the capture coefficient can be replaced by the shallow trap controlled capture coefficient given in Equation (2.8) [9]. Likewise, the

mobility μ can be replaced by the shallow trap controlled mobility given by Equation (2.6).

It is convenient to convert the previous equations to dimensionless quantities by defining the following:

$$x = x'/L \tag{3.7}$$

$$t = t'/t_0 \tag{3.8}$$

$$p(x,t) = eLp'(x',t')/CV_0 \tag{3.9}$$

$$p_t(x,t) = eLp_t'(x',t')/CV_0 \tag{3.10}$$

$$E(x,t) = E'(x',t')/E_0' \tag{3.11}$$

$$j_c(x,t) = t_0 J_c(x',t')/CV_0 \tag{3.12}$$

$$\tau_c = \tau_c'/t_0 \tag{3.13}$$

where $t_0 = L^2/\mu V_0$ = transit time

$E_0' = V_0/L$ = initial electric field

$C = \varepsilon/L$ = capacitance per unit area

Substituting these dimensionless variables into (3.1) through (3.4) gives:

$$j_c(x,t) = p(x,t)E(x,t) \tag{3.14}$$

$$j_c(x,t) + \frac{\partial E(x,t)}{\partial t} = 0 \tag{3.15}$$

$$\frac{\partial E(x,t)}{\partial x} = p(x,t) + p_t(x,t) \tag{3.16}$$

$$\frac{\partial p_t(x,t)}{\partial t} = \frac{p(x,t)}{\tau_c} \tag{3.17}$$

Boundary and initial conditions can then be determined from the following pieces of information. At t=0, the surface of the sample at x=0 is charged to an initial voltage of V_0. At this time, there is no trapped or free charge left in the bulk. Therefore, the photoreceptor is analogous to a charged parallel plate capacitor with a field of V_0/L present in the region between the plates. These statements lead to the initial conditions (specified in terms of the normalized variables):

$$E(x,0) = 1, \qquad 0 \le x \le 1 \tag{3.18}$$

$$p(x,0) = 0, \qquad 0 \le x \le 1 \tag{3.19}$$

$$p_t(x,0) = 0, \qquad 0 \le x \le 1 \tag{3.20}$$

Also, if illumination is applied for all $t \ge 0$, the discharge will continue until all of the surface charge at x=0 has been injected into the bulk. Therefore, the field just below the surface at x=0 will eventually vanish and

$$E(0,\infty) = 0 \tag{3.21}$$

Note that this statement is true for any arbitrary law of injection. Combining the initial conditions (3.18) and (3.20) with Equations (3.14) through (3.17) gives a partial differential equation in E(x,t):

$$\frac{\partial E(x,t)}{\partial t} + E(x,t)\frac{\partial E(x,t)}{\partial x} = -\frac{E(x,t)}{\tau_c}\ln E(x,t) \tag{3.22}$$

For large values of t (specifically $t >> \tau_c$, $t > 1$) and for low injection rates, all time variance will be small in comparison with the spatial variation and the first term of (3.22) can be neglected. The result is a simple total differential equation:

$$\frac{\partial E(x,t)}{\partial x} = -\frac{\ln E(x,t)}{\tau_c} \qquad (3.23)$$

A complete review of the solution method presented by Kanazawa and Batra is beyond the scope of this work. However, a few important results of their analysis should be presented.

Solving (3.23) with $t = \infty$ gives the final state of the electric field, $E(x,\infty)$, from which the residual potential, V_r, can be calculated:

$$v_r = \frac{V_r}{V_0} = \int_0^l E(x,\infty)dx \qquad (3.24)$$

Since the solution for $E(x,\infty)$ will vary with τ_c through (3.23), the residual potential will be a function of τ_c. A plot of the normalized residual voltage, v_r, versus the normalized deep trap capture lifetime τ_c, is referred to in the literature as the "universal curve" and is depicted in Figure 3.3. This is the central result of the Kanazawa-Batra model. It asserts that the residual potential is solely a function of the capture lifetime and is independent of the injection history (i.e. intensity and duration).

The accuracy of the K-B model of residual potentials has been checked using μ and τ_c' values obtained using the Interrupted-Field Time of Flight (IFTOF) method and V_r measurements obtained in xerographic experiments. Values for V_r obtained from μ and τ_c' through the universal curve have been found to be almost an order of magnitude larger than values found from xerographic experiments[9]. From these results, it would appear that the Kanazawa-Batra model is incomplete. Kasap et al. [9] suggest that the discrepancy is due to the fact that trap filling has been neglected, i.e. $p_t' << N_t$ has been assumed. The analysis presented by Kasap et al. asserts that the KB assumption that $p_t' << N_t$ is only valid if

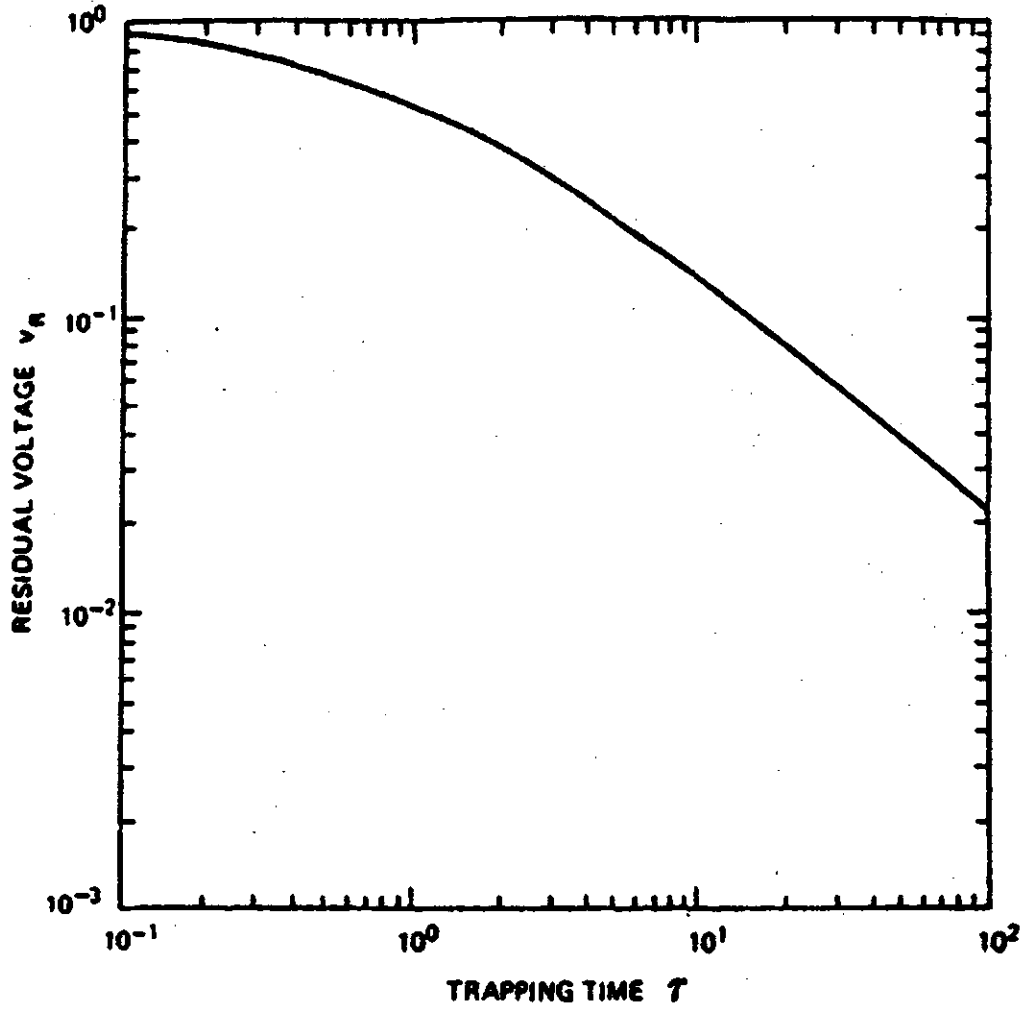

Figure 3.3. Universal Curve relating the normalized residual potential to the normalized trapping parameter τ (after [8]).

$$\frac{\varepsilon C_t}{e\mu_0} << 1 \qquad (3.25)$$

Also, in the K-B model, the surface voltage decays to a residual potential that remains strictly constant for all time. In real samples however, the residual potential is seen to decay with time, suggesting that significant release from deep traps is occurring. It appears obvious that accurate models for photo-induced discharge must include the effects of both trap filling and release.

3.3 Model for PID including trap release and filling

Other authors have recognized the shortcomings of the K-B model, and have improved upon it. Okuda et al. [7] have presented a model that includes release of holes from deep traps. Under these circumstances, the deep trapping rate equation, Eq. (3.4), becomes

$$\frac{\partial p_t'(x',t')}{\partial t'} = \frac{p'(x',t')}{\tau_c'} - \frac{p_t'(x',t')}{\tau_r'} \tag{3.26}$$

This form of the rate equation, because it includes release from traps, can account for the decay of the residual potential. However, in their model the capture constant τ_c' is still approximated by

$$\tau_c' \cong \frac{1}{N_t C_t} \tag{3.27}$$

and trap filling is still ignored. A model has been presented by Kasap et al. [10] however, that includes both trap filling and release. In their model, the approximation $p_t' << N_t$ is not taken and therefore Eq. (3.26) becomes

$$\frac{\partial p_t'(x',t')}{\partial t'} = p'(x',t')C_t\left[N_t - p_t'(x',t')\right] - \frac{p_t'(x',t')}{\tau_r'} \tag{3.28}$$

Normalizing with Equations (3.7) through (3.13) gives

$$\frac{\partial p_t(x,t)}{\partial t} = \omega p(x,t) - r p_t(x,t) - c p(x,t) p_t(x,t) \tag{3.29}$$

where $\omega \equiv t_0 / \tau_{c0}'$ = normalized unsaturated trapping rate

$r \equiv t_0 / \tau_r'$ = normalized release rate

$c \equiv \varepsilon C_t / e\mu_0$ = normalized capture coefficient

$\tau_{c0}' \equiv 1/N_t C_t$ = unsaturated trapping rate

Note that the unsaturated trapping rate, τ'_{c0}, is the trapping rate used in the K-B and Okuda models. Setting r=0, c=0 causes the model to reduce to the K-B model. Setting c=0 causes the model to reduce to the Okuda model. Notice that the required condition for ignoring trap filling given in Equation (3.25) can now be rewritten in terms of the normalized capture coefficient, i.e.

$$c \ll 1 \tag{3.30}$$

This result is consistent with Equation (3.29) since c=0 implies that trap filling is ignored (e.g. $C_t \to 0$, $N_t \to \infty$, $1/N_tC_t$ = constant since τ'_{c0} is fixed).

Solving Equations (3.14), (3.15), (3.16), and (3.29) for E(x,t) gives a second order non-linear partial differential equation in E(x,t) (the (x,t) has been dropped for clarity):

$$E\frac{\partial^2 E}{\partial t^2} + E^2\frac{\partial^2 E}{\partial t \partial x} - (1+c)\left(\frac{\partial E}{\partial t}\right)^2 - cE\left(\frac{\partial E}{\partial x}\right)\left(\frac{\partial E}{\partial t}\right) + (\omega + r)E\frac{\partial E}{\partial t} + rE^2\frac{\partial E}{\partial x} = 0 \tag{3.31}$$

If a solution for E(x,t) can be obtained, V(t), p(x,t), and $p_t(x,t)$ can then be obtained from the E(x,t) as follows:

$$V(t) = \int_0^1 E(x,t)dx \tag{3.32}$$

Combining Equations (3.14) and (3.15) gives

$$p(x,t) = -\frac{1}{E(x,t)}\frac{\partial E(x,t)}{\partial t} \tag{3.33}$$

and combining Equations (3.33) and (3.16) gives

$$p_t(x,t) = \frac{\partial E(x,t)}{\partial x} + \frac{1}{E(x,t)}\frac{\partial E(x,t)}{\partial t} \tag{3.34}$$

3.4 Boundary and Initial Conditions

In order to obtain a solution for E(x,t), suitable boundary and initial conditions must be chosen. In previous works [7, 8, 10], two different sets of boundary conditions have been considered, those corresponding to weak step illumination and pulsed illumination.

3.4.1 Weak Step Illumination

The boundary conditions for the case of weak step illumination were first proposed by Kanazawa and Batra [8] They selected a power law of injection that reflects field-dependent quantum efficiency:

$$j_c(0,t) = KE^m(0,t) \tag{3.35}$$

where K is a constant that includes the illumination flux density. Substituting this relation into Equation (3.15) with x=0 gives

$$\frac{dE(0,t)}{dt} = -KE^m(0,t) \tag{3.36}$$

Integrating this expression gives an expression for E(0,t) which governs the field at the boundary x=0:

$$E(0,t) = [1-(1-m)Kt]^{1/(1-m)}, \quad m \neq 1 \tag{3.37}$$

$$E(0,t) = e^{-Kt}, \quad m = 1 \tag{3.38}$$

In order to simulate weak injection and to ensure that the discharge is purely injection limited, a small value for the intensity constant K is often chosen. Kanazawa and Batra [8] and Kasap et al. [10] chose a value of $K=10^6$. If $m\neq0$ is chosen, the surface field and charge will drop to zero at a well defined time:

$$t_{final} = \frac{1}{(1-m)K} \tag{3.39}$$

If m=0.5 is chosen [10], then the discharge will end at $t_{final} = 2 * 10^6$. Since hole transit times are roughly around 1μs, this implies discharge durations of approximately 2 seconds. Solving for E(x,t), V(t), p(x,t), etc. over this time scale is a useful exercise because the exposure times used during xerographic experiments are comparable (≈ 5 s). This allows direct comparison of theoretical results with experimental results.

In a xerographic configuration where the sample is initially free of space charge, Equations (3.18), (3.19) and (3.20) proposed by Kanazawa and Batra will hold. Combining these equations with Equations (3.16) and (3.33) leads to a complete set of initial conditions:

$$E(x,0) = 1, \qquad 0 \le x \le 1 \tag{3.40}$$

$$\frac{dE(x,0)}{dx} = 0, \qquad 0 < x \le 1 \tag{3.41}$$

$$\left.\frac{\partial E(x,t)}{\partial t}\right|_{t=0} = 0, \quad 0 < x \le 1 \tag{3.42}$$

The theoretical characteristics of photo-induced discharge subject to injection limited conditions have been studied exhaustively in the literature. Kanazawa and Batra [8] presented an analytical solution for E(x,t) for $t' >> t_0$, neglecting trap release (r=0) and filling (c=0). Okuda et al. [7] have solved for E(x,t) for the case of r≠0, c=0 (release, filling neglected). Kasap et al. [10] have solved for E(x,t) for the general case of r≠0, c≠0. A detailed review of their results is beyond the scope of this work, and can be found in the literature.

3.4.2 Pulsed Illumination

Solving Equation (3.31) under weak step illumination conditions is useful if one wants to compare theoretical results with results obtained from xerographic experiments. However, pulse illumination is more representative of what happens in real world applications. For example, in laser printing applications, the photo-receptor is rapidly scanned with an intense laser beam, causing a localized photo-induced discharge wherever the beam strikes the surface.

In the pulsed illumination scenario, it can be assumed that an extremely thin region of photogenerated carriers is instantaneously created near the surface of the photoreceptor when it is illuminated. Under these conditions, the electrons immediately travel to the surface and cancel out a fraction of the initial positive charge. A small packet of holes remains. This packet of holes will then drift across the film towards the metal substrate. For the purposes of modeling, we define φ as the normalized or fractional amount of charge remaining on the surface. The normalized amount of charge injected into the film is therefore $1 - \varphi$. A small value of φ therefore indicates strong pulsed illumination, and a large value of φ indicates weak pulsed illumination. To formulate boundary conditions, we assume that we start with an initial free charge density $p(x,0)$ that satisfies

$$\int_0^1 p(x,0)dx = 1-\varphi \tag{3.43}$$

Of course, $p(x,0)$, must be concentrated into a small region near the surface to satisfy the strong absorption criterion. Assuming that the initial trapped density $p_t(x,0)$ is zero as in Equation (3.20), an expression for the initial electric field gradient can be obtained from Equation (3.16):

$$\frac{dE(x,0)}{dx} = p(x,0) \tag{3.44}$$

Since the initial surface charge is φ, the initial electric field is given by

$$E(x,0) = \varphi + \int_0^x p(x,0)dx \tag{3.45}$$

Remaining boundary conditions can then be obtained from (3.44) and (3.45). Equations (3.44), (3.14), and (3.15) give:

$$\left.\frac{\partial E(x,t)}{\partial t}\right|_{t=0} = -E(x,0)\frac{dE(x,0)}{dx}, \quad 0 < x \le 1 \tag{3.46}$$

Also, since the surface charge remains at φ for the entire discharge ($t>0$), we see that

$$E(0,t) = \varphi \tag{3.47}$$

$$\frac{dE(0,t)}{dt} = 0 \tag{3.48}$$

$$\frac{d^2E(0,t)}{dt^2} = 0 \tag{3.49}$$

Therefore, if the initial free charge density p(x,0) is known, the remaining boundary conditions can be found. Using the numerical solution methods presented in Chapter 4, a solution for E(x,t) can be obtained, allowing an examination of how, ω, r, c, φ, and the initial free charge distribution p(x,0) affect the characteristics of the discharge.

In order to obtain a solution for E(x,t), p(x,0) must be known. If the photoreceptor has a normalized optical absorption coefficient α, then the light intensity will drop off as $e^{-\alpha x}$. The initial density of photogenerated free holes p(x,0) will therefore have the same dependence. An expression for p(x,0) that satisfies the injection condition given in (3.43) is

$$p(x,0) = (1-\varphi)\alpha\frac{e^{-\alpha x}}{1-e^{-\alpha}} \tag{3.50}$$

The absorption coefficient α is chosen so that p(x,0) is only significant in a very thin layer near x=0. For numerical reasons, it is advantageous to choose a simpler function for p(x,0) that has better behaved derivatives and a more uniform distribution of charge. The charge distribution used in this work is a "wedge-shaped" distribution given by:

$$p(x,0) = \begin{cases} \dfrac{400(1-\varphi)x}{19\delta^2}, & 0 \le x < \dfrac{\delta}{20} \\ \dfrac{20(1-\varphi)}{19\delta}, & \dfrac{\delta}{20} \le x < \dfrac{19\delta}{20} \\ \dfrac{400(1-\varphi)(\delta-x)}{19\delta^2}, & \dfrac{19\delta}{20} \le x < \delta \\ 0, & x \ge \delta \end{cases} \tag{3.51}$$

The theoretical behavior of photo-induced discharge under pulsed-illumination conditions has not been exhaustively studied. Kasap et al. [11] have solved Equation (3.31) when w≠0, c≠0, r=0, φ = 0.05 (95% injection) and φ=0.90 (10% injection). No satisfactory solution to (3.31) has been found under general trapping conditions (i.e. w≠0, r≠0, c≠0) and when the injection is extremely high (≈99%). Results obtained by Kasap et al. indicate that the effect of trap saturation is extremely pronounced under high injection (95%) conditions. One would expect that introducing release (r≠0) would significantly alter the results. Also, the high injection situation is of great interest because this scenario occurs in practical configurations such as laser printers. The remainder of this thesis will concentrate on solving (3.31) under these conditions.

4. NUMERICAL METHODS

Obtaining an exact solution for the PID differential equation developed in Chapter 3 would involve finding a solution over the (x,t) domain, which is continuous. For obvious reasons, this domain is not well-suited to solving the equation on a computer. In order to achieve a workable numerical solution method, we first need to devise a domain that lends itself to a computer solution.

4.1 Solution Grid

Equation (3.31) is a differential equation describing the electric field over the (x,t) domain. Recalling that x and t are normalized variables, we note that the domain of this problem is

$$0 \le x \le 1 \tag{4.1}$$

$$0 \le t \le \infty \tag{4.2}$$

Obtaining a solution over the entire time domain is impractical, and it is useful to impose an upper limit on the time domain, i.e.

$$0 \le t \le t_{max} \tag{4.3}$$

The upper limit t_{max} is chosen to be much longer than the duration of the discharge, i.e. at least several transit times.

A common technique used when solving a differential equation numerically is to restrict the domain to discrete values. If the problem is two-dimensional, as in this case,

this approach is equivalent to superimposing a grid over the (x,t) domain, as shown in Figure 4.1. The x-axis is divided into LL points spaced k=1/LL apart. The t-axis is divided into MM points spaced $h=t_{max}/MM$ apart. A point on the grid is identified by a set of integer indices m and ℓ, which can take on the values

$$0 \le \ell \le LL \tag{4.4}$$

$$0 \le m \le MM \tag{4.5}$$

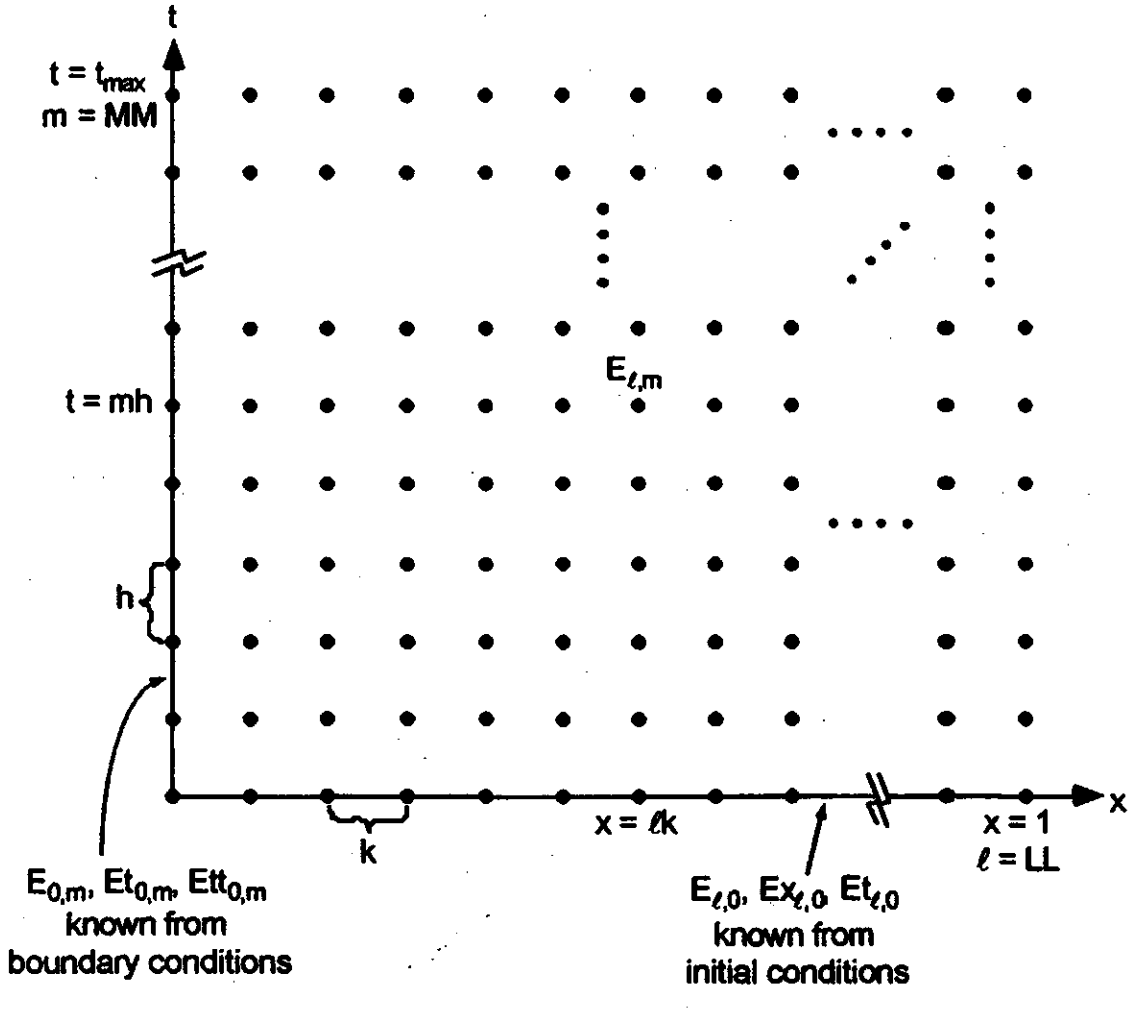

Figure 4.1. Grid used to obtain a numerical solution to the PID differential equation.

The (x,t) coordinate value of a grid point ℓ,m is therefore (ℓk,mh). In order to simplify the notation, the following conventions for the electric field and its derivatives at the grid points were adopted:

$$E_{\ell,m} = E(\ell k, mh) \tag{4.6}$$

$$Et_{\ell,m} = \left.\frac{\partial E(x,t)}{\partial t}\right|_{x=\ell k,\, t=mh} \tag{4.7}$$

$$Ex_{\ell,m} = \left.\frac{\partial E(x,t)}{\partial x}\right|_{x=\ell k,\, t=mh} \tag{4.8}$$

$$Ett_{\ell,m} = \left.\frac{\partial^2 E(x,t)}{\partial t^2}\right|_{x=\ell k,\, t=mh} \tag{4.9}$$

$$Etx_{\ell,m} = \left.\frac{\partial^2 E(x,t)}{\partial t \partial x}\right|_{x=\ell k,\, t=mh} \tag{4.10}$$

Substituting these definitions into Equation (3.31) gives

$$\begin{aligned} E_{\ell,m}Ett_{\ell,m} + E_{\ell,m}^2 Etx_{\ell,m} - (1+c)Et_{\ell,m}^2 - cE_{\ell,m}Ex_{\ell,m}Et_{\ell,m} \\ + (\omega + r)E_{\ell,m}Et_{\ell,m} + rE_{\ell,m}^2 Ex_{\ell,m} = 0 \end{aligned} \tag{4.11}$$

which is the differential equation governing the electric field at a point (ℓ,m) on the grid.

The derivatives in Equation (4.11) can be approximated in terms of the electric field values at neighboring grid points. A variety of methods can be used to do this. A first order approximation of the first derivatives can be obtained from the backward and forward Euler equations:

$$Et_{\ell,m} \approx \frac{E_{\ell,m} - E_{\ell,m-1}}{h} \quad \text{(backward Euler)} \tag{4.12}$$

$$Ex_{\ell,m} \cong \frac{E_{\ell,m} - E_{\ell-1,m}}{k} \quad \text{(backward Euler)} \tag{4.13}$$

$$Et_{\ell,m} \cong \frac{E_{\ell,m+1} - E_{\ell,m}}{h} \quad \text{(forward Euler)} \tag{4.14}$$

$$Ex_{\ell,m} \cong \frac{E_{\ell+1,m} - E_{\ell,m}}{k} \quad \text{(forward Euler)} \tag{4.15}$$

These basic equations could be used to create a variety of approximations for the second order derivatives in (4.11), $Ett_{\ell,m}$ and $Etx_{\ell,m}$. The approximations used in subsequent discussions are expressions based on repeated application of backward Euler. The backward Euler approximation is generally preferable to the forward Euler approximation because it has better inherent stability when it is used to solve differential equations [12]. An approximation to $Ett_{\ell,m}$ obtained from backward Euler is

$$Ett_{\ell,m} \cong \frac{Et_{\ell,m} - Et_{\ell,m-1}}{h} \tag{4.16}$$

Substituting Equation (4.12) into (4.16) gives

$$\begin{aligned} Ett_{\ell,m} &\cong \frac{\left(\frac{E_{\ell,m} - E_{\ell,m-1}}{h}\right) - \left(\frac{E_{\ell,m-1} - E_{\ell,m-2}}{h}\right)}{h} \\ &= \frac{E_{\ell,m} - 2E_{\ell,m-1} + E_{\ell,m-2}}{h^2} \end{aligned} \tag{4.17}$$

Similarly, an expression can be obtained for $Etx_{\ell,m}$:

$$Etx_{\ell,m} \cong \frac{Ex_{\ell,m} - Ex_{\ell,m-1}}{h} \tag{4.18}$$

$$\begin{aligned} Etx_{\ell,m} &\cong \frac{\left(\frac{E_{\ell,m} - E_{\ell-1,m}}{k}\right) - \left(\frac{E_{\ell,m-1} - E_{\ell-1,m-1}}{k}\right)}{h} \\ &= \frac{E_{\ell,m} - E_{\ell-1,m} - E_{\ell,m-1} + E_{\ell-1,m-1}}{hk} \end{aligned} \tag{4.19}$$

Note that for these approximations to be accurate, the grid must have adequate resolution, i.e. MM and LL must be sufficiently large.

Our goal is to obtain a solution for $E_{\ell,m}$ over the entire grid. Specifically, we want to obtain the solution for a given set of boundary conditions, initial conditions, and trapping parameters (ω, r, c). In Chapter 3, we established the boundary and initial conditions for the case of pulsed photo-excitation (Equations (3.44) through (3.49)). These conditions can be rewritten in grid notation. The initial conditions are

$$Ex_{\ell,0} = p(\ell k, 0), \tag{4.20}$$

$$E_{\ell,0} = \varphi + \int_0^{\ell k} p(x,0)dx \tag{4.21}$$

$$Et_{\ell,0} = -E_{\ell,0}Ex_{\ell,0} \tag{4.22}$$

where φ is the normalized amount of charge remaining on the surface after injection. These equations hold for all ℓ where $0 \le \ell \le LL$. Recall that the initial untrapped charge distribution, p(x,0), is defined by Equation (3.51), which describes a "wedge-shaped" initial charge distribution. The boundary conditions, written in grid notation, are

$$E_{0,m} = \varphi \tag{4.23}$$

$$Et_{0,m} = 0 \tag{4.24}$$

$$Ett_{0,m} = 0 \tag{4.25}$$

for all m where $0 \le m \le MM$.

Many different solution algorithms can be obtained by combining the derivative approximations with the PID differential equation and the boundary and initial

conditions. Two algorithms which have been implemented by the author are presented here.

4.2 "Hybrid" Algorithm

The "hybrid" algorithm was developed by Kasap [10] and Z. Liang[13] and is referred to as such because it uses a combination of the forward and backward Euler techniques. A detailed description of this method follows.

The partial differential equation governing the discharge, written in grid notation, was presented in Equation (4.11):

$$\begin{aligned} E_{\ell,m}Ett_{\ell,m} + E^2_{\ell,m}Etx_{\ell,m} - (1+c)Et^2_{\ell,m} - cE_{\ell,m}Ex_{\ell,m}Et_{\ell,m} \\ + (\omega + r)E_{\ell,m}Et_{\ell,m} + rE^2_{\ell,m}Ex_{\ell,m} = 0 \end{aligned} \tag{4.11}$$

The derivative $Etx_{\ell,m}$ can be eliminated from this equation by substituting in the backward Euler approximation given in Equation (4.18):

$$\begin{aligned} E_{\ell,m}Ett_{\ell,m} + E^2_{\ell,m}\left(\frac{Ex_{\ell,m} - Ex_{\ell,m-1}}{h}\right) - (1+c)Et^2_{\ell,m} \\ - cE_{\ell,m}Ex_{\ell,m}Et_{\ell,m} + (\omega + r)E_{\ell,m}Et_{\ell,m} + rE^2_{\ell,m}Ex_{\ell,m} \approx 0 \end{aligned} \tag{4.26}$$

Solving for $Ex_{\ell,m}$ gives:

$$Ex_{\ell,m} \approx \frac{\frac{E^2_{\ell,m}}{h}Ex_{\ell,m-1} - E_{\ell,m}Ett_{\ell,m} + (1+c)Et^2_{\ell,m} - (w+r)E_{\ell,m}Et_{\ell,m}}{\frac{E^2_{\ell,m}}{h} - cE_{\ell,m}Et_{\ell,m} + rE^2_{\ell,m}} \tag{4.27}$$

From this equation we can see that

$$Ex_{\ell,m} \approx f(E_{\ell,m}, Et_{\ell,m}, Ett_{\ell,m}, Ex_{\ell,m-1}) \tag{4.28}$$

and therefore an estimate to $Ex_{\ell,m}$ can be obtained if $E_{\ell,m}$, $Et_{\ell,m}$, $Ett_{\ell,m}$, and $Ex_{\ell,m-1}$ are known. By applying the forward Euler approximation given by (4.15), we can then use this estimate to calculate an estimate for $E_{\ell+1,m}$, i.e.

$$E_{\ell+1,m} \cong E_{\ell,m} + kEx_{\ell,m} \tag{4.29}$$

Note that calculating an estimate $E_{\ell+1,m}$ requires values from earlier grids points (i.e. $E_{\ell,m}$, $Et_{\ell,m}$, $Ett_{\ell,m}$, and $Ex_{\ell,m-1}$). Therefore, in order to solve the entire grid, equations (4.27) and (4.29) must be applied in a sequence that guarantees knowledge of previous grid points, as depicted in Figure 4.2. The exact details of how these two equations are applied vary depending on where the point is located on the grid. Figure 4.3 depicts how (4.27) and (4.29) are applied to the grid.

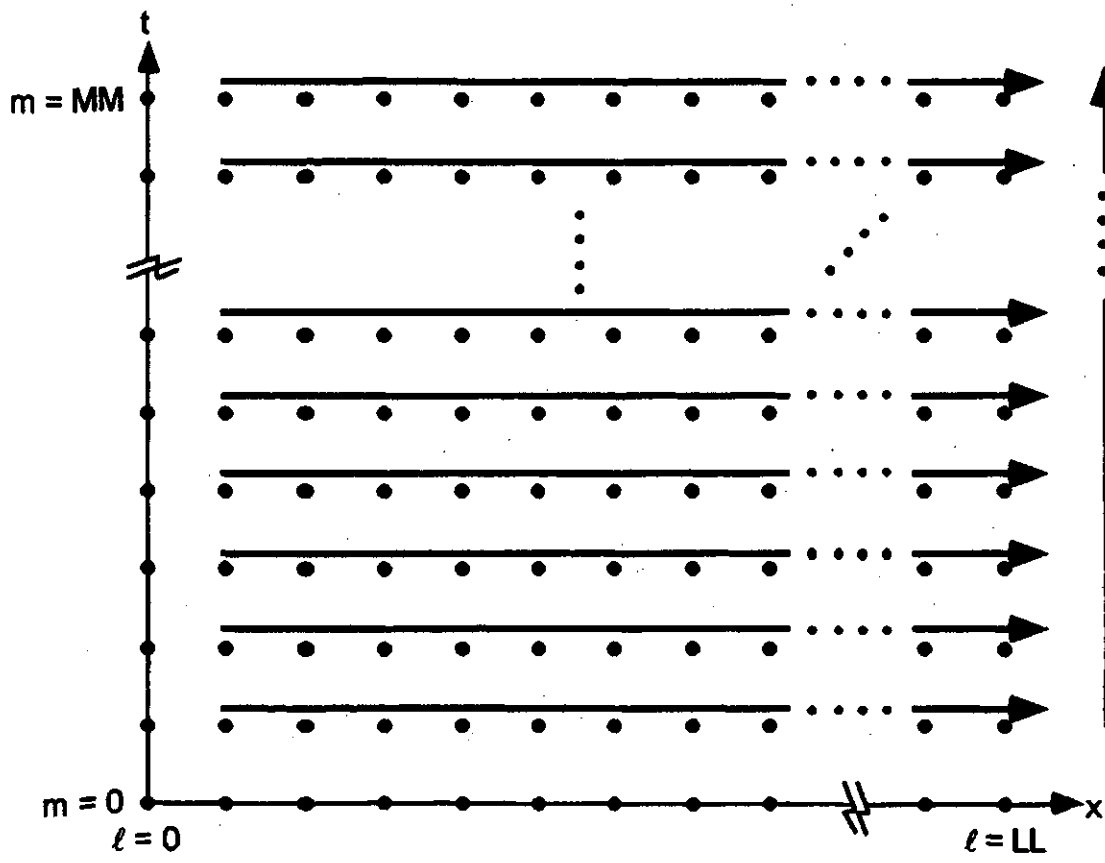

Figure 4.2. Solution sequence that guarantees knowledge of previous grid values.

In Figure 4.3 (a), the equations are applied to the grid point m=1, ℓ=0. All of the quantities required by Equation (4.27) are on the axes and are therefore supplied by boundary and initial conditions (refer to Figure 4.1). It is trivial to compute an estimate to $E_{1,1}$ from $E_{0,1}$, $Et_{0,1}$, $Ett_{0,1}$, and $Ex_{0,0}$ using Equations (4.27) and (4.29).

The solution sequence depicted in Figure 4.2 indicates that the remainder of the grid points in the row m=1 are then solved in ascending order (i.e. ℓ=1,2,3.. LL-1). This situation is depicted in Figure 4.3 (b). The values for $E_{\ell,0}$, $Et_{\ell,0}$, and $Ex_{\ell,0}$ are known from initial conditions, and the value for $E_{\ell,1}$ is known from the previous iteration. However, since these grid points do not lie along the t-axis, the values for $Et_{\ell,1}$ and $Ett_{\ell,1}$ are not known. Estimates for these quantities can be obtained from the backward Euler approximations:

$$Et_{\ell,1} \approx \frac{E_{\ell,1} - E_{\ell,0}}{h} \tag{4.30}$$

$$Ett_{\ell,1} \approx \frac{Et_{\ell,1} - Et_{\ell,0}}{h} \approx \frac{\frac{E_{\ell,1} - E_{\ell,0}}{h} - Et_{\ell,0}}{h} \tag{4.31}$$

Substituting these approximations into Equation (4.27) creates an equation of the form:

$$Ex_{\ell,1} \approx f(E_{\ell,1}, E_{\ell,0}, Et_{\ell,0}, Ex_{\ell,0}) \tag{4.32}$$

and therefore the values for $E_{\ell+1,1}$ can be calculated from (4.27) and (4.29) using known values and the approximations given by (4.30) and (4.31).

The remainder of the rows are then solved in ascending order (m=2,3,4.. MM), as depicted in Figure 4.2. The case of ℓ=0, $2 \le m \le$ MM, is shown in Figure 4.3 (c). Since these points lie on the t-axis, $E_{0,m}$, $Et_{0,m}$, and $Ett_{0,m}$ are known from boundary conditions. An estimate for $Ex_{0,m-1}$ is known from calculations performed in the previous row. These values can be directly substituted into (4.27) and (4.29) to obtain an estimate for $E_{1,m}$.

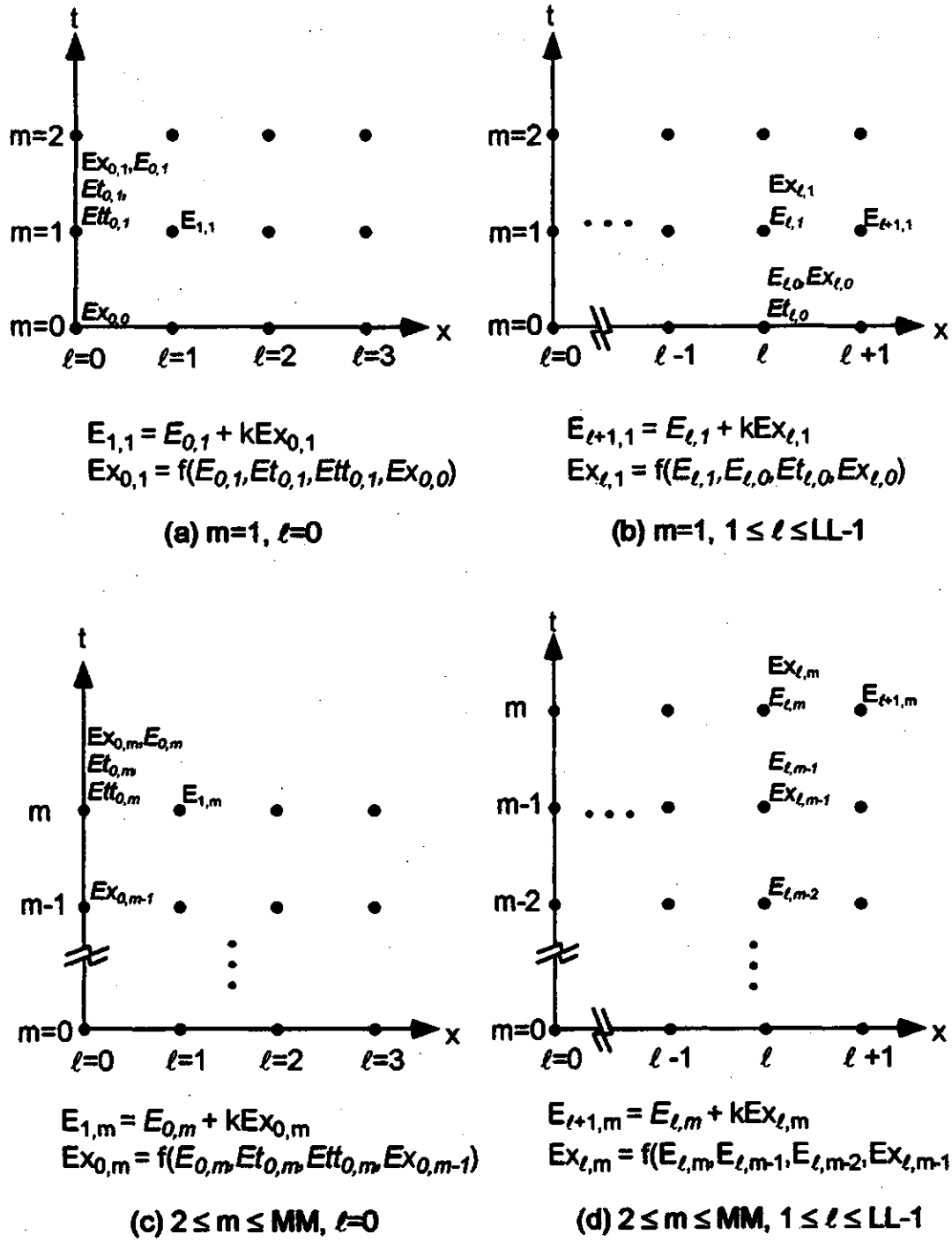

Note: Grid values shown in italics are known from boundary and initial conditions or prior iterations.

Figure 4.3. "Hybrid" solution method obtained by combining the forward and backward Euler approximations.

The general case for the remainder of the row is shown in Figure 4.3 (d). Since these grid points do not lie near either axis, knowledge of boundary conditions cannot be used. An estimate for $Ex_{\ell,m-1}$ can be obtained from calculations performed on the previous row. Estimates for $Et_{\ell,m}$ and $Ett_{\ell,m}$ can be obtained from calculations performed on previous rows using the backward Euler approximations given by Equations (4.12) and (4.17):

$$Et_{\ell,m} \approx \frac{E_{\ell,m} - E_{\ell,m-1}}{h} \tag{4.33}$$

$$Ett_{\ell,m} \approx \frac{E_{\ell,m} - 2E_{\ell,m-1} + E_{\ell,m-2}}{h^2} \tag{4.34}$$

Substituting these approximations into Equation (4.27) creates an equation of the form:

$$Ex_{\ell,m} \approx f(E_{\ell,m}, E_{\ell,m-1}, E_{\ell,m-2}, Ex_{\ell,m-1}) \tag{4.35}$$

and therefore an estimate to $E_{\ell+1,m}$ can calculated from Equations (4.27) and (4.29) using the approximations given by Equations (4.33) and (4.34).

Using this method, a complete solution for $E_{\ell,m}$ can be obtained over the entire grid. All other desired quantities can then be calculated from $E_{\ell,m}$ using the relationships given at the end of Section 3.3.

4.3 "Cubic" Algorithm

The hybrid algorithm was found to have convergence problems under extremely high injection conditions. To allow investigation of photo-induced discharge under these conditions, a new algorithm has been developed that relies solely on the backward Euler approximations. This exclusive use of the backward Euler approximation gives the algorithm better inherent stability [12]. This method is presented below.

Consider the PID differential equation written in grid form (Equation 4.11):

$$E_{\ell,m}Ett_{\ell,m} + E^2_{\ell,m}Etx_{\ell,m} - (1+c)Et^2_{\ell,m} - cE_{\ell,m}Ex_{\ell,m}Et_{\ell,m} + (\omega + r)E_{\ell,m}Et_{\ell,m} + rE^2_{\ell,m}Ex_{\ell,m} = 0 \tag{4.11}$$

The derivatives can be removed from this equation by substituting the backward Euler approximations given by Equations (4.12), (4.13), (4.17), and (4.19):

$$E_{\ell,m}\left(\frac{E_{\ell,m} - 2E_{\ell,m-1} + E_{\ell,m-2}}{h^2}\right) + E^2_{\ell,m}\left(\frac{E_{\ell,m} - E_{\ell-1,m} - E_{\ell,m-1} + E_{\ell-1,m-1}}{hk}\right) - (1+c)\left(\frac{E_{\ell,m} - E_{\ell,m-1}}{h}\right)^2 - cE_{\ell,m}\left(\frac{E_{\ell,m} - E_{\ell-1,m}}{k}\right)\left(\frac{E_{\ell,m} - E_{\ell,m-1}}{h}\right) + (\omega + r)E_{\ell,m}\left(\frac{E_{\ell,m} - E_{\ell,m-1}}{h}\right) + rE^2_{\ell,m}\left(\frac{E_{\ell,m} - E_{\ell-1,m}}{k}\right) \approx 0 \tag{4.35}$$

Expanding and collecting gives a cubic polynomial in $E_{\ell,m}$:

$$AE^3_{\ell,m} + BE^2_{\ell,m} + CE_{\ell,m} + D = 0 \tag{4.36}$$

where

$$A = \frac{1-c}{hk} + \frac{r}{k} \tag{4.37}$$

$$B = \frac{E_{\ell-1,m-1} - E_{\ell-1,m} - E_{\ell,m-1}}{hk} - \frac{c}{h^2} + \frac{w+r}{h} - \frac{r}{k}E_{\ell-1,m} \tag{4.38}$$

$$C = \frac{E_{\ell,m-2} + 2cE_{\ell,m-1}}{h^2} + \frac{c}{hk}\left(E_{\ell,m-1} + E_{\ell-1,m}\right) - \frac{w+r}{h}E_{\ell,m-1} \tag{4.39}$$

$$D = -\frac{(1+c)}{h^2}E^2_{\ell,m-1} - \frac{c}{hk}E_{\ell-1,m}E_{\ell,m-1} \tag{4.40}$$

Therefore, a estimate to $E_{\ell,m}$ can be found by solving (4.36) using the coefficients given by Equations (4.37) through (4.40), which depend on the previous grid values $E_{\ell-1,m}$,

$E_{\ell-1,m-1}$, $E_{\ell,m-1}$, and $E_{\ell,m-2}$, as depicted in Figure 4.4 (b). If this equation is applied to the grid in sequence depicted by Figure 4.2, the values on previous points will always be known.

Equations (4.37) through (4.40) cannot be used to solve for $E_{\ell,m}$ if m=1, because the $E_{\ell,m-2}$ value required by Equation (4.39) does not lie on the grid. In this case, we can obtain a new set of coefficients for the polynomial by using a slightly different backward Euler approximation to $Ett_{\ell,m}$. Substituting Equation (4.12) into Equation (4.16) gives:

$$Ett_{\ell,m} \approx \frac{\frac{E_{\ell,m} - E_{\ell,m-1}}{h} - Et_{\ell,m-1}}{h} \tag{4.41}$$

Substituting Equations (4.12), (4.13), (4.19), and (4.41) into Equation (4.11) gives

$$E_{\ell,m}\left(\frac{\frac{E_{\ell,m} - E_{\ell,m-1}}{h} - Et_{\ell,m-1}}{h}\right) + E_{\ell,m}^2\left(\frac{E_{\ell,m} - E_{\ell-1,m} - E_{\ell,m-1} + E_{\ell-1,m-1}}{hk}\right)$$
$$-(1+c)\left(\frac{E_{\ell,m} - E_{\ell,m-1}}{h}\right)^2 - cE_{\ell,m}\left(\frac{E_{\ell,m} - E_{\ell-1,m}}{k}\right)\left(\frac{E_{\ell,m} - E_{\ell,m-1}}{h}\right) \tag{4.42}$$
$$+(\omega + r)E_{\ell,m}\left(\frac{E_{\ell,m} - E_{\ell,m-1}}{h}\right) + rE_{\ell,m}^2\left(\frac{E_{\ell,m} - E_{\ell-1,m}}{k}\right) \approx 0$$

Collecting and expanding terms containing powers of $E_{\ell,m}$ again gives a cubic equation of the form given by Equation (4.36). The coefficients A, B, D are the same as in the general case ($2 \le m \le MM$). The coefficient C for the case of m=1 is given by:

$$C = \frac{1+2c}{h^2}E_{\ell,m-1} - \frac{1}{h}Et_{\ell,m-1} + \frac{c}{hk}\left(E_{\ell,m-1} + E_{\ell-1,m}\right) - \frac{w+r}{h}E_{\ell,m-1} \tag{4.43}$$

For the case of m=1, an estimate to $E_{\ell,m}$ can then be found by solving (4.36) using the coefficients given by Equations (4.37), (4.38), (4.40), and (4.43) which depend on the previous grid values $E_{\ell-1,m}$, $E_{\ell-1,m-1}$, $E_{\ell,m-1}$, and $Et_{\ell,m-1}$, as depicted in Figure 4.4 (a). If this

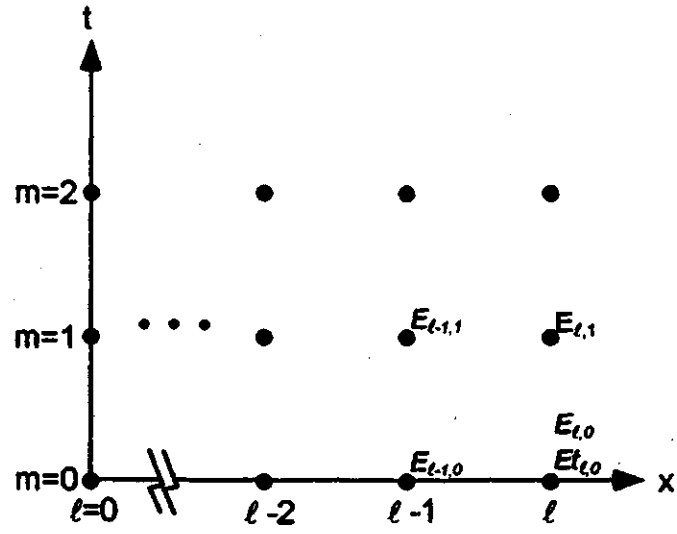

$$E_{\ell,1} = f(E_{\ell,0}, E_{\ell-1,1}, E_{\ell-1,0}, Et_{\ell,0})$$

(a) m=1, $1 \le \ell \le LL$

Note: Grid values shown in italics are known from boundary and initial conditions or prior iterations.

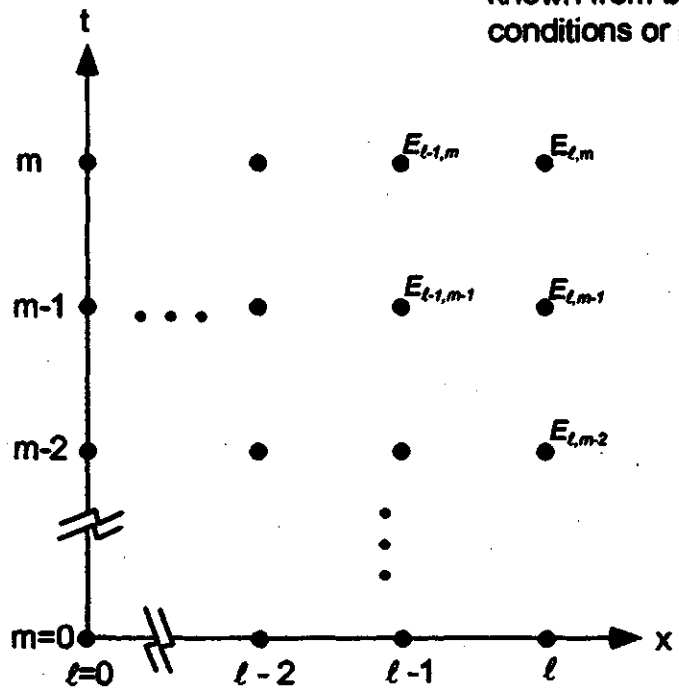

$$E_{\ell,m} = f(E_{\ell-1,m}, E_{\ell-1,m-1}, E_{\ell,m-1}, E_{\ell,m-2})$$

(b) $2 \le m \le MM$, $1 \le \ell \le LL$

Figure 4.4. "Cubic" solution method obtained using the backward Euler approximation.

equation is applied in ascending order on the m=1 row, as depicted by Figure 4.2, the values on previous points will be known..

The analytical method used to obtain the solutions to the cubic equation involves tedious algebra and is provided in Appendix A. A few comments are in order, however. The cubic equation, in general, has three roots. In this case, only one of the roots corresponds to the electric field value $E_{\ell,m}$. The correct root is chosen by selecting the root that: 1) is real; 2) is between 0 and 1, inclusive; and 3) is not much different from values of $E_{\ell,m}$ on neighboring grid points.

This method has been found to converge successfully under high injection situations. Under low injection conditions, the results were seen to be the same as those obtained using the hybrid algorithm. A detailed discussion of the results obtained using these two methods is provided in Chapter 5.

4.4 Computer Programs

Two computer programs were written that solve the photo-induced discharge differential equation using the algorithms described in the previous sections. The first program implements the hybrid algorithm, and the second implements the cubic algorithm. The programs are written in Pascal and were compiled and run on a Macintosh computer using Think Pascal, version 4.0. Both of the programs implement identical functionality. Only the core numerical algorithms are different. The features common to both of the programs are described below.

The programs solve for the electric field $E_{\ell,m}$ (i.e. E(x,t)) in a pulsed-illumination scenario under specified trapping and injection characteristics. Specifically, the programs allow the user to specify the following parameters:

(1) trapping parameters, ω, r, and c

(2) the fractional amount of charge remaining on the surface after illumination, φ

(3) the fractional injection depth parameter δ used in Equation (3.51)

(4) the time scale of the simulation, via the t_{max} parameter depicted in Figure 4.1

(5) the density of the grid via the MM and LL parameters depicted in Figure 4.1

Given these parameters, the programs will solve the entire grid for the electric field. Note that boundary and initial conditions are determined from the injection parameters φ and δ using Equations (3.44) through (3.49) and (3.51)

In order to obtain accurate solutions, the grid density parameters MM and LL often need to be quite large in order to guarantee that the approximations outlined in section 4.1 are accurate. In order to ensure that the solution for $E_{\tau,m}$ is accurate, the grid density parameters MM and LL are repetitively increased until there is no discernible change in the surface potential V(t) output by the computer programs. Since the surface voltage V(t) is related to the electric field E(x,t) by

$$V(t) = \int_0^1 E(x,t)dx \tag{4.44}$$

this guarantees the accuracy of the calculated electric field values (i.e. error in $E_{l,m}$). The exact values of MM and LL required vary depending on the trapping parameters and injection characteristics. High injection scenarios usually require extremely dense grid spacings (e.g. MM around 4000, LL as large as 20000), whereas low injection scenarios are less demanding (e.g. MM and LL around 4000).

The programs discussed in this section have been used to model a pulse-illuminated xerographic discharge under a wide variety of trapping and injection conditions. The results of these efforts are presented in Chapter 5.

5. RESULTS AND DISCUSSION

5.1 Introduction

The numerical technique described in Chapter 4 has been used to solve the PID partial differential Equation (3.31) under a variety of trapping and injection conditions. The computer programs which implement the numerical technique provide a solution for the normalized electric field, E(x,t).

The results presented in this chapter have been divided into three sections: low injection, high injection, and thermalization. In the low injection case, an extremely small amount of charge is injected into the sample. This amount of injection is representative of XTOF experiments performed on xerographic materials in attempts to determine their material properties. In the high injection case, injection strengths as high as 99% are used. Injection strengths of this magnitude are more representative of practical situations such as electroradiography with laser scanned read-out where a high intensity laser beam is scanned across the sample. Thermalization results are of interest because they explain a variety of phenomena which will be discussed in the low injection results. In each case, the effects of varying the trapping parameters ω, r, and c have been examined.

It has been established that the grid described in Chapter 4 must contain around 10 million points in order for accurate solutions to be obtained. Analysis of the entire set of electric field data is obviously intractable due to the sheer volume of data. In order to simplify the analysis, several features have been incorporated into the programs

which implement the solution algorithms. In Chapter 3, we saw that the trapped and untrapped charge densities can be calculated from the electric field through Equations (3.33) and (3.34):

$$p(x,t) = -\frac{1}{E(x,t)}\frac{\partial E(x,t)}{\partial t} \tag{3.33}$$

$$p_t(x,t) = \frac{\partial E(x,t)}{\partial x} + \frac{1}{E(x,t)}\frac{\partial E(x,t)}{\partial t} \tag{3.34}$$

The programs allow the charge densities to be calculated and output at an arbitrary list of times which are specified by the user. This allows one to examine how the charge packets evolve as they travel through the film. To further automate the analysis of this data, the program finds and records the positions and magnitudes of the charge packet peak and half-maxima at these times. These data can be used to determine the velocity of the charge packet and to examine how the charge packet changes with time.

The programs also calculate and output the normalized surface voltage V(t) and its derivatives dV/dt and d^2V/dt^2 at specified intervals throughout the discharge. The surface voltage is calculated by numerically integrating the electric field, i.e.

$$V(t) = \int_0^1 E(x,t)dx \tag{5.1}$$

which can be approximated using the electric field values at the grid points and the trapezoidal rule:

$$V_m = V(mh) \cong \frac{1}{2}\sum_{\ell=0}^{LL-1}\left(E_{\ell-1,m} + E_{\ell,m}\right) \tag{5.2}$$

The derivatives can be approximated using the forward Euler approximation:

$$Vt_m \equiv \left.\frac{dV(t)}{dt}\right|_{t=mh} \cong \frac{V_{m+1} - V_m}{h} \tag{5.3}$$

$$Vtt_m \equiv \left.\frac{d^2V(t)}{dt^2}\right|_{t=mh} \cong \frac{Vt_{m+1} - Vt_m}{h} \tag{5.4}$$

The time evolution of the surface potential is of particular interest for two reasons: 1) it is a quantity that can be directly measured in xerographic experiments, and 2) properties of its time derivatives provide insight into the mechanics of the charge transport process. In the next section, we will see that the first derivative, dV/dt, is of particular interest because its properties are directly related to the shape, density, and velocity of the trapped and untrapped charge packets.

5.2 Basic Concepts

In order to fully appreciate the results presented in this chapter, a detailed understanding of the relationship between the trapped and untrapped charge densities and the surface voltage is required. To achieve this goal, it is useful to consider what occurs in the case of a generalized discharge.

In the model presented in Chapters 3 and 4, a packet of untrapped carriers is injected into a thin region near the surface (x=0). The normalized amount of charge remaining on the surface is denoted as φ, thereby fixing the amount of injected charge at $1-\varphi$. The injected charge packet then drifts across the sample towards the substrate, thereby discharging the sample. As the packet traverses the sample, it interacts with a single layer of traps that is characterized by a set of trap capture, release, and saturation constants, denoted ω, r, and c. Once the injected charge packet has left the sample, the amount of charge remaining on the surface, φ, fixes the final normalized surface voltage at φ. Therefore, during the course of the discharge, the normalized surface voltage has been reduced from 1 to φ. In a xerographic discharge, the discharge is often monitored

by measuring the rate of change of the surface voltage, dV/dt. Subsequent discussions will establish the detailed relationship that exists between dV/dt and the evolution of the injected charge packet.

If the explicit behaviour of the trapped and untrapped charge packets is known (i.e. $p(x,t)$, $p_t(x,t)$ are known), we can solve for the surface voltage V(t) and its derivative, dV(t)/dt, as follows. Using Equation (3.16) and the boundary conditions given by Equation (3.47), we can derive a general expression for the electric field:

$$E(x,t) = \varphi + \int_0^x \left(p(u,t) + p_t(u,t)\right)du \tag{5.5}$$

This equation can be written more simply as

$$E(x,t) = \varphi + \int_0^x \rho(u,t)du \tag{5.6}$$

where $\rho(x,t) = p(x,t) + p_t(x,t)$

The surface voltage V(t) is then given by

$$V(t) = \int_0^1 E(x,t)dx \tag{5.7}$$

and hence the time derivative dV/dt is given by

$$\frac{dV(t)}{dt} = \frac{d}{dt}\left(\int_0^1 E(x,t)dx\right) \tag{5.8}$$

The consequences of these relationships can be illustrated by presenting a few examples. Consider the scenario depicted in Figures 5.1 and 5.2. In this example, a relatively narrow charge packet is traversing the film. The fractional amount of charge remaining on the surface is φ=0.999, fixing the fractional amount of injected charge at 0.001.

The total charge density is plotted at various different times on the left-hand side of Figure 5.1. We can make a few general observations. Note that the packet travels a normalized distance of 0.2 in a normalized time of 20. This sets the packet velocity at

$$v_p = \frac{\Delta x}{\Delta t} = \frac{0.2}{20} = 0.01 \tag{5.9}$$

The packet velocity is determined by the selection of trapping parameters. This relationship will be discussed in detail in later sections. This velocity of 0.01 implies that the transit time is $1/v_p = 100$, which can be confirmed by observing that the charge packet is just leaving the film at t=100. At t=140, the packet has completely left the sample. Note that the charge packet spreads as it passes through the film. We will see in later sections that is the result of interaction with traps.

The solution to Equation (5.6) subject to these charge densities is shown on the right-hand side of Figure 5.1. Plots of $E(x,t) - \varphi$ vs. x are shown to emphasize the effect of the second term of Equation (5.6). Note that in each case, $E(x,t) - \varphi$ rises from 0 to 0.001 at the position of charge packet. This rise is identically equal to the amount of injected charge, $1 - \varphi$, due to the "integral" relationship between $\rho(x,t)$ and $E(x,t)$. This also implies that the abruptness of the rise in $E(x,t) - \varphi$ is related to the width of the charge packet. As the charge packet traverses through the film, the rise in $E(x,t) - \varphi$ moves through the film with a velocity that is equal to that of the charge packet. At t=140, the packet has left the film and $E(x,t) - \varphi$ is equal to 0 throughout the sample.

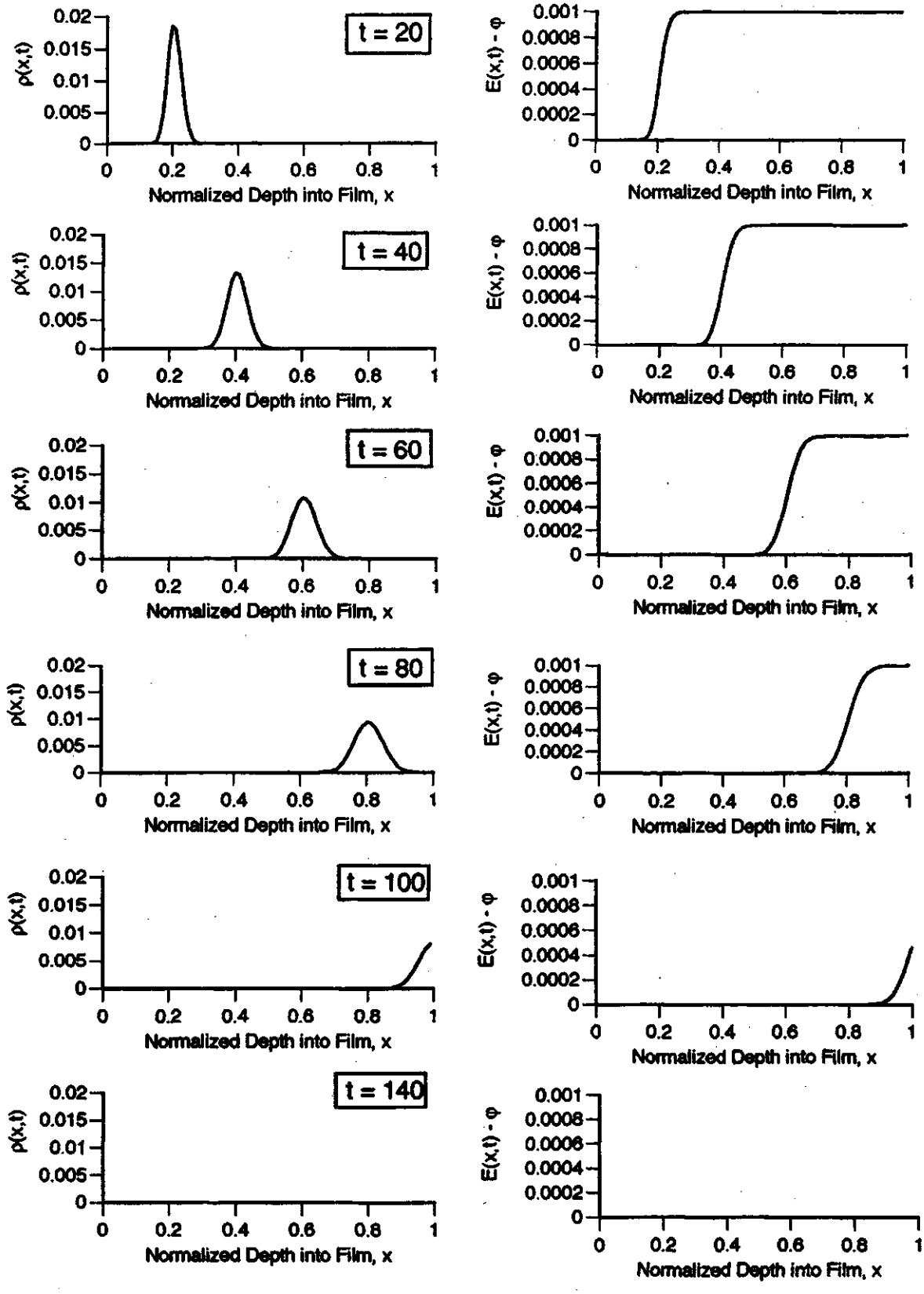

Figure 5.1. Normalized charge density and electric field at various times throughout the discharge for a narrow charge packet with a normalized transit time of 100. The fractional amount of injection is 0.001 (i.e. $\varphi = 0.999$).

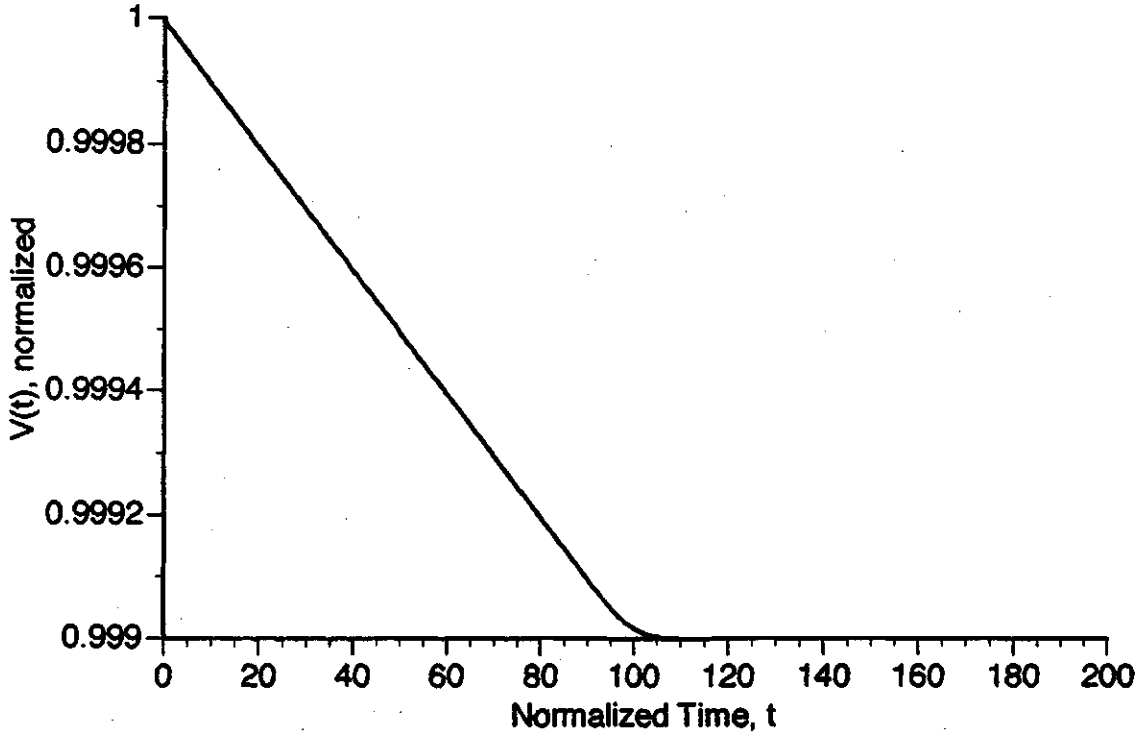

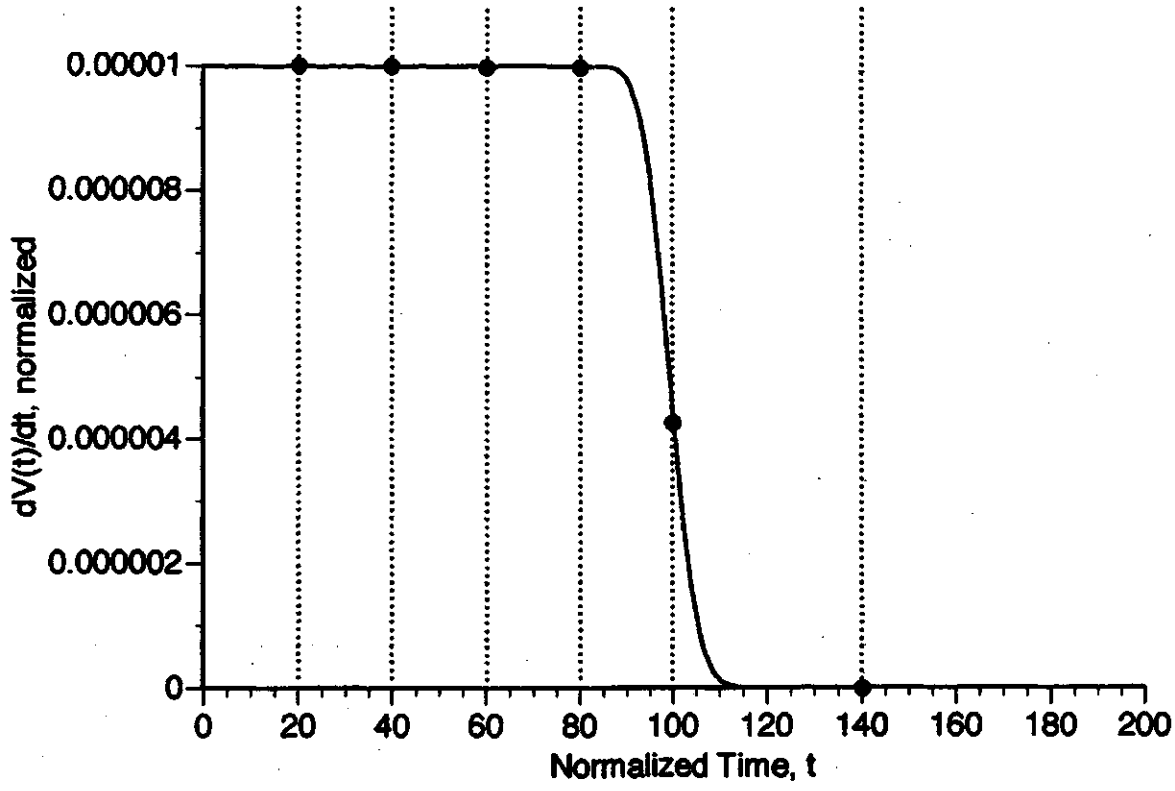

Figure 5.2. Normalized surface voltage and its time derivative for the case of a narrow charge packet with a normalized transit time of 100. The fractional amount of injection is 0.001 (i.e. φ =0.999). The dashed lines indicate the times shown in Figure 5.1.

Plots of V(t) and dV(t)/dt for this situation are shown in Figure 5.2. The times depicted in Figure 5.1 are shown with dashed lines. Stated simply, V(t) is the area under the E(x,t) curve and dV(t)/dt is the rate of change of that area with time. In Figure 5.1 we saw that the rise of 1- φ in E(x,t) - φ moved with a constant velocity that was equal to that of the charge packet, v_p. Using these facts, we can determine an approximation for Equation (5.8):

$$\frac{dV(t)}{dt} = \frac{d}{dt}\left(\int_0^l E(x,t)dx\right) \cong (1-\varphi)v_p \qquad (5.10)$$

In this case, we obtain $(1-\varphi)v_p$ = (1-0.999) * 0.01 = 0.00001. Figure 5.2 confirms this approximation, since V(t) drops with a constant rate equal to 0.00001 for times less than t=80. The approximation given by Equation (5.10) becomes invalid when the charge packet and hence the rise in E(x,t) - φ starts exiting the film near t=100. At this point, the rate of change of the area under E(x,t) - φ starts to drop, causing a corresponding drop in dV/dt. Once the packet has left the film, e.g. at t=140, the area under E(x,t) - φ no longer changes and dV/dt is equal to zero.

The effect of the width of the packet can be examined by considering another example, which is depicted in Figures 5.3 and 5.4. In this example, the injection parameter is the same (i.e. φ=0.999), but trapping parameters have been selected to give a wider charge packet with the same velocity of v_p = 0.01. Note that the rise in E(x,t) - φ is less sharp. The effect of this can be seen by examining Figure 5.4. The derivative dV/dt is still equal to the predicted value of 0.00001 for times less than t=60. However, the gentler rise in E(x,t) - φ causes the drop in dV/dt to be more gradual.

From these two examples, we can make the following conclusions. If a packet with a total charge content of 1 - φ is located entirely within the sample and is moving

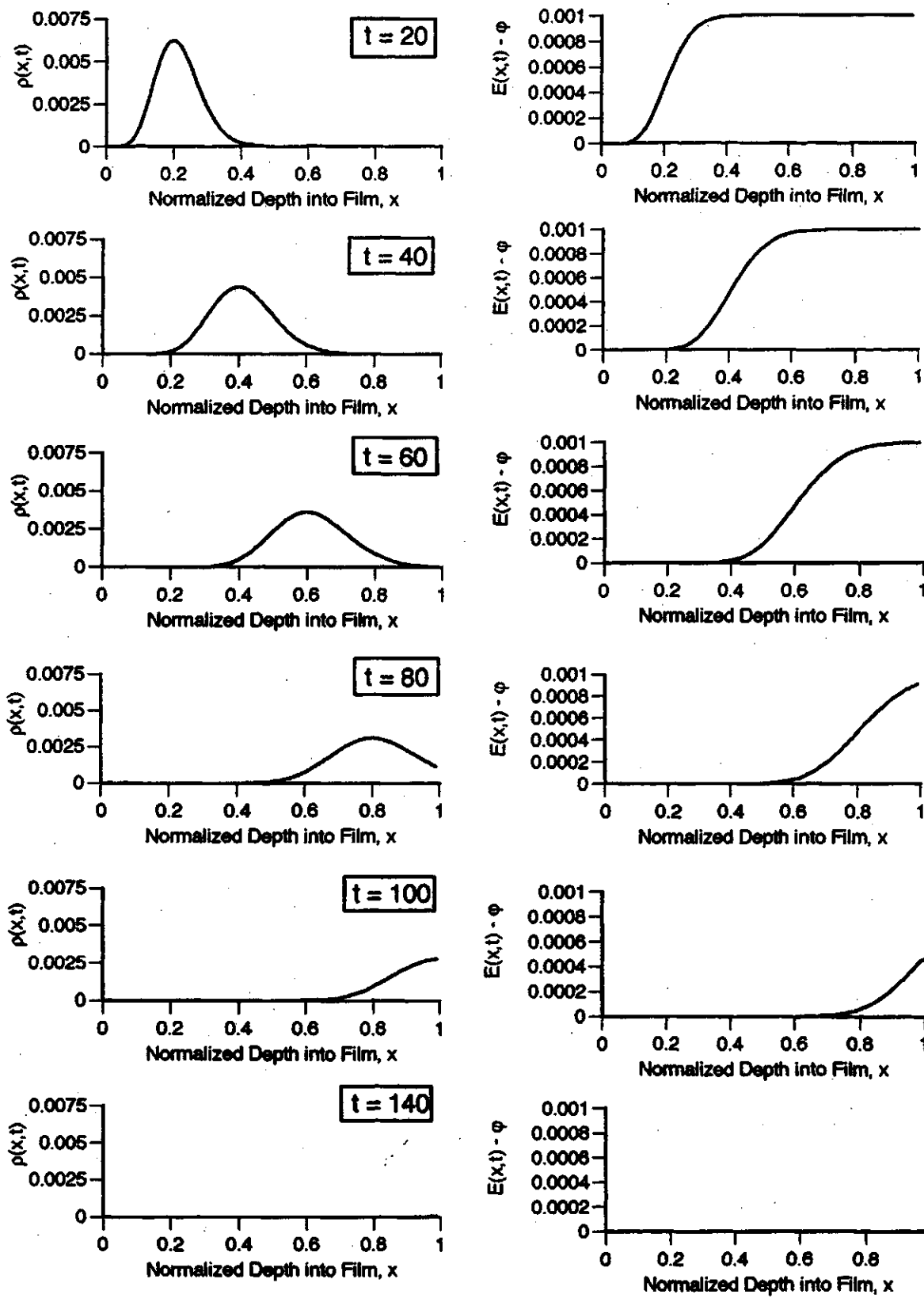

Figure 5.3. Normalized charge density and electric field at various times throughout the discharge for a wide charge packet with a normalized transit time of 100. The fractional amount of injection is 0.001 (i.e. $\varphi = 0.999$).

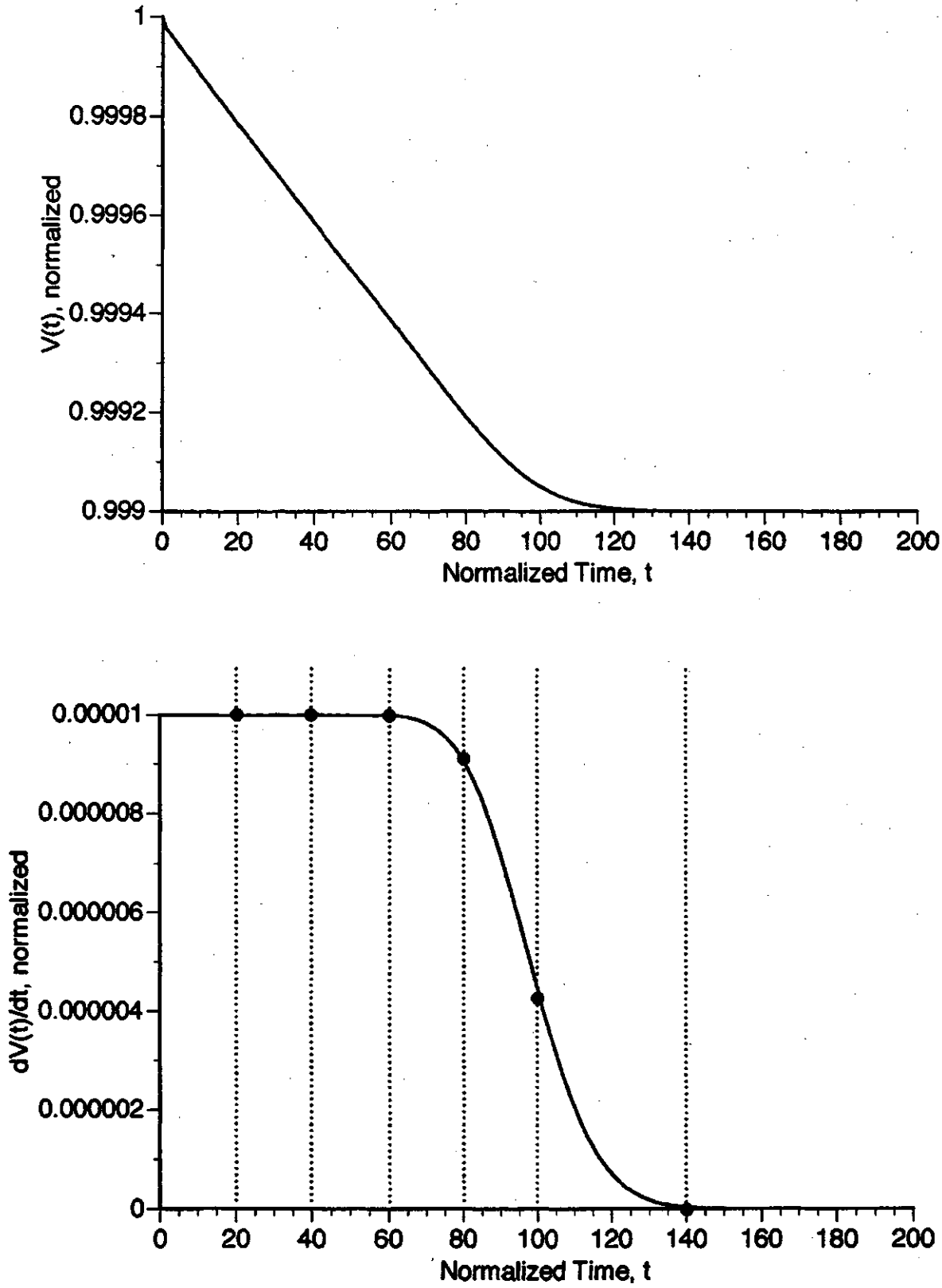

Figure 5.4. Normalized surface voltage and its time derivative for the case of a wide charge packet with a normalized transit time of 100. The fractional amount of injection is 0.001 (i.e. $\varphi = 0.999$). The dashed lines indicate the times shown in Figure 5.3.

with a velocity of v_p, dV/dt can be approximated by $(1-\varphi)v_p$. The behaviour of dV/dt near the transit time is determined by the shape of the charge packet. If the packet is narrow, the drop in dV/dt near the transit time is abrupt. If the packet is wide, the drop in dV/dt is gradual. These conclusions are important, because they illustrate that information about the shape and velocity of the charge packet can be obtained from dV/dt.

In the preceding discussion, the mechanisms which affect the shape of the charge packet were not discussed. Subsequent sections will illustrate that the shape of the charge packet depends on both the strength of the injection (i.e. on 1- φ) and on the trapping parameters ω, r, and c.

5.3 Low Injection

In order to simulate a pulse illuminated discharge under low injection conditions, the "wedge" shaped initial untrapped charge distribution described in Chapter 3 is used:

$$p(x,0) = \begin{cases} \dfrac{400(1-\varphi)x}{19\delta^2}, & 0 \le x < \dfrac{\delta}{20} \\ \dfrac{20(1-\varphi)}{19\delta}, & \dfrac{\delta}{20} \le x < \dfrac{19\delta}{20} \\ \dfrac{400(1-\varphi)(\delta-x)}{19\delta^2}, & \dfrac{19\delta}{20} \le x < \delta \\ 0, & x \ge \delta \end{cases} \qquad (5.11)$$

The fractional amount of charge left on the surface, φ, is set to 0.999, reflecting an injection strength of 0.1 %. The width parameter δ was set to 0.01, indicating that the initial injected charge resides in a region near the surface that is 1% of the sample thickness. The trapping parameters are set to a variety of different values in order to investigate their effect on the trapped and untrapped charge packets.

In chapter 2, an assertion was made that the microscopic mobility μ_o is reduced by a factor θ given by

$$\theta = \frac{t_c}{t_c + t_r} \tag{5.12}$$

where t_c and t_r are the unnormalized capture and release lifetimes of a set of traps. This assertion is only valid if these lifetimes are much shorter than the microscopic transit time, i.e. $t_c, t_r << t_o$. The validity of this statement will be evaluated in this section. In order to use modeling results to test Equation (3.52), it must be rewritten in terms of the normalized capture and release rates, ω and r. Substituting the definitions of ω and r given in Equation (3.29) into Equation (3.52) gives

$$\theta = \frac{\frac{t_o}{\omega}}{\frac{t_o}{\omega} + \frac{t_o}{r}} \times \frac{\frac{\omega r}{t_o}}{\frac{\omega r}{t_o}} = \frac{r}{r + \omega} \tag{5.13}$$

The condition for validity, $t_c, t_r << t_o$ now becomes $\omega, r >> 1$ when the equation is written in this form. Under these circumstances, we would expect the packet velocity to be reduced by the same value θ and the transit time to be increased by $1/\theta$.

Several sets of ω and r values were chosen, and the PID differential equation (3.31) was solved in each case using the methods described in Chapter 4. Typical ω and r values were chosen with the following objectives in mind:

(1) to examine how the velocity and shape of the charge packet and hence the behaviour of dV/dt vary with the magnitude of the trapping and release rates, ω and r, and

(2) to examine how the velocity and shape of the charge packet and hence the behaviour of dV/dt vary with the magnitude of the mobility reduction factor, θ.

The effect of the charge packet shape on the behaviour of dV/dt near the transit time will also be investigated. The values of ω and r chosen for use in simulations are shown in Table 5.1. Notice that for each value of θ, there are multiple sets of ω and r parameters, each with different strengths. This allows an independent examination of the effect of θ and the magnitude of ω and r. The trap saturation constant, c, was set equal to zero in all low injection simulations because trap saturation is not a significant effect. Trap saturation will be examined when high injection scenarios are considered.

Table 5.1. Trapping and release parameters used in low injection simulations.

Mobility Reduction Factor, θ	Trap Capture Rate, ω	Trap Release Rate, r
0.01	990	10
	495	5
	198	2
	99	1
0.02	490	10
	245	5
	98	2
	49	1
0.05	190	10
	95	5
	38	2
	19	1
0.1	90	10
	45	5
	18	2
	9	1
0.2	40	10
	20	5
	8	2
0.5	10	10
	5	5

First, let us examine the effect of varying θ in the case where the trapping parameters are large. The results obtained with r=10 are shown in Figures 5.5 through 5.9. Note that in these cases both parameters are much larger than 1 and we would expect the concept of a mobility reduction factor to be valid. In order to test this concept, the packet velocity and transit time have been calculated for the data depicted in Figures 5.5 through 5.9, and are listed in Table 5.2. The packet velocity was determined based on the velocity of the peak of the untrapped charge packet. The transit time is set by locating the inflection point in dV/dt (i.e. the maxima in d^2V/dt^2). The theoretical mobility reduction factor and its reciprocal are also listed for comparison purposes.

Table 5.2. Comparison of mobility reduction factor, packet velocity, and transit time.

Figure	ω	r	θ	packet velocity comparison		$1/\theta$	transit time comparison	
				v_p	% diff.		transit time	% diff.
5.5	990	10	0.01	0.009975	0.25	100	99.25	0.75
5.6	490	10	0.02	0.0199	0.5	50	49.5	1
5.7	190	10	0.05	0.049875	0.25	20	19.65	1.75
5.8	90	10	0.1	0.09975	0.25	10	9.71	2.9
5.9	40	10	0.2	0.2005	0.25	5	4.745	5.1

Note that in each case, the packet velocity is within 0.5% of the mobility reduction factor. This is the expected result because the solution is performed using normalized variables, i.e. a packet velocity and transit time of 1 corresponds to the no trapping situation.

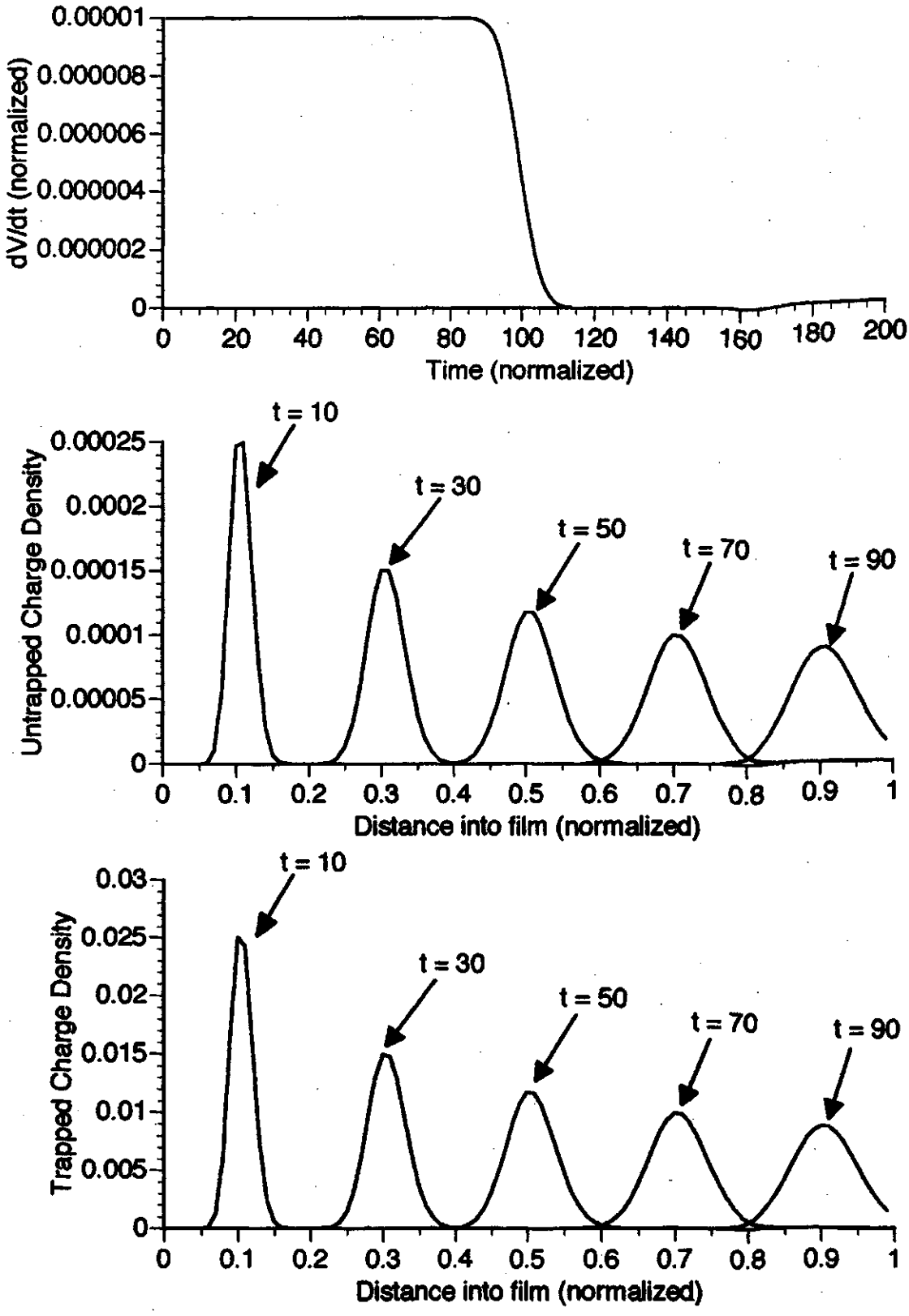

Figure 5.5. Low injection simulation results obtained with $\omega = 990$, $r = 10$, and $\theta = 0.01$.

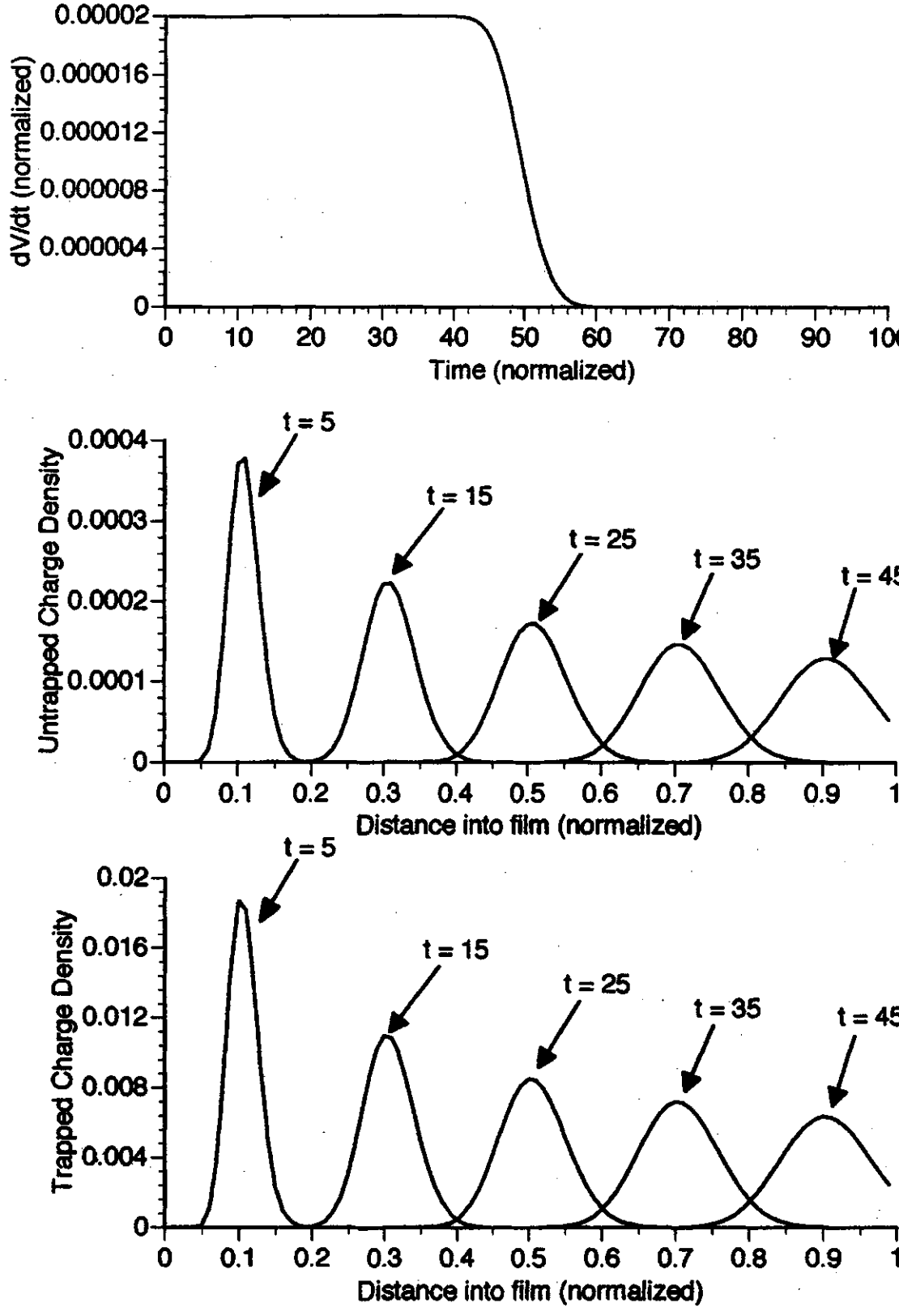

Figure 5.6. Low injection simulation results obtained with $\omega = 490$, $r = 10$, and $\theta = 0.02$.

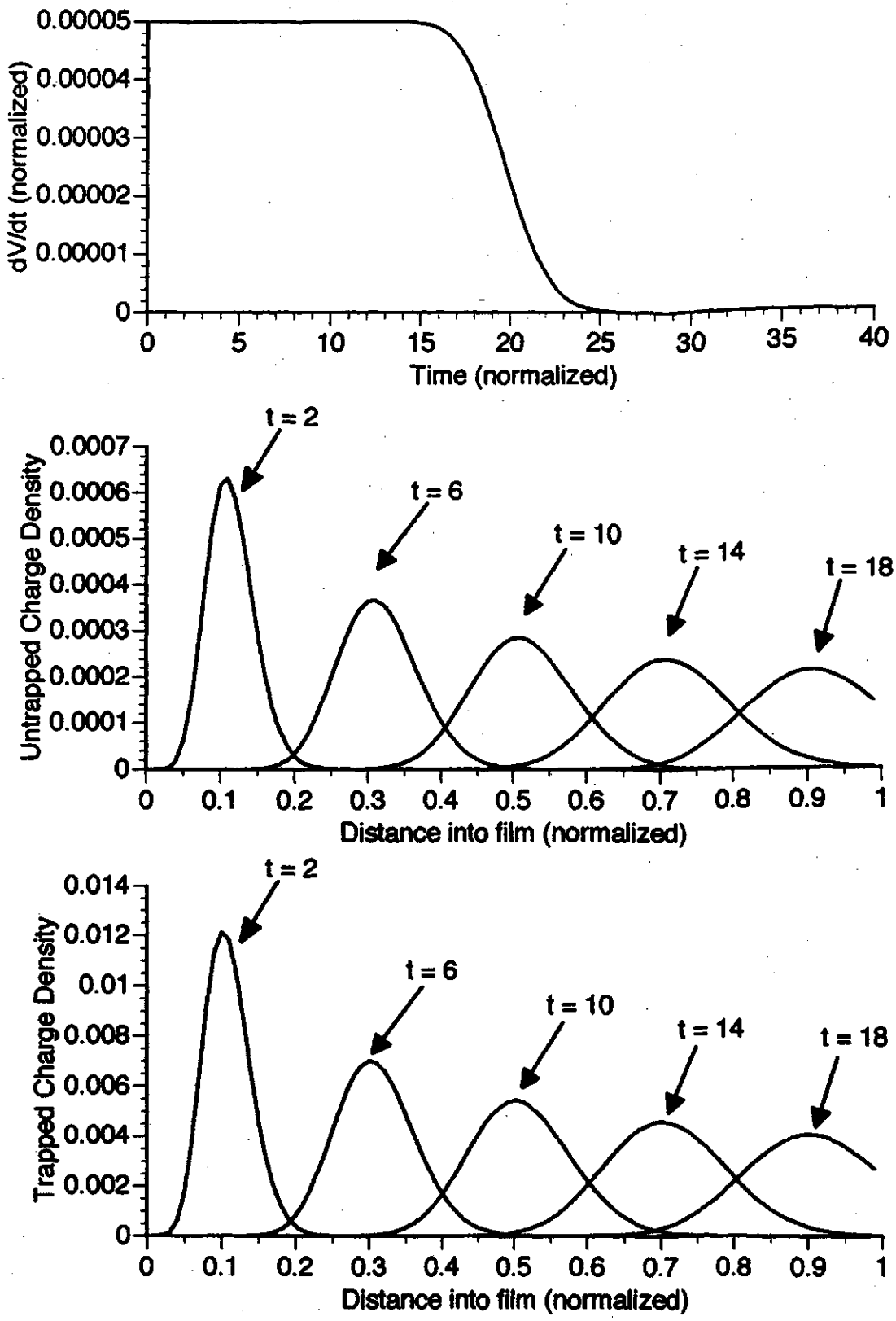

Figure 5.7. Low injection simulation results obtained with $\omega = 190$, $r = 10$, and $\theta = 0.05$.

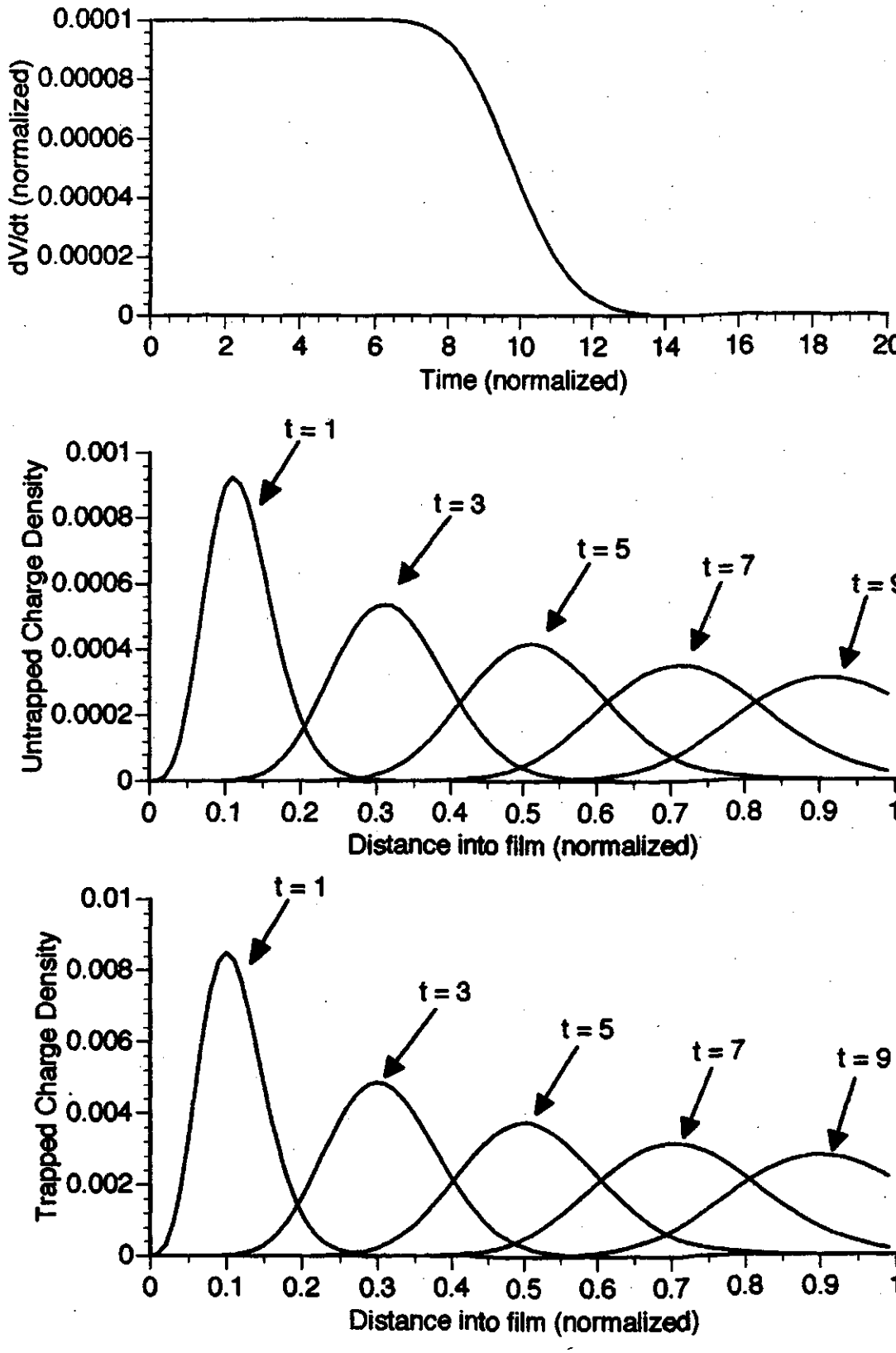

Figure 5.8. Low injection simulation results obtained with $\omega = 90$, $r = 10$, and $\theta = 0.1$.

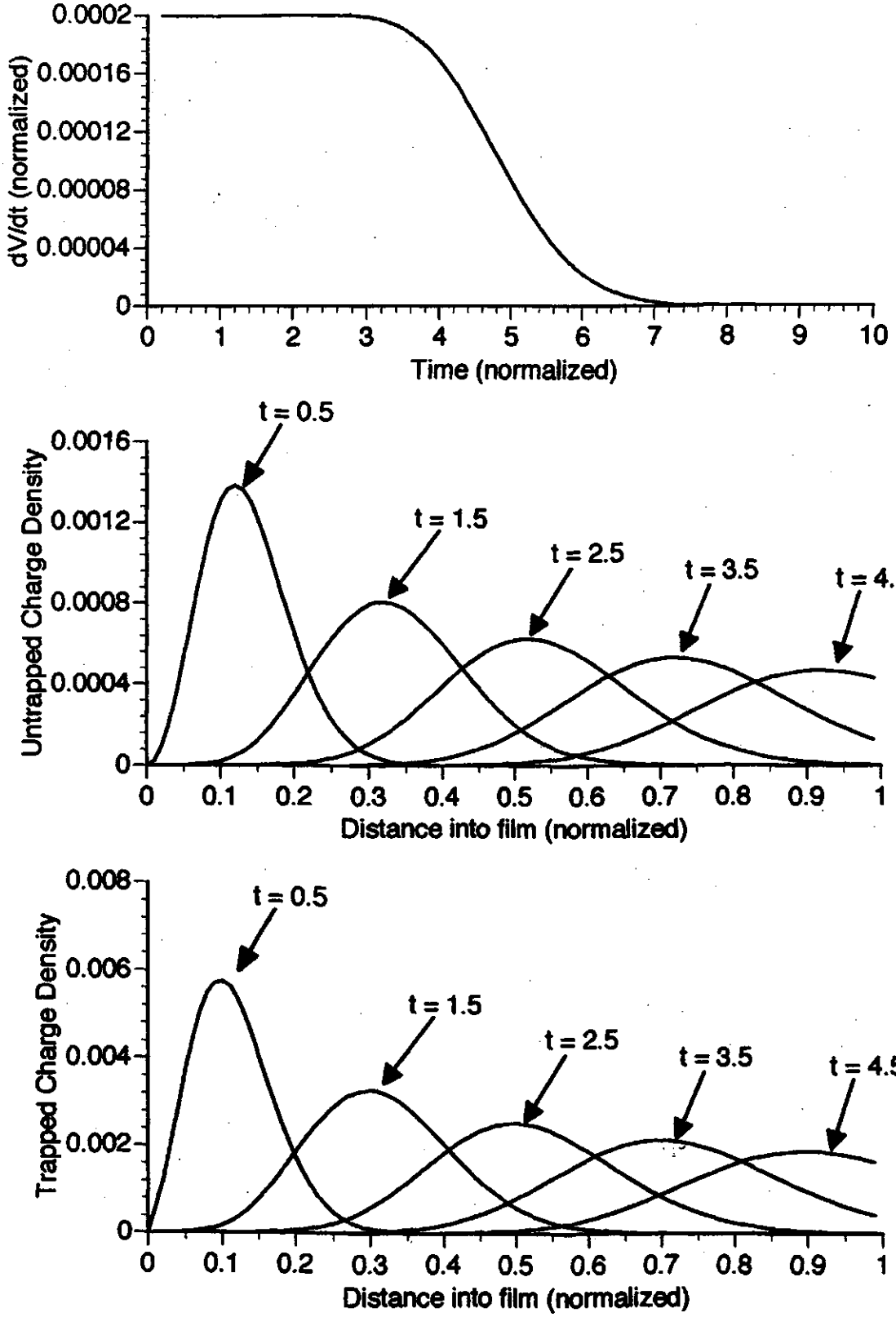

Figure 5.9. Low injection simulation results obtained with $\omega = 40$, $r = 10$, and $\theta = 0.2$.

Note that the transit time is in good agreement with the theoretical value of $1/\theta$ for large values of ω, but is only within 5% for smaller values. This is due to an effect called "thermalization" that occurs at the beginning of the discharge. This effect will be discussed in detail later in this chapter. Also note that the concept of a well-defined transit time is more appropriately applied to small values of θ where the transition in dV/dt at the transit time is more abrupt.

It is also expected that the value of dV/dt before the packet starts exiting the film should be governed by the relationship given in Equation (5.10). If we replace the packet velocity with the mobility reduction factor, which is supported by the data presented in Table 5.2, the predicted pre-transit time values for dV/dt are given by $\theta(1-\varphi)$. The pre-transit time value of dV/dt for the data depicted in Figures 5.5 through 5.9 and the values predicted by this relation are tabulated in Table 5.3. Recall that the value of φ used for all low injection simulations is 0.999.

Table 5.3. Comparison of $\theta(1-\varphi)$ and the pre-transit time dV/dt value

Figure	ω	r	θ	$\theta(1-\varphi)$	Pre-Transit Time dV/dt value	% diff
5.5	990	10	0.01	0.00001	0.00001000	0
5.6	490	10	0.02	0.00002	0.00001999	0.05
5.7	190	10	0.05	0.00005	0.00004998	0.04
5.8	90	10	0.1	0.0001	0.00009996	0.04
5.9	40	10	0.2	0.0002	0.00019991	0.045

The pre-transit time dV/dt values generated by the model are obviously in excellent agreement with the predicted value of $\theta(1-\varphi)$. This is due to the fact that the injection is extremely weak, causing the entire charge packet to move with the same velocity. This is not the case in high injection situations, which will be discussed later. The slight discrepancy between the modeled values and the values predicted by $\theta(1-\varphi)$ is due to

the fact that the initial injected charge packet has a finite width and therefore does not start drifting at x=0.

Figures 5.5 through 5.9 illustrate how the trapped and untrapped charge packets evolve as they pass through the film for the case of r=10. In each case, the packets are shown at times when they are 10%, 30%, 50%, 70% and 90% through the thickness of the film. These points correspond to different times, depending on the value of θ. Examination of these figures allows some general observations to be made. The first is that the dispersion of the trapped and untrapped charge packets increases with increasing θ (i.e. with decreasing ω). This fact may seem counter-intuitive upon first inspection, since larger values of θ give rise to shorter discharges. One would think that the amount of dispersion would be proportional to the duration of the discharge, implying that dispersion would decrease with increasing θ. Figures 5.10 through 5.13 illustrate the effect of decreasing ω and r but keeping θ constant. A comparison with Figures 5.5 through 5.8 shows that the dispersion of the charge packet increases with decreasing ω and r if θ is held constant.

Earlier in this chapter, it was pointed out that the shape of the charge packet is linked to the shape or "dispersion" of the dV/dt waveform near the transit time. From observations made previously, it is obvious that changing θ, ω, and r will affect the shape of dV/dt. In order to characterize this dependence, a quantitative method for measuring the dispersion in dV/dt has been devised. This method is shown in Figure 5.14. The percent dispersion of the dV/dt waveform as a function of θ is shown for various values of r in Figure 5.15. Note that the dispersion increases with increasing θ and with decreasing r if θ is held constant. This observation is in line with observations made on the charge packets shown in Figures 5.5 through 5.13.

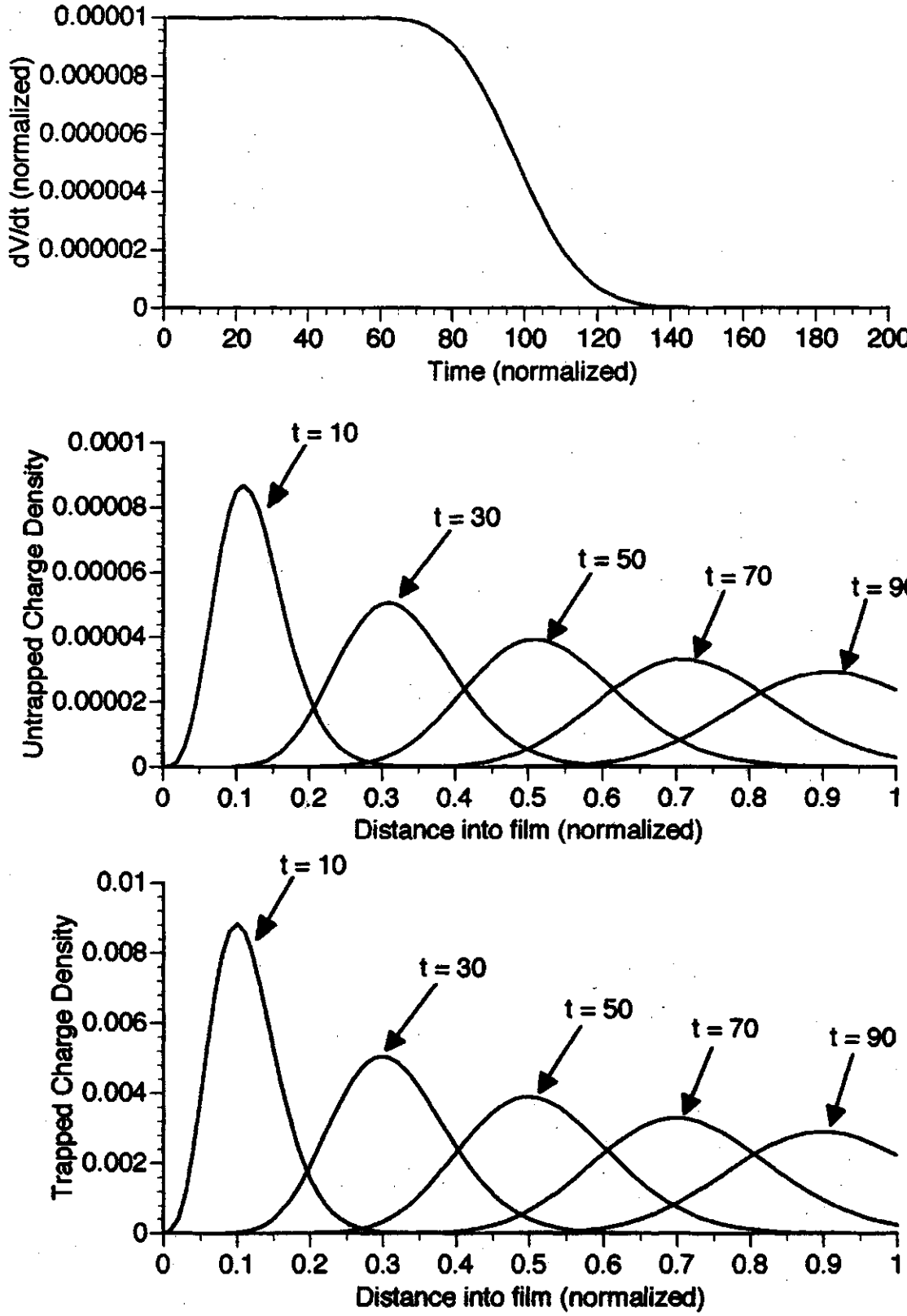

Figure 5.10. Low injection simulation results obtained with $\omega = 99$, $r = 1$, and $\theta = 0.01$.

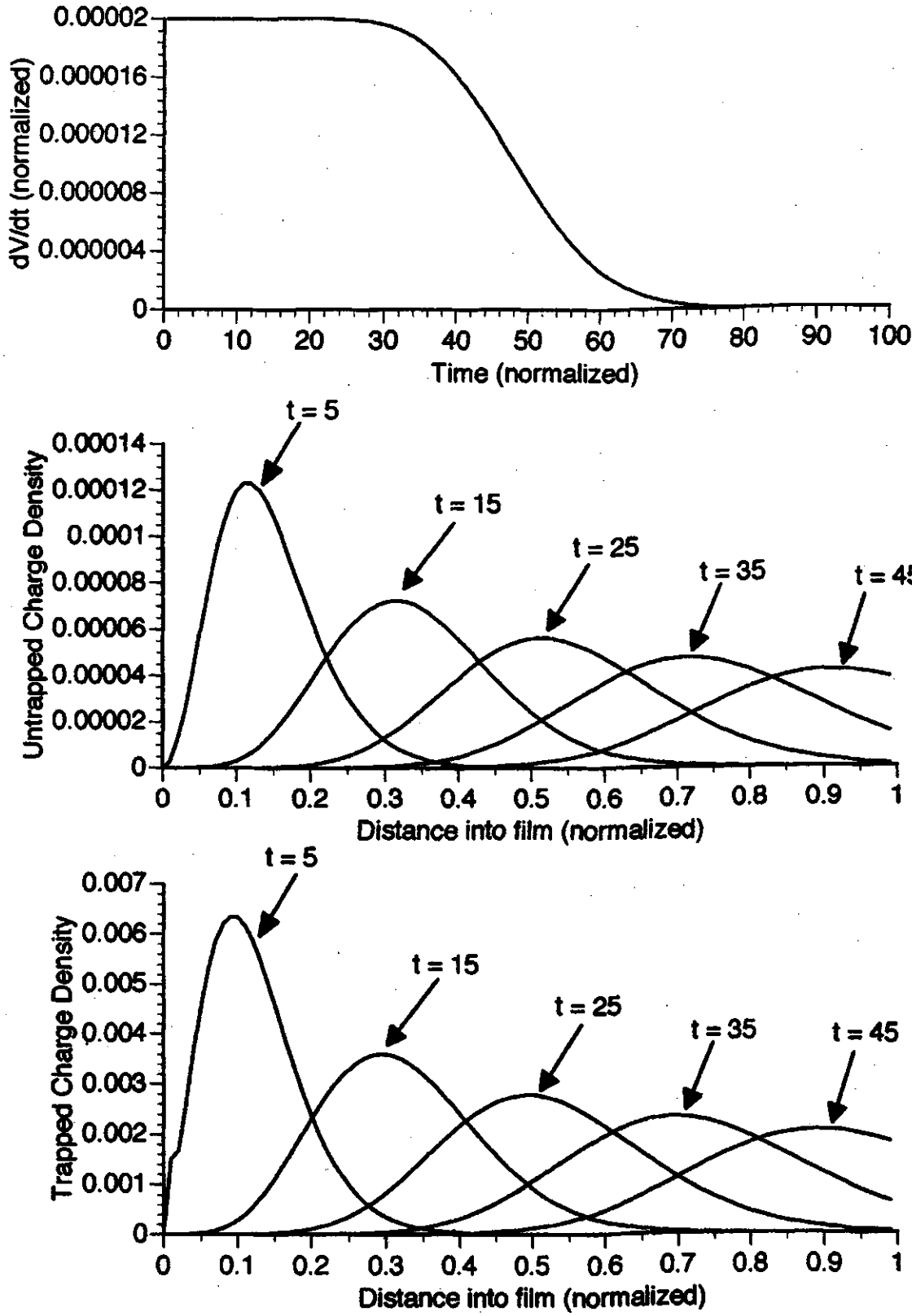

Figure 5.11. Low injection simulation results obtained with $\omega = 49$, $r = 1$, and $\theta = 0.02$.

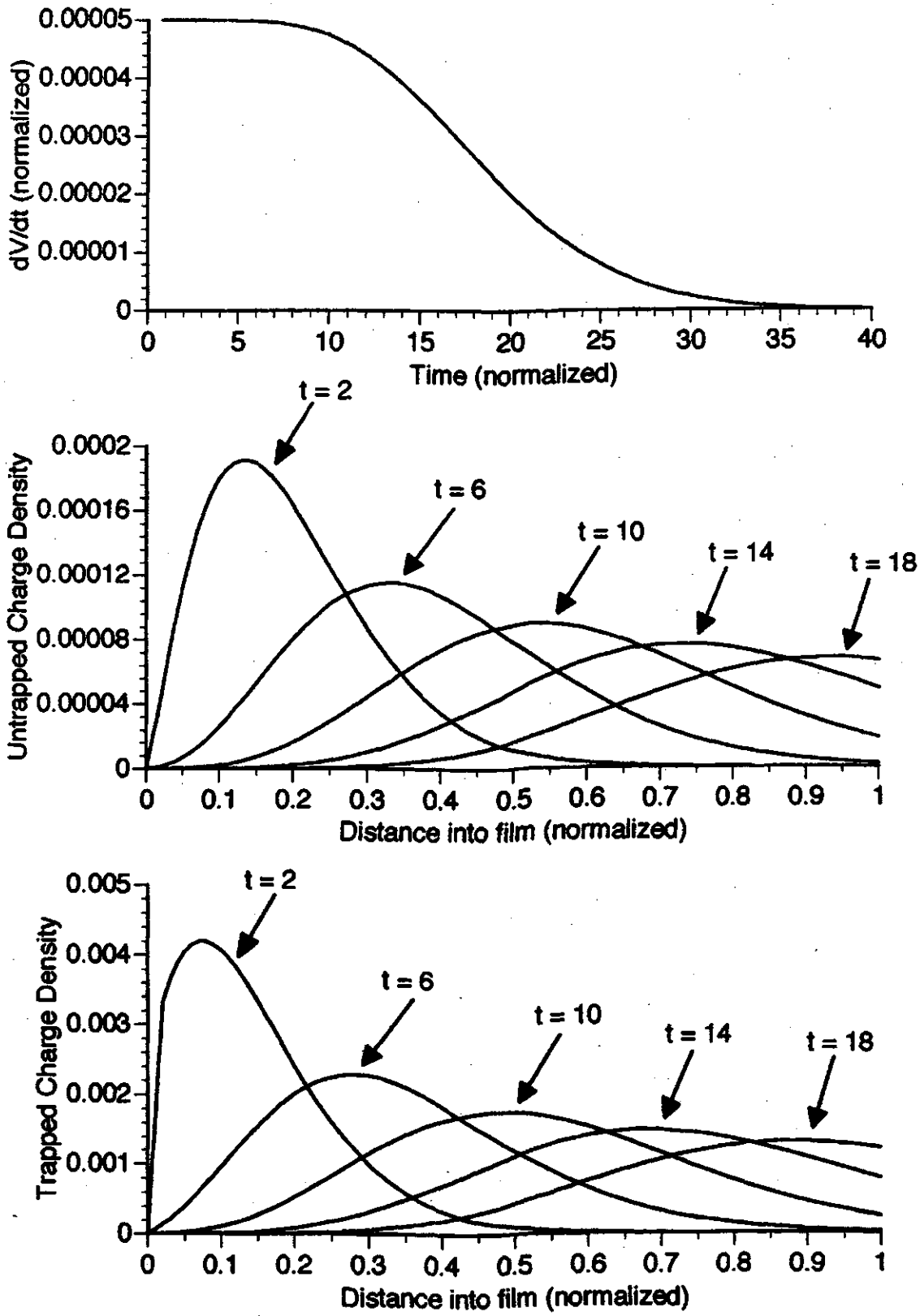

Figure 5.12: Low injection simulation results obtained with $\omega = 19$, $r = 1$, and $\theta = 0.05$.

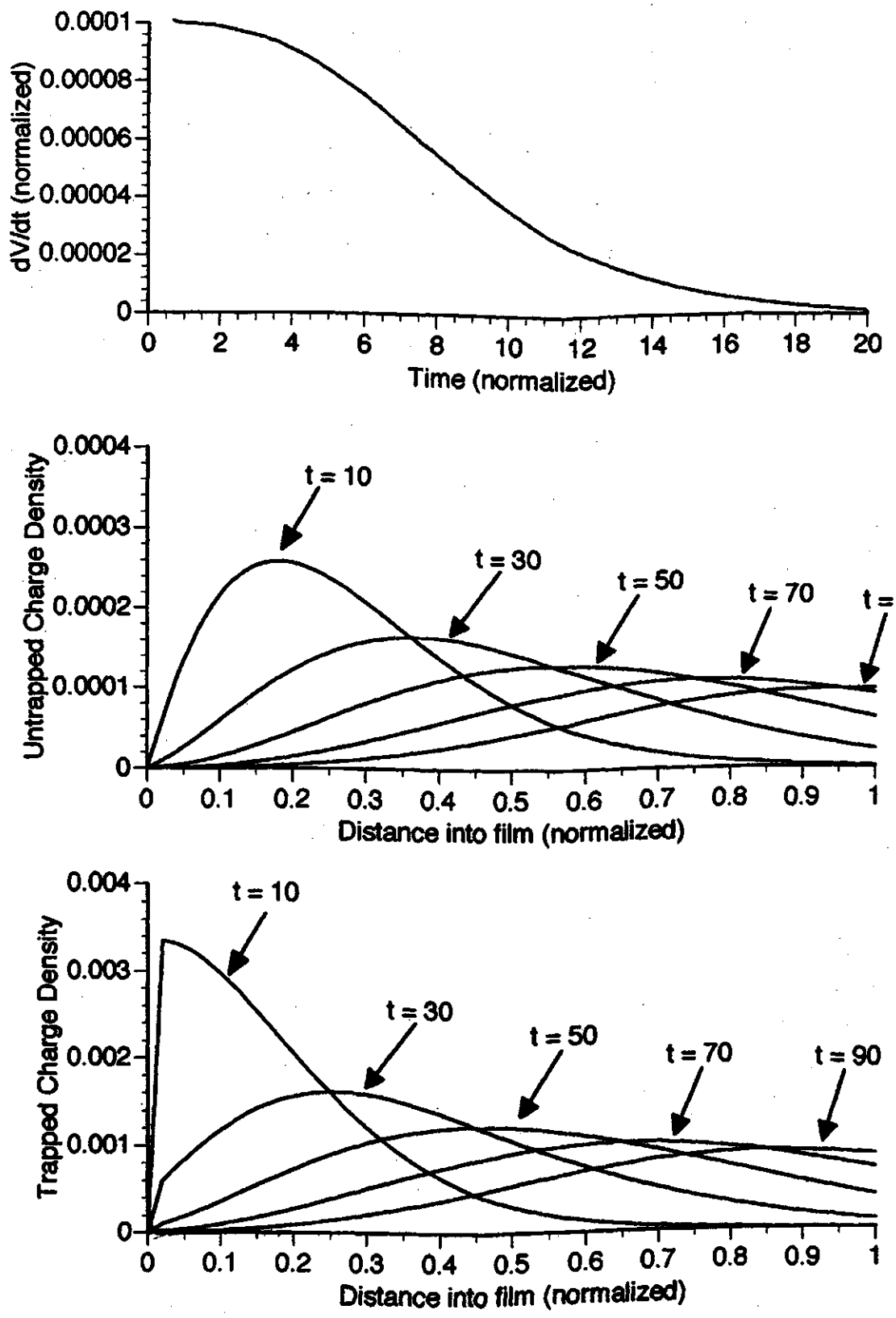

Figure 5.13. Low injection simulation results obtained with $\omega = 9$, $r = 1$, and $\theta = 0.1$.

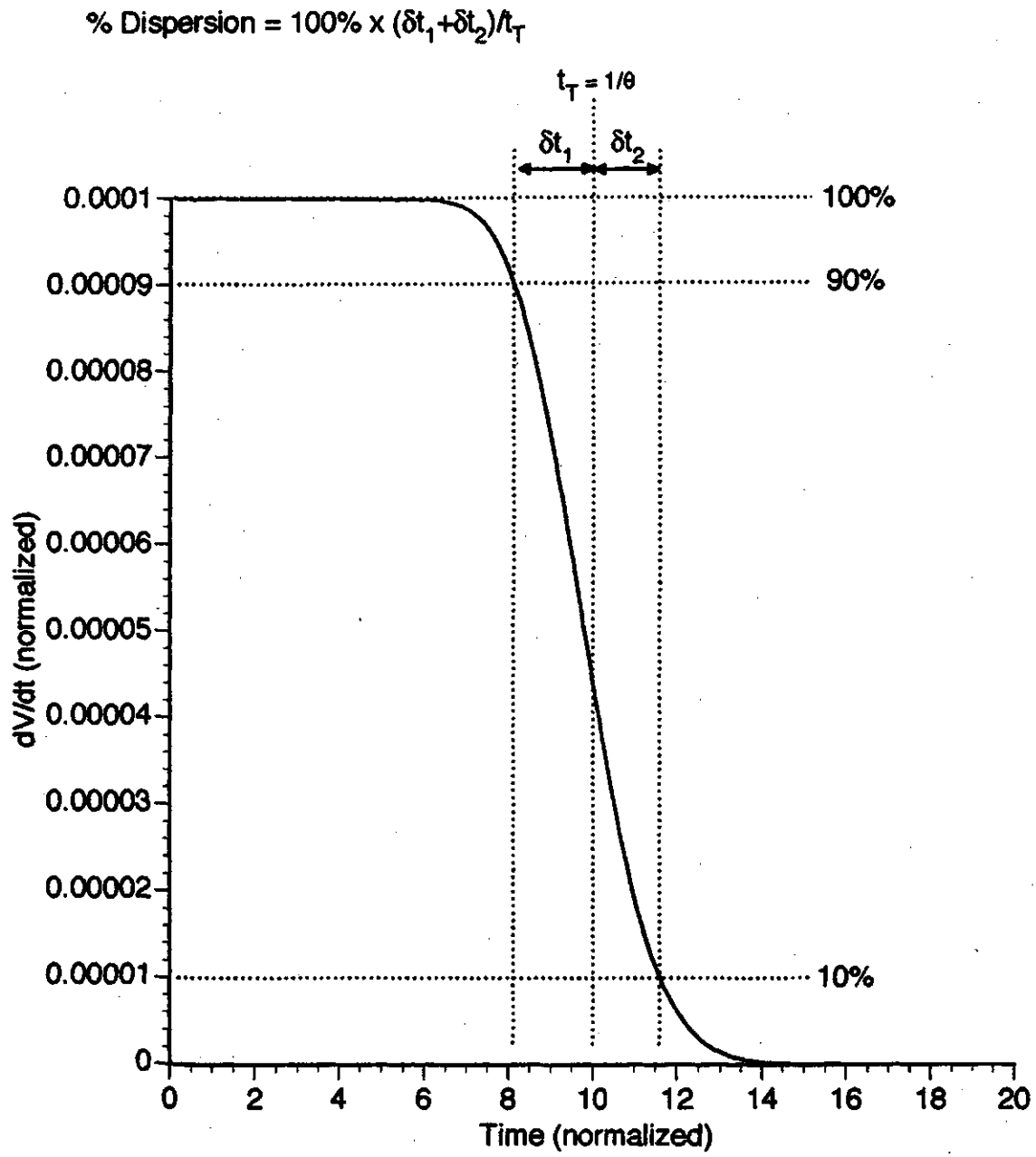

Figure 5.14. Method used to measure the dispersion of dV/dt waveforms.

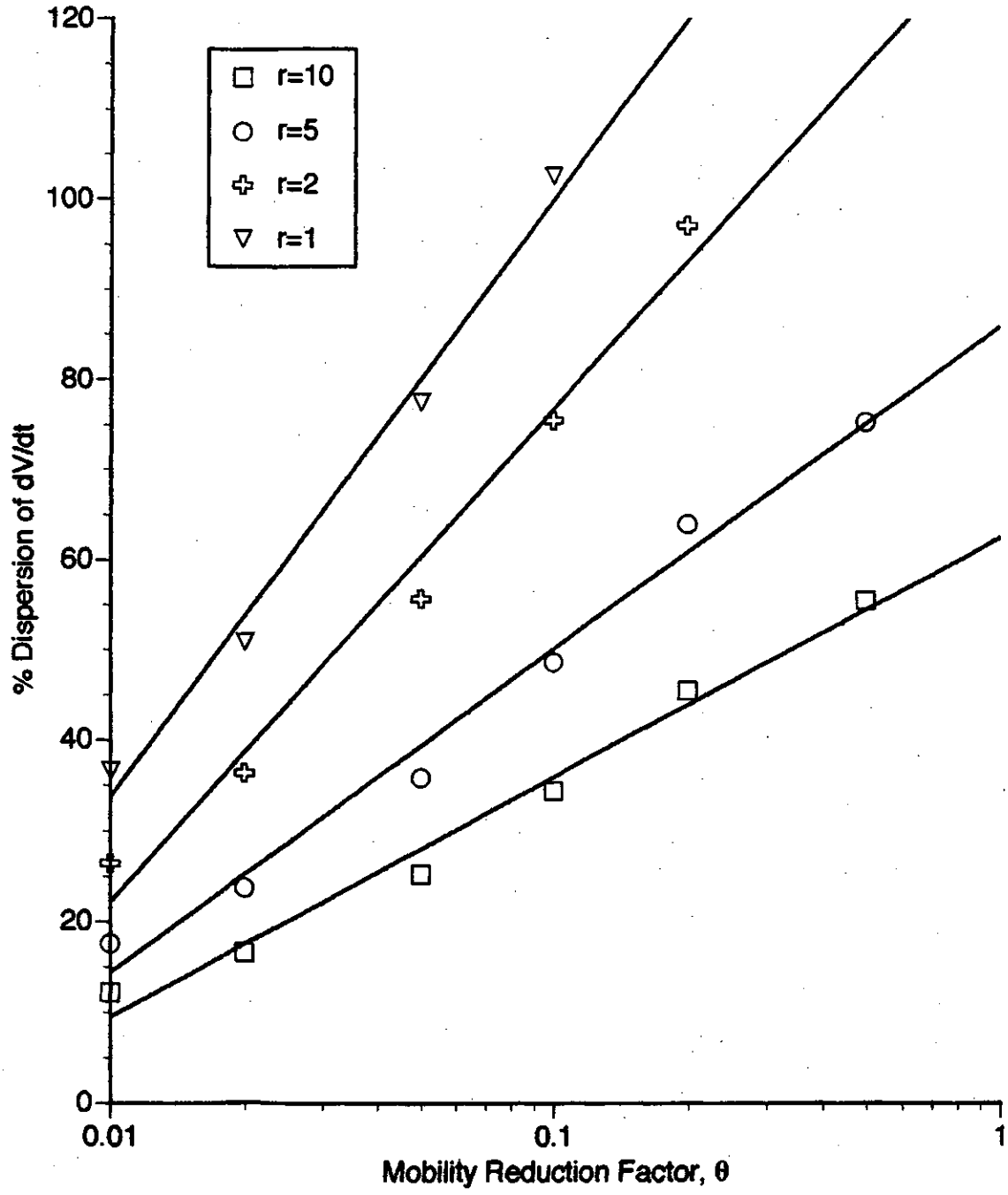

Figure 5.15. Percent dispersion of dV/dt versus mobility reduction factor under low injection conditions.

The dependence of the charge packet and dV/dt waveform dispersion on θ can be understood if one considers the origin of the mobility reduction concept. In chapter 2, the mobility reduction factor was derived to be

$$\theta = \frac{t_c}{t_c + t_r} \tag{5.14}$$

This ratio is essentially the average amount of time that the carrier is free to drift through the film. However, it is important to note that it is only the average. Sometimes, a carrier will drift for times longer than θ, other times, for times shorter than theta. We can hypothesize that the rate of packet dispersion with time is proportional to the mobility reduction factor, i.e.

$$\frac{d(\text{packet width})}{dt} \propto \theta \tag{5.15}$$

It has also been established that the rate of packet movement is also proportional to θ, i.e.

$$\frac{dx_{peak}}{dt} \propto \theta \tag{5.16}$$

Taking the ratio of Equations (5.15) and (5.16) suggests that the rate of packet dispersion with respect to peak movement is invariant with θ, i.e.

$$\frac{d(\text{packet width})}{dx_{peak}} \text{ is independent of } \theta \tag{5.17}$$

This prediction can be tested by measuring how the width of the packet changes as it passes through the film. The full-width half-maxima (FWHM) is a convenient measure of packet width. In order to test Equation (5.17), the FWHM of the packet can be measured at various points throughout the discharge. The computer program calculates the FWHM of the packet when the packet peak is as x=0.1, 0.2, 0.3, 0.4, etc. In order to

determine the increase in the packet width, the FWHM at each point is compared to the FWHM when the packet was 0.1 units closer to the surface. These results are shown in Figure 5.16. Upon viewing this figure, it appears that Equation (5.17) is indeed correct. The increase in FWHM with distance does not depend on the value of θ chosen. Interestingly enough, it does not appear to depend on the magnitude of the trapping parameters either. The results obtained with r=10 are very similar to results obtained with r=2. From Figure 5.16, we can conclude that the rate of packet spreading with distance does not depend on ω or r.

If the rate of spreading with distance is constant, why are different packet widths observed when different values of ω and r are chosen? For instance, if one compares Figure 5.5 and 5.10, one notes that the packet is much wider in the ω=99, r=1 case than in the ω=990, r=10 case, although the rate of spreading with distance is the same in both cases. This discrepancy can be explained by examining what occurs during the thermalization process that occurs at the beginning of the discharge. This process causes the charge packet to be wider if ω and r are smaller. Thermalization will be discussed in detail later in this chapter.

Another method can be used to measure dispersion. If the second derivative of the surface voltage, i.e. d^2V/dt^2 is plotted, one finds that there is a peak near the transit time predicted by $1/\theta$, as shown in Figure 5.17. The shape of this curve is reminiscent of a Gaussian function. The FWHM of this curve can be used as method of measuring dispersion. In fact, in work performed by Schmidlin [14,15], it has been shown that the spread in arrival times in TOF experiments can be represented by a normal distribution with a variance of

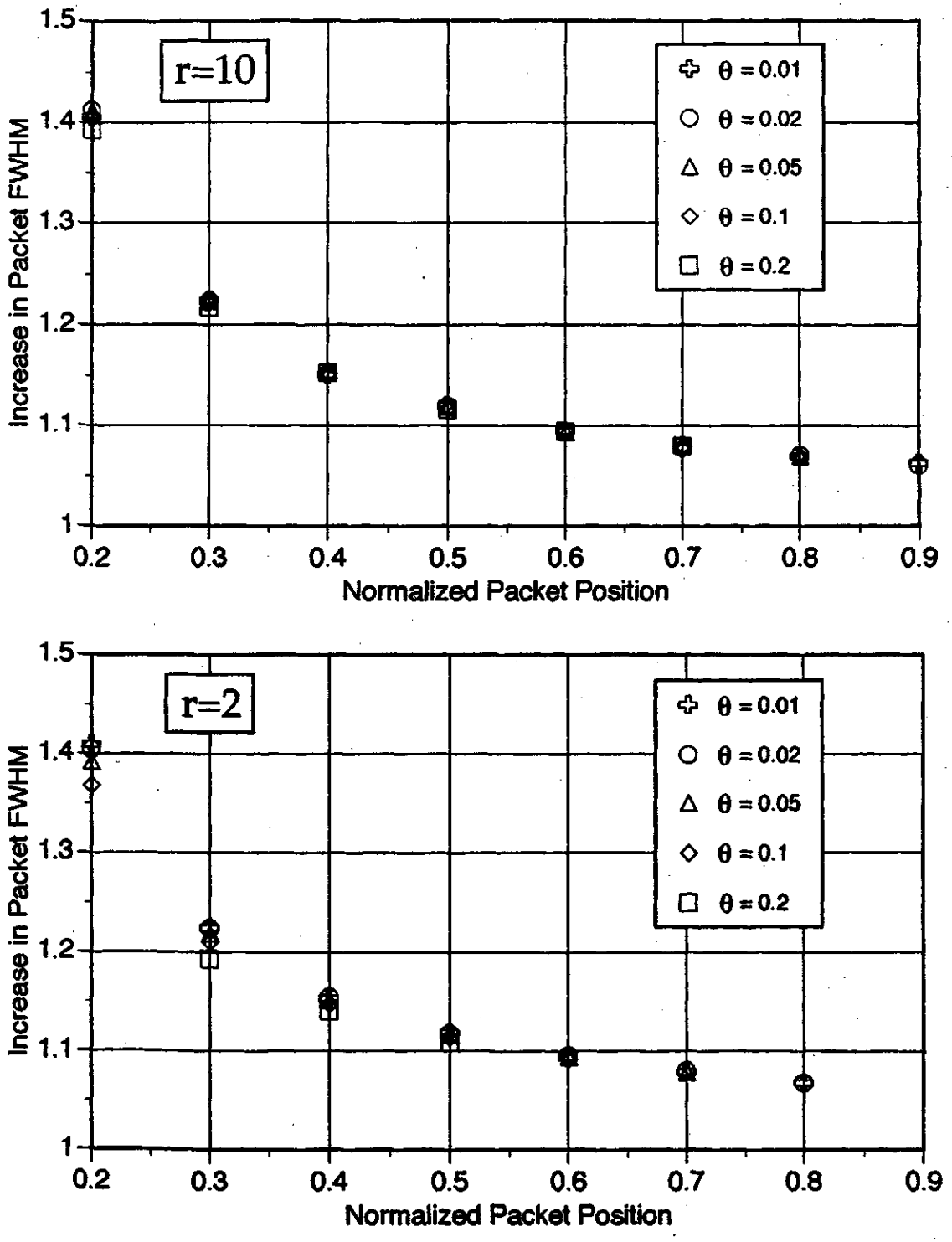

Figure 5.16. Increase in the untrapped charge packet FWHM as a function of packet position for various values of the mobility reduction factor and release rate, r. The increase in FWHM is taken with respect to the FWHM when the packet was 0.1 units closer to the surface.

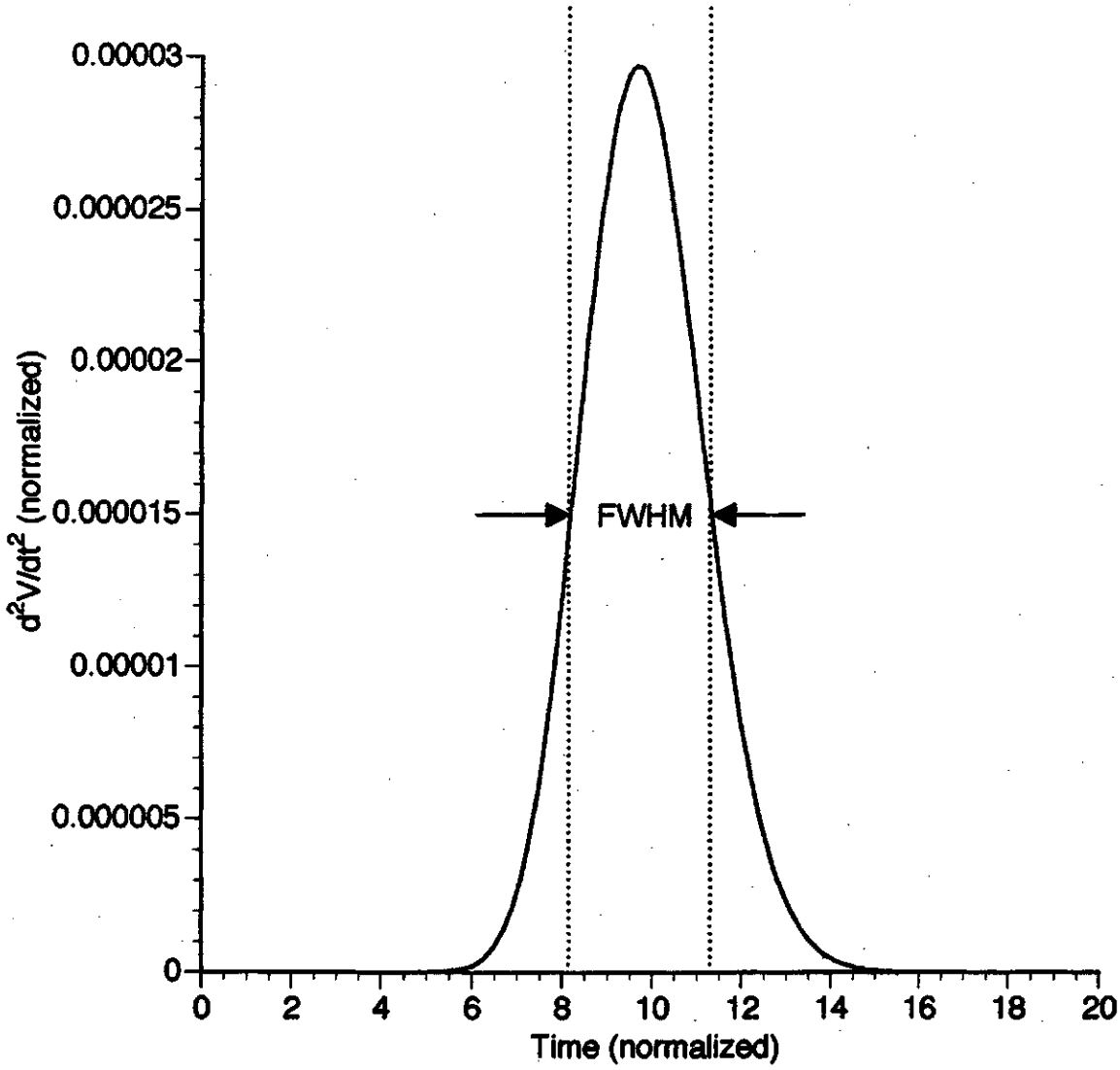

Figure 5.17. FWHM method of measuring dispersion.

$$(\Delta t')^2 = \frac{2(\tau_r')^2 L}{\tau_c' \mu_0 E} \tag{5.18}$$

where $\Delta t'^2$ = unnormalized variance of the arrival time distribution

τ_r' = unnormalized release lifetime

τ_c' = unnormalized capture lifetime

μ_0 = microscopic mobility

L = sample thickness

E = electric field

If the low injection is assumed, the electric field can be assumed to be constant at $E=V_0/L$. Equation (5.18) can be cast in terms of normalized rate parameters by noting the definitions of ω and r:

$$\omega = t_0 / \tau_{c0}' \tag{5.19}$$

$$r = t_0 / \tau_r' \tag{5.20}$$

where $t_0 = L^2 / \mu V_0$ = microscopic transit time

Note that if trap saturation is ignored (i.e. c=0), $\tau_{c0}'=\tau_c'$. The normalized variance $\Delta t^2 = (\Delta t')^2 / t_0^2$ can be obtained by substituting the expressions for E, ω, r, into Equation (5.18):

$$(t_0 \Delta t)^2 = \frac{2(t_0/r)^2 L}{(t_0/\omega)\mu_0 (V/L)}$$
$$\Delta t^2 = \frac{2\omega}{r^2} \tag{5.21}$$

The FWHM of a Gaussian function is related to its variance σ^2 by the relation

$$\text{FWHM} = 2\sqrt{2\ln 2 \sigma^2} \tag{5.22}$$

Using the equation for the variance gives the expected FWHM of d^2V/dt^2:

$$\text{FWHM in } d^2V/dt^2 = 2\sqrt{2\ln 2\left(2\omega/r^2\right)} = \frac{4\sqrt{\omega \ln 2}}{r} \qquad (5.23)$$

The FWHM results obtained from simulation results and the values predicted by equation (5.23) for several values of ω and r are tabulated in Table 5.4

Table 5.4. Comparison of simulated and theoretical d^2V/dt^2 FWHM.

ω	r	FWHM obtained from simulations	$\frac{4\sqrt{\omega \ln 2}}{r}$	% diff
40	10	2.08	2.106	1.2
90	10	3.16	3.159	0.03
190	10	4.63	4.59	0.9
490	10	7.60	7.37	3.1
990	10	11.15	10.47	6.5
20	5	2.90	2.98	2.7
45	5	4.45	4.47	0.45
95	5	6.58	6.49	1.4
245	5	10.9	10.43	4.5
495	5	16.15	14.8	9.1
38	2	10.16	10.26	1.0
98	2	16.68	16.48	1.2
198	2	24.2	23.43	3.3
49	1	23.2	23.31	0.47
99	1	33.55	33.13	1.3

These results are generally within good agreement. Results obtained with higher values of ω (i.e. ω=990,r=10 and ω=495 r=10) have errors that are significantly higher. This is likely due to the finite width of the initial injected charge packet, which is relatively undistorted during the thermalization process for large values of ω. This effect will discussed later when thermalization is examined.

5.4 High Injection

In the previous section, it was shown how the shape of the charge densities and the dV/dt waveform depended on the trapping constants ω and r. In this section it will be shown that the amount of injection plays an extremely important role in determining these properties as well. Also, since the injection is so high, the effects of trap saturation also become significant. Non-zero values of the trap saturation constant, c, will be used to incorporate this effect. The parameters used in examining the characteristics of high injection discharges are listed Table 5.5. In order to investigate the effect of injection, three different injection levels are used: 10%, 50%, and 99%. Different values of ω and r are used to provide different trapping strengths and different values for the mobility reduction factor. The results obtained with the trap saturation coefficient c set to zero are shown in Figures 5.18 through 5.23.

Table 5.5. Trapping and release parameters used in high injection simulations

% Injection $(1-\varphi) * 100\%$	Mobility Reduction Factor, θ	Trap Capture Rate, ω	Trap Release Rate, r	Trap Saturation Coeff., c
10	0.01	990	10	0
	0.1	90	10	0
50	0.01	990	10	0
	0.1	90	10	0
99	0.01	990	10	0
	0.1	90	10	0
		90	10	1
		90	10	5
		90	10	10

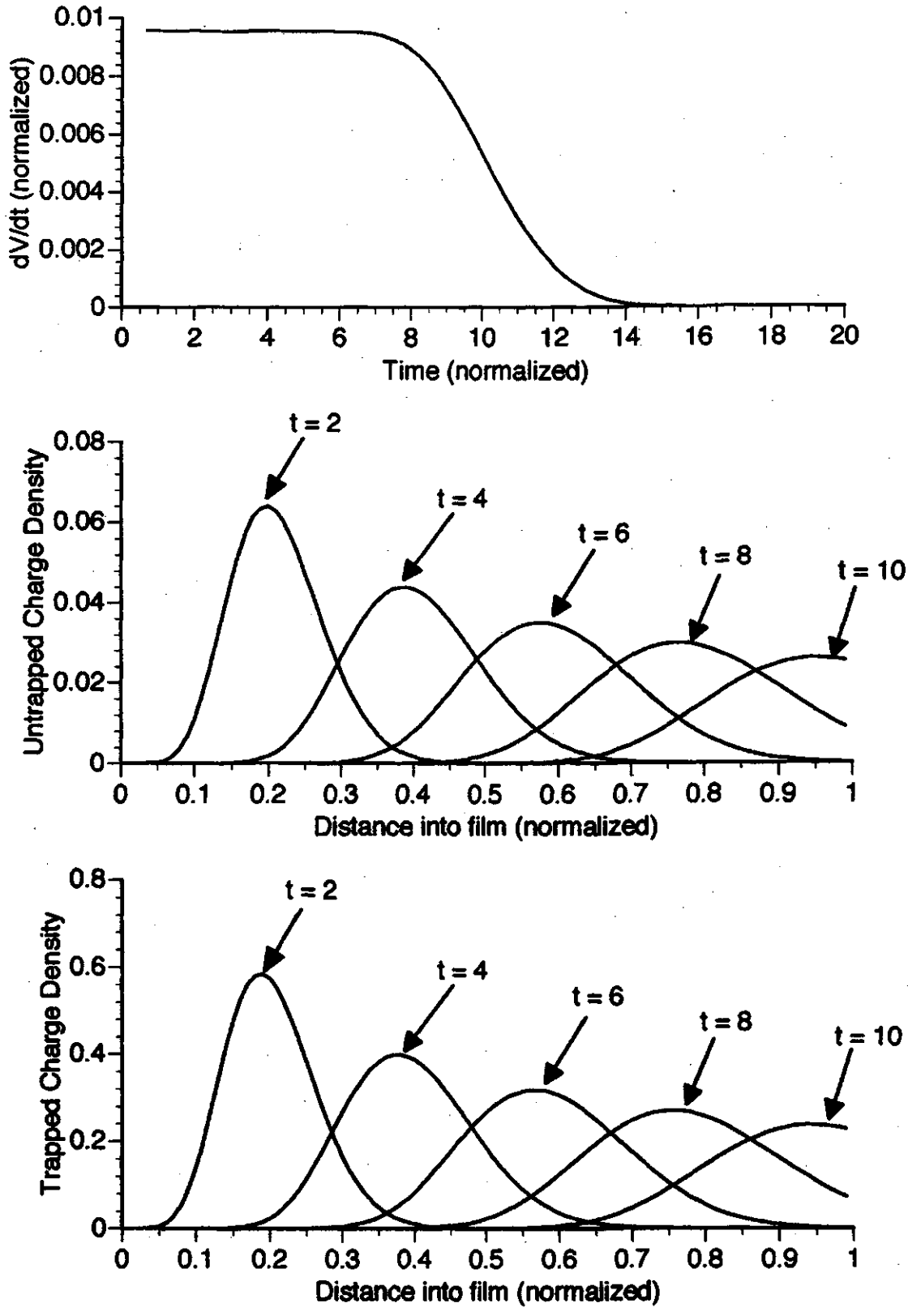

Figure 5.18. Simulation results obtained under 10% injection with $\omega = 90$, $r = 10$, $c=0$, and $\theta = 0.1$.

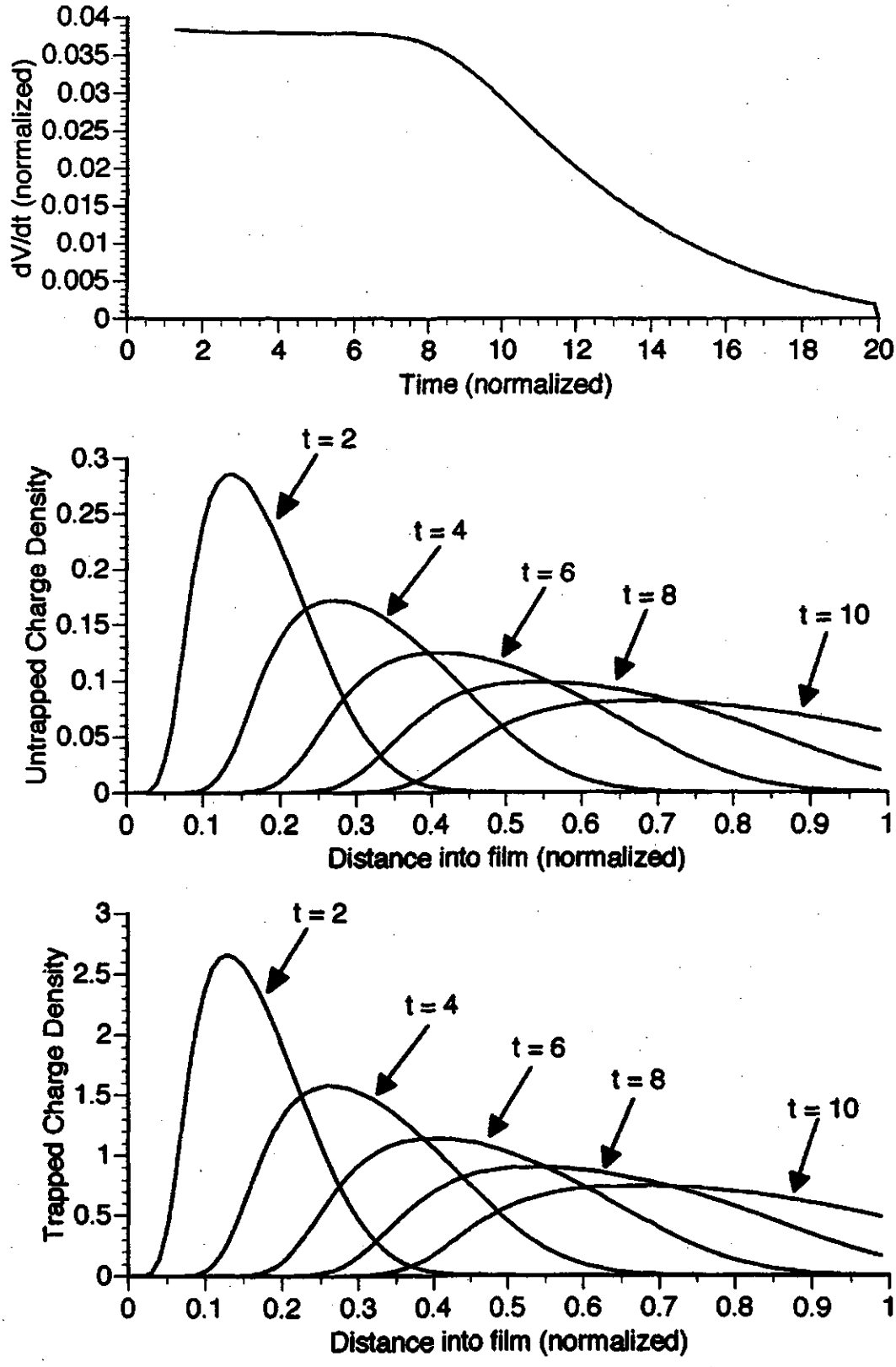

Figure 5.19. Simulation results obtained under 50% injection with $\omega = 90$, $r = 10$, $c=0$, and $\theta = 0.1$.

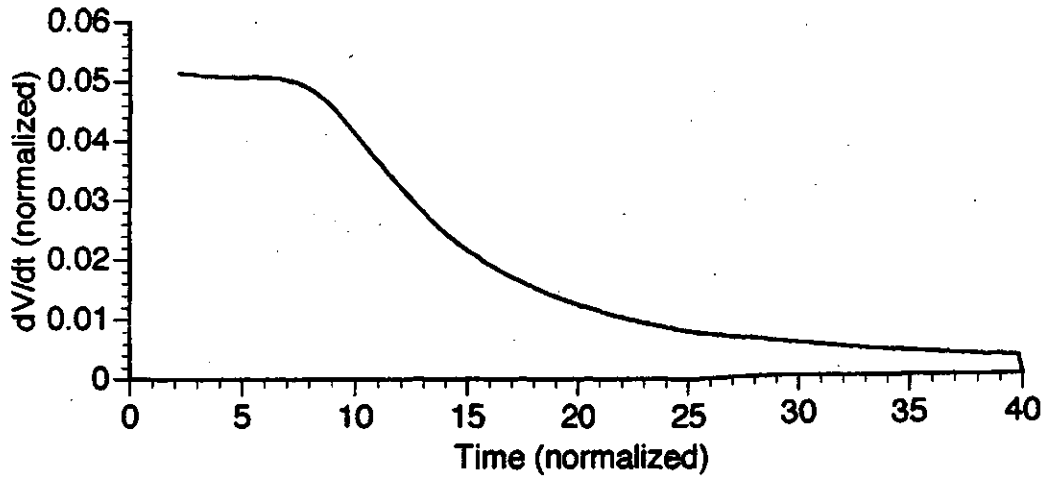

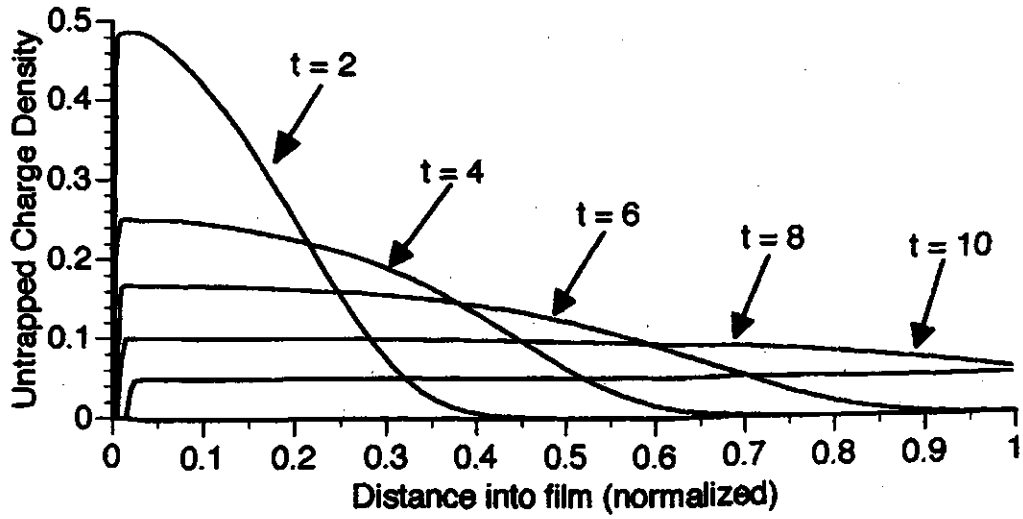

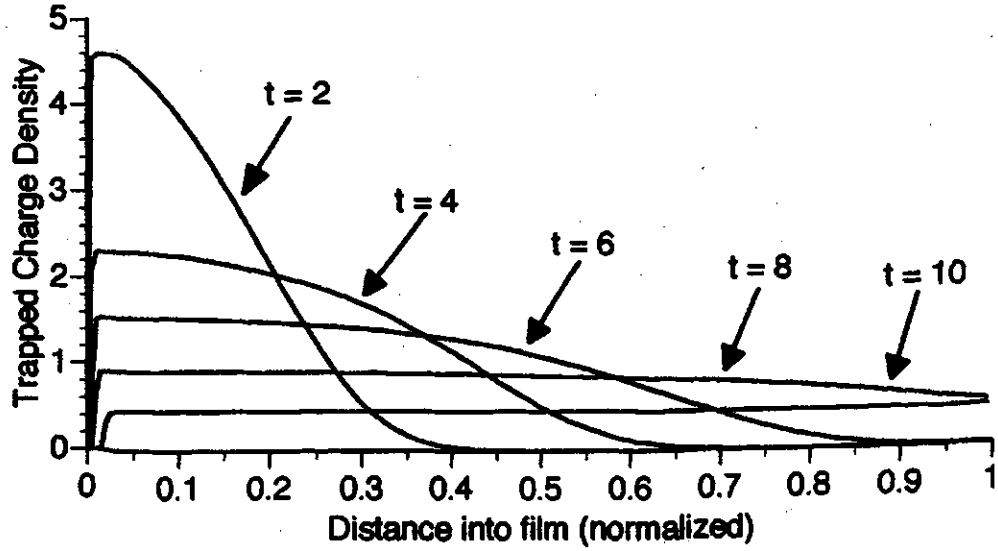

Figure 5.20. Simulation results obtained under 99% injection with $\omega = 90$, $r = 10$, $c=0$, and $\theta = 0.1$.

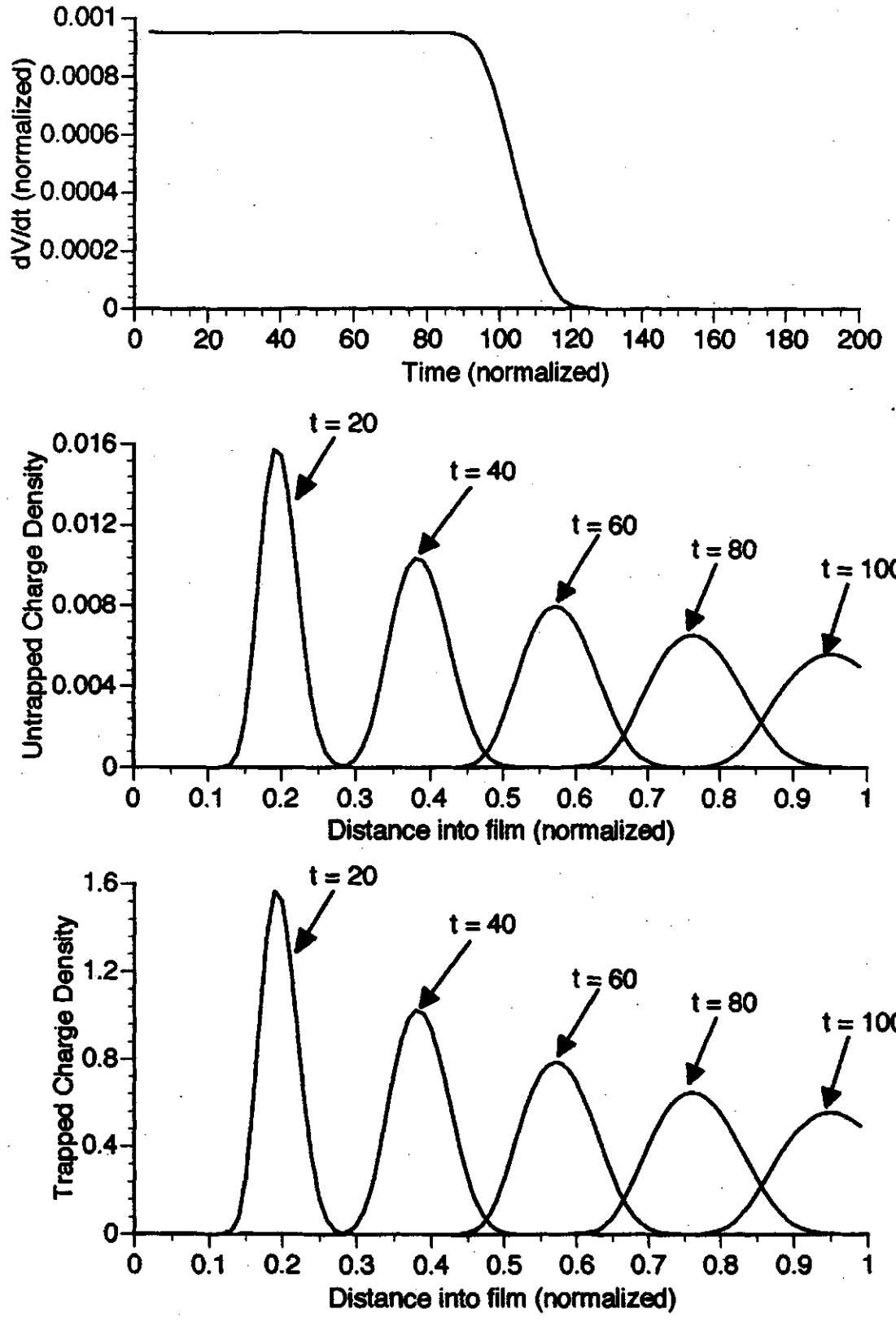

Figure 5.21. Simulation results obtained under 10% injection with $\omega = 990$, $r = 10$, $c=0$, and $\theta = 0.01$.

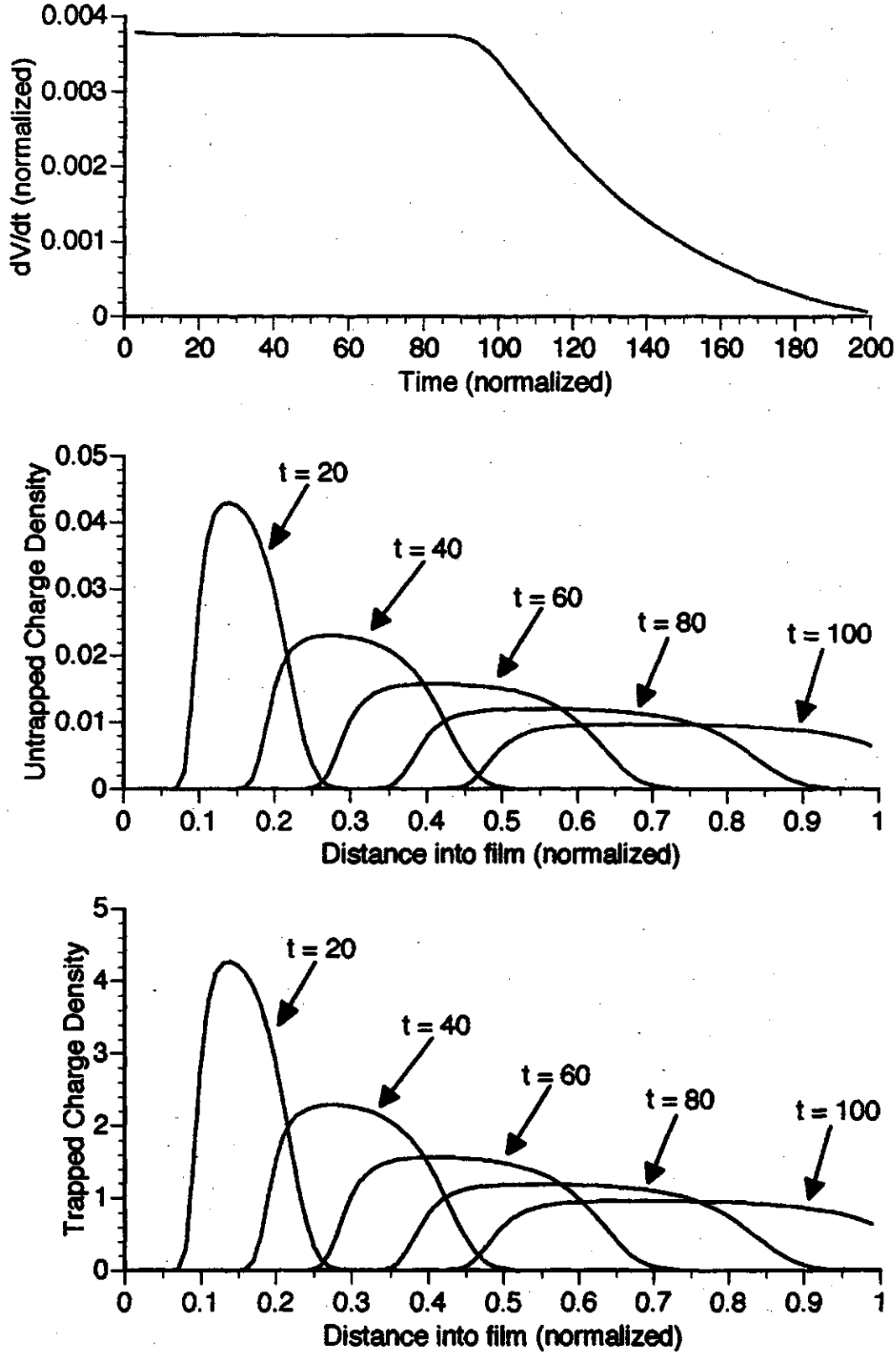

Figure 5.22. Simulation results obtained under 50% injection with $\omega = 990$, $r = 10$, $c=0$, and $\theta = 0.01$.

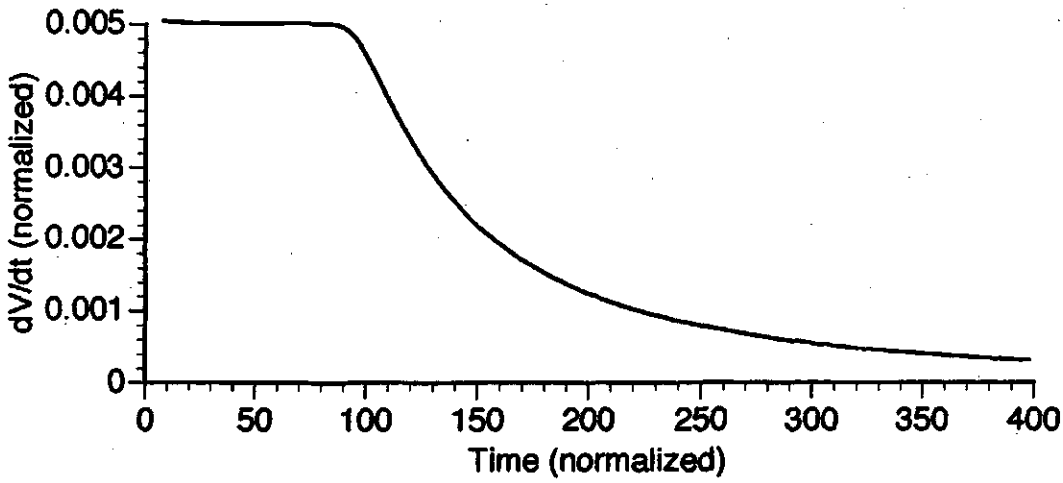

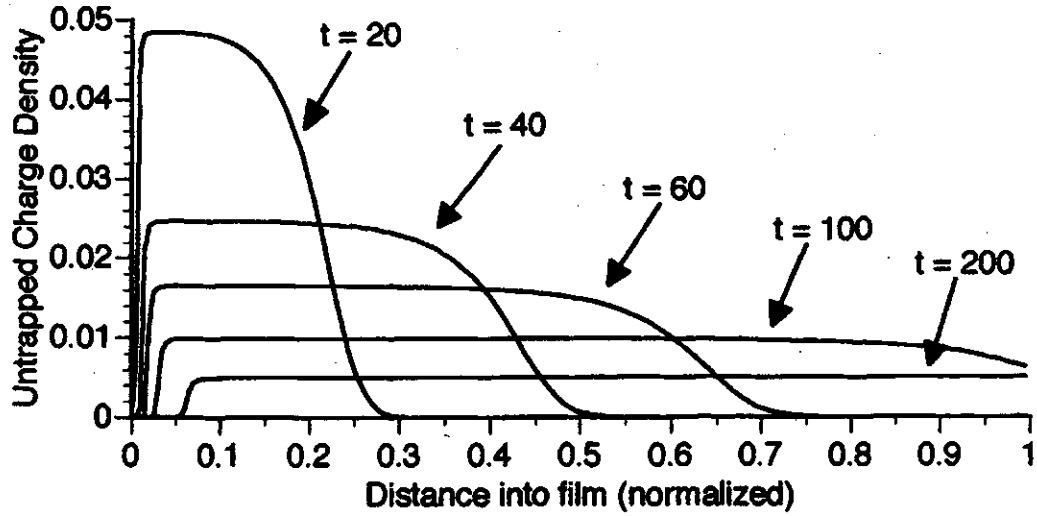

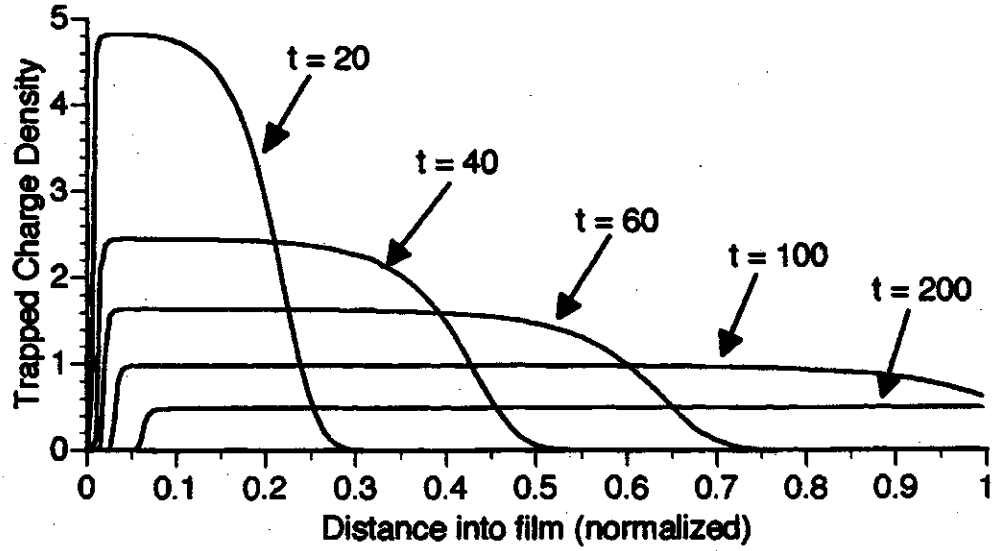

Figure 5.23. Simulation results obtained under 99% injection with $\omega = 990$, $r = 10$, $c=0$, and $\theta = 0.01$.

Figures 5.18 through 5.20 show the results obtained with ω=90, r=10, and c=0 with injection strengths of 10%, 50% and 99%, respectively. The 10% injection case shown in Figure 5.18 is reminiscent of the low injection results presented in Figure 5.8. The shape of the charge packet is still approximately Gaussian. This is because the motion of the charge packet is primarily due to the charge left on the surface, which is equal to 90% of the total charge. When the injection level is increased to 50%, as shown in Figure 5.19, the charge packets start to exhibit a fair amount of asymmetry. This phenomenon can be explained by examining the expression for the electric field given by Equation (5.5). From this equation, we can conclude that if the injection is significant, the charge packet is moving not only due to the influence of the field created by the surface charge, but also due to the field created by the packet itself. Equation (5.5) also implies that the field will increase significantly as the substrate is approached. As a result, charge located closer to the substrate (i.e. closer to x=1) moves faster than charge closer to the surface, creating the asymmetry in the charge packet. This effect is taken to the extreme in the 99% injection case depicted in Figure 5.20. The leading end of the packet moves much faster than the trailing end located near the surface. In fact, the field is so low near the surface that the charge located there does not move very far during the course of the discharge.

Figures 5.21 through 5.23 contain the results obtained for the same set of injection strengths but with a different set of trapping parameters, ω=990, r=10, c=0. The same basic features are present in these results. The results obtained with 10% shown in Figure 5.21 are similar to those obtained with low injection depicted in Figure 5.5. As the injection is increased, as shown in Figures 5.22 and Figure 5.23, the charge packets become more spread out.

A comparison of Figures 5.18 through 5.20 and Figures 5.21 through 5.23, respectively, illustrates that the spread in the charge packets increases with decreasing ω. This result is consistent with the low injection results presented in the previous section. This dependence is much less pronounced in the case of extremely high injection shown in Figures 5.20 and 5.23. Under high injection conditions, the spread in the charge packet is primarily due to the amount of injection, not the trapping parameters.

The behaviour of the charge packets under high injection conditions have a profound effect on the dV/dt waveform. An examination of the dV/dt graphs shown in Figures 5.18 through 5.23 allows three conclusions to be made: (1) The pre-transit time value of dV/dt is no longer given by $\theta(1-\varphi)$, (2) dV/dt starts dropping near the transit time predicted by $1/\theta$, and (3) the length of the discharge "tail" following this transit time increases significantly as the injection increases. These conclusions will be discussed in turn.

The pre-transit time value of dV/dt for the results shown in Figure 5.18 through 5.23 are listed in Table 5.6.

Table 5.6. Comparison of $\theta(1-\varphi)$ and the pre-transit time dV/dt value for various injection levels.

Figure	ω	r	θ	φ	$\theta(1-\varphi)$	Pre-Transit Time dV/dt value	% diff
5.18	90	10	0.1	0.9	0.01	0.00955	4.5
5.19	90	10	0.1	0.5	0.05	0.03850	23.0
5.20	90	10	0.1	0.01	0.099	0.05219	47.3
5.21	990	10	0.01	0.9	0.001	0.000957	4.3
5.22	990	10	0.01	0.5	0.005	0.003868	22.6
5.23	990	10	0.01	0.01	0.0099	0.005378	45.7

The expression for the pre-transit time value of dV/dt, $\theta(1-\varphi)$, originated from Equation (5.10), which is repeated here:

$$\frac{dV(t)}{dt} = \frac{d}{dt}\left(\int_0^1 E(x,t)dx\right) \cong (1-\varphi)v_p \qquad (5.10)$$

In section 5.3, it was shown that under low injection conditions, the packet moves with a normalized velocity of θ, leading to the expression $\theta(1-\varphi)$. However, the packet only moves with a velocity of θ if the normalized field seen by the entire packet is approximately equal to unity. This condition is only strictly met under low injection conditions. As the injection increases, the pre-transit time value of dV/dt drops because the trailing end of the packet sees a reduced field, and therefore moves with a reduced velocity. This explains why the 10% injection results shown in Table 5.6 are in better agreement with the predicted value of $\theta(1-\varphi)$ than the results obtained with 50% and 99% injection.

Under high injection conditions, the dV/dt waveform starts dropping near the trap controlled transit time predicted by $1/\theta$. This can be explained by observing that the charge at the very leading edge of the packet sees a field that is close to unity, regardless of the injection level. This is because the charge on the leading edge sees the field due to the charge remaining on the surface and the majority of the charge packet. As a result, a small portion of the charge packet reaches the substrate at a time near the predicted transit time of $1/\theta$, causing dV/dt to start dropping.

An examination of Figures 5.18 through 5.23 illustrates that the length of the "tail" of dV/dt increases with increasing injection. This can be understood using an argument that is complementary to the one provided above. The charge at the trailing end of the packet sees only the field due to the charge remaining on the surface. This

causes the trailing end of the packet to move more slowly than the leading edge. This causes the duration of the discharge to draw out, creating a longer "tail" in dV/dt. It also explains why the packet becomes more elongated as the discharge progresses. This effect is most pronounced in the 99% injection cases shown in Figures 5.20 and 5.23, where packet eventually ends up spanning more than 90% of the sample.

This increase in tail length with injection can be expressed quantitatively using the dispersion method described in Figure 5.14. The results are shown in Figure 5.24. Dispersion results obtained from the corresponding low injection results are also shown to allow a comparison. The dispersion at 10% injection is slightly greater than the dispersion obtained under low injection (i.e. 0.1% injection) conditions. As the injection increases from 50% to 99%, the percent dispersion increases dramatically. Note that the dispersion increases with decreasing ω, which is in line with previous observations. The effect of changing ω is nearly constant (i.e. 15 - 20 %), regardless of the amount of injection. Obviously, the amount of injection is the main factor affecting the amount of dispersion under high injection conditions. The effects of trapping, as far as percent dispersion is concerned, become less significant under high injection.

All of the simulation results presented thus far have ignored the effects of trap saturation. This is equivalent to assuming that the trap density N_t in the unnormalized trapping rate equation,

$$\frac{\partial p_t'(x',t')}{\partial t'} = p'(x',t')C_t\left[N_t - p_t'(x',t')\right] - \frac{p_t'(x',t')}{\tau_r'} \tag{5.24}$$

is much larger than the unnormalized trapped charge density, $p_t'(x',t')$. Recall that this equation has its normalized form in Equation (3.29),

$$\frac{\partial p_t(x,t)}{\partial t} = \omega p(x,t) - r p_t(x,t) - c p(x,t) p_t(x,t), \tag{5.25}$$

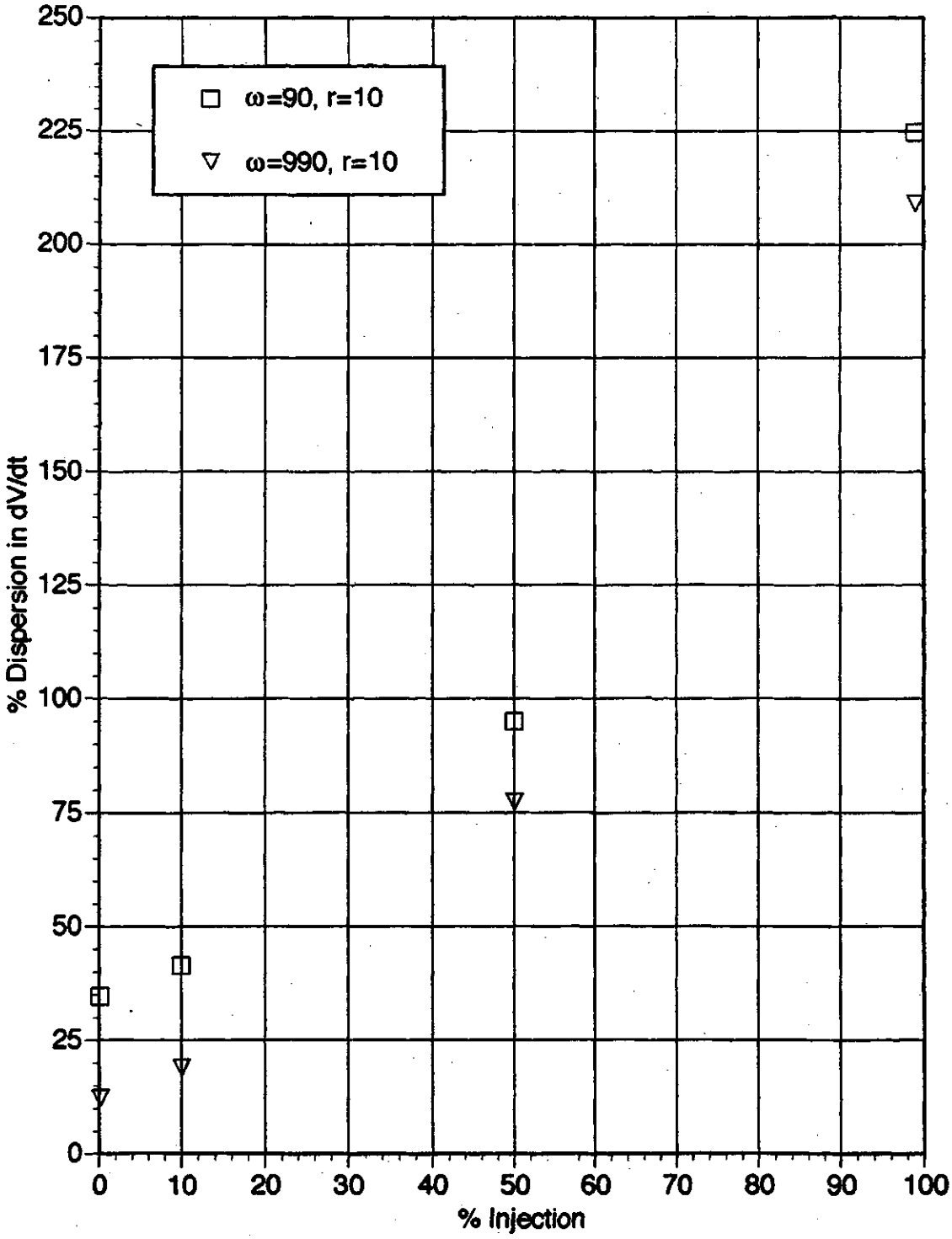

Figure 5.24. Percent disperion in dV/dt as a function of injection for various values of ω and r. The trap saturation constant c is set to zero.

where c is the trap saturation coefficient. If c is set equal to zero, the last term of Equation (3.29) vanishes and trap saturation is neglected.

To observe the affects of trap saturation, simulations have been performed with the trap saturation coefficients of c = 1,5, and 10. The results are shown in Figures 5.25 through 5.27. These figures can be compared to Figure 5.20, where trap saturation has been ignored. Note that as the trap saturation parameter c is increased, the peak concentration of the trapped and untrapped charge packets decreases. Also note that the top of the packet becomes flatter. These phenomena can be explained in terms of trap saturation. As c is increased, the number of available traps at a given position decreases. This limits the magnitude of the trapped charge density at a given position. When all of the traps at a given position have been filled, any remaining untrapped charge can move forward into a region where more traps are available. Trapping will occur at that position until the traps are filled. Then the remaining amount of untrapped charge will move forward again, etc. This process will continue until equilibrium can be reached between the trapped and untrapped charge packets, as governed by the trapping rate equation. As a result, the charge packet becomes more spread out and has a smaller and smaller peak magnitude as the trap saturation parameter is increased.

This behaviour is reflected in the pre-transit time behaviour of the dV/dt waveform. In Figure 5.20, where c=0, dV/dt is essentially constant before t=7. As c is increased, as shown in Figures 5.25 through 5.27, a significant amount of decay appears in dV/dt before the transit time. This is because it takes more time for the untrapped charge to reach equilibrium with the trapped charge when significant trap saturation is present. Note that the post-transit time behaviour of dV/dt is not significantly affected by trap saturation. This is because the majority of the packet spreading is caused by the amount of injection, as was discussed earlier.

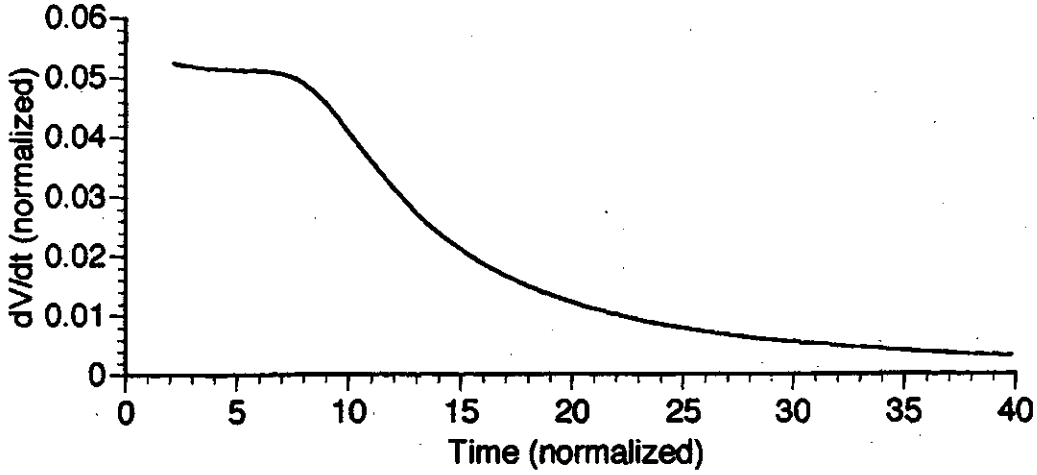

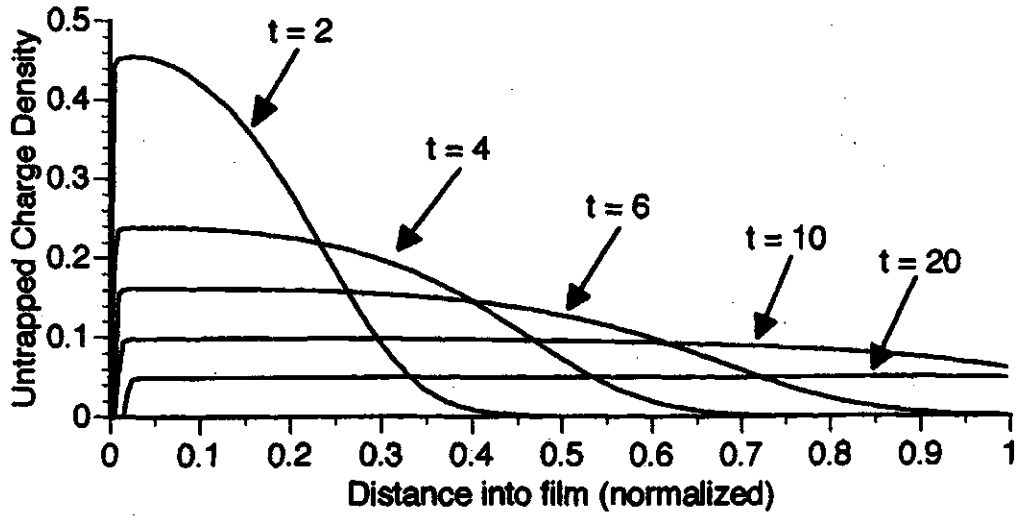

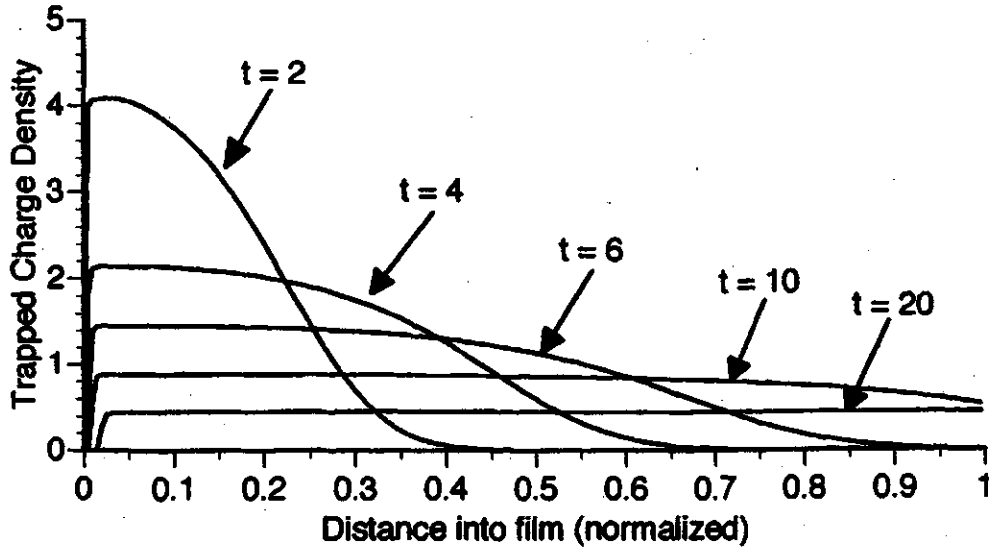

Figure 5.25. Simulation results obtained under 99% injection with $\omega = 90$, $r = 10$, $c=1$, and $\theta = 0.1$.

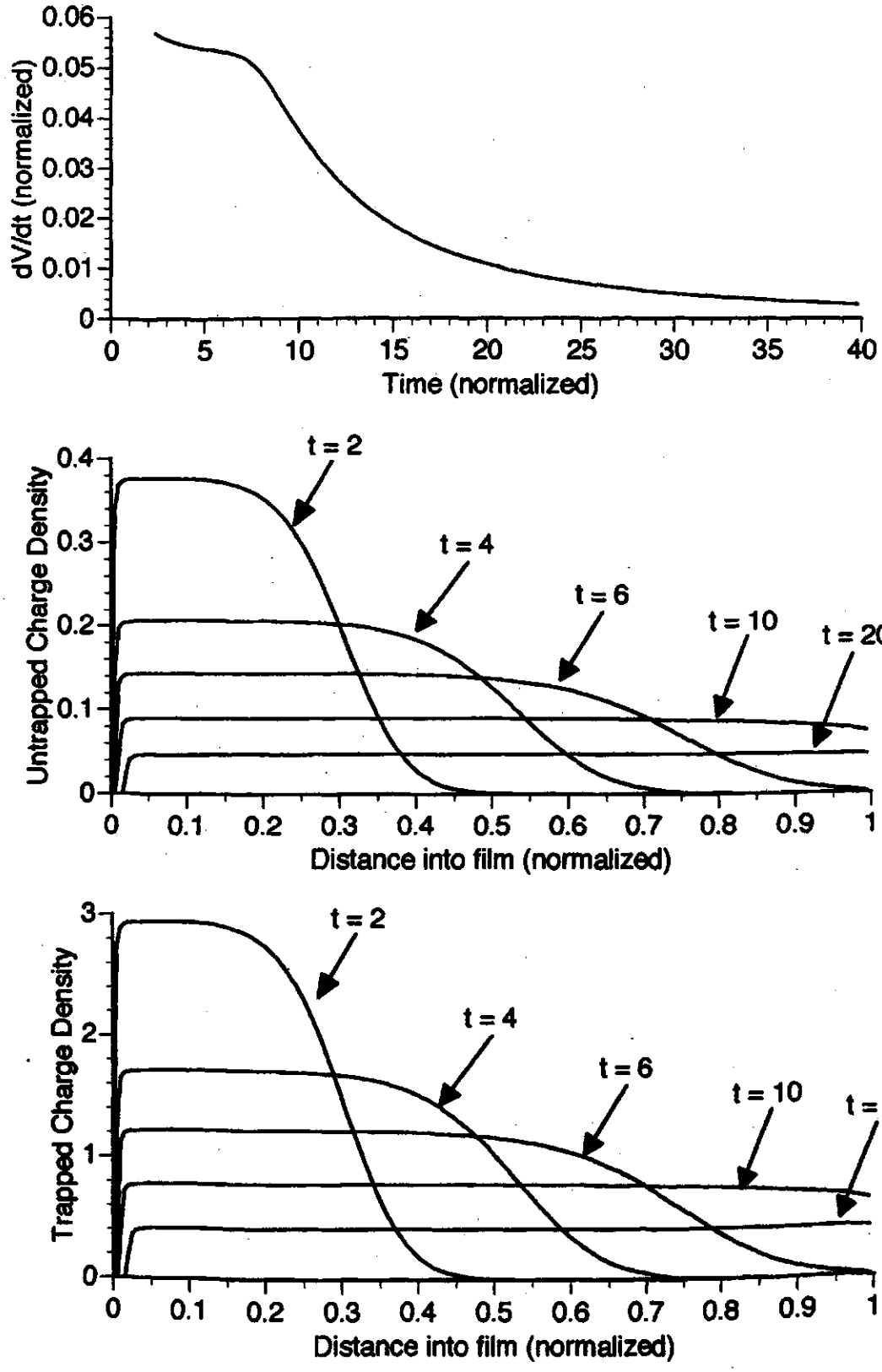

Figure 5.26. Simulation results obtained under 99% injection with $\omega = 90$, $r = 10$, $c=5$, and $\theta = 0.1$.

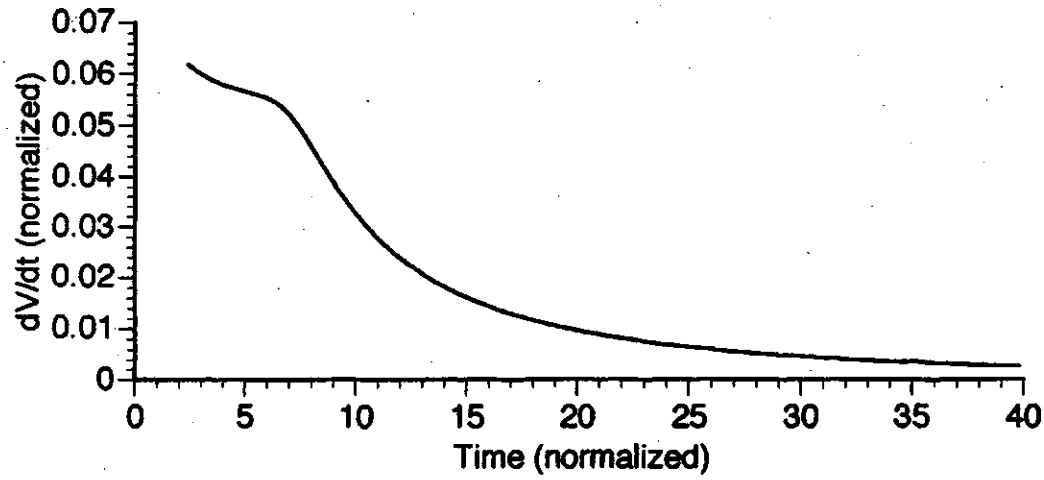

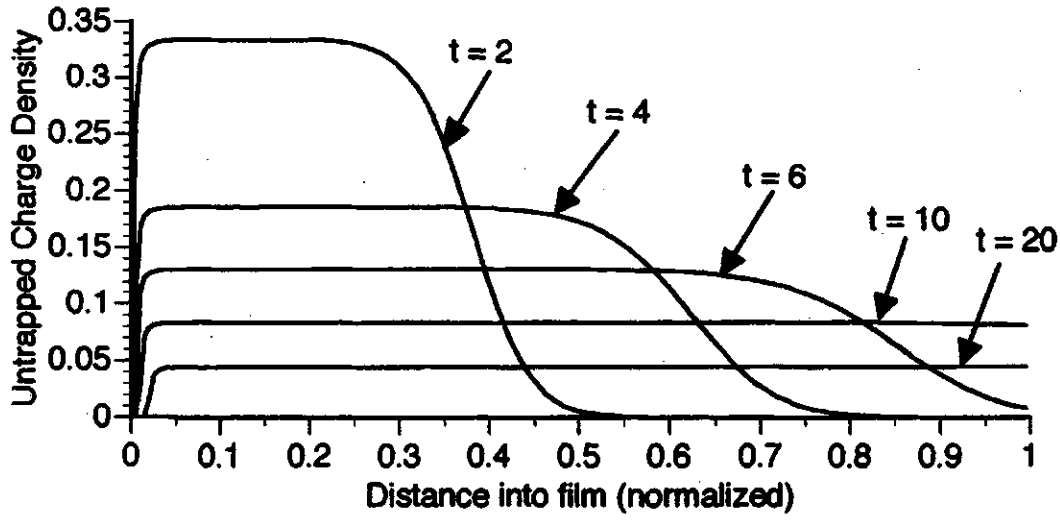

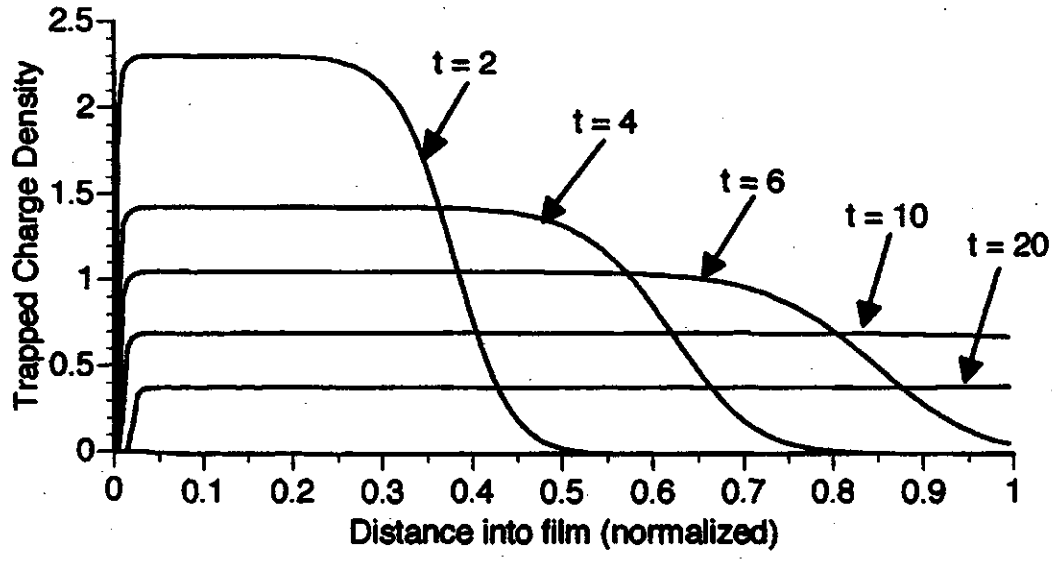

Figure 5.27. Simulation results obtained under 99% injection with $\omega = 90$, $r = 10$, $c=10$, and $\theta = 0.1$.

An investigation of the thermalization process under high injection conditions would provide a more quantitative explanation for these phenomena. However, the study of thermalization under high injection conditions is beyond the scope of this work. Thermalization results obtained under low injection conditions are presented in the next section.

5.5 Thermalization

Recall that the initial conditions discussed in Section 3.4.2 stipulated that the initial trapped charge density $p_t(x,0)$ was equal to zero and that the initial untrapped charge density used in the simulations was given by a "wedge-shaped" distribution:

$$p(x,0) = \begin{cases} \dfrac{400(1-\varphi)x}{19\delta^2}, & 0 \le x < \dfrac{\delta}{20} \\ \dfrac{20(1-\varphi)}{19\delta}, & \dfrac{\delta}{20} \le x < \dfrac{19\delta}{20} \\ \dfrac{400(1-\varphi)(\delta-x)}{19\delta^2}, & \dfrac{19\delta}{20} \le x < \delta \\ 0, & x \ge \delta \end{cases} \tag{5.11}$$

Inspection of the normalized trapping rate equation,

$$\frac{\partial p_t(x,t)}{\partial t} = \omega p(x,t) - r p_t(x,t) - c p(x,t) p_t(x,t), \tag{5.14}$$

illustrates that this is definitely not an equilibrium condition. At the beginning of the discharge, the trapped charge density begins to increase until the left-hand side of Equation (5.14) approaches zero. At this point, thermal equilibrium between the extended states and the single trapping level has been achieved. The term "thermal" is used because trapping is a thermally governed process. The process of reaching this equilibrium condition is called thermalization.

A simplified analysis of this process can be obtained by removing variation with distance from Equation (5.14) and setting c=0. In this case, Equation (5.14) reduces to

$$\frac{dp_t(t)}{dt} = \omega p(t) - r p_t(t). \tag{5.15}$$

This is essentially the equation governing an extremely narrow charge packet that is not moving (i.e. variation with distance is not important). If we note that the total injected charge is always equal to 1- φ, we note that

$$p_t = (1-\varphi) - p \tag{5.16}$$

Substituting this into Equation (5.15) gives

$$\frac{dp}{dt} = r(1-\varphi) - (\omega + r)p \tag{5.17}$$

The solution to this equation is trivial, and is given by

$$p = (p_0 - p_f)e^{-(\omega+r)t} + p_f \tag{5.18}$$

where p_0 = untrapped charge initial value $= 1-\varphi$

p_f = untrapped charge final value $= (1-\varphi)\dfrac{r}{\omega + r}$

This analysis predicts that the untrapped charge will decrease exponentially with a rate constant equal to ω+r during the thermalization process.

The accuracy of this analysis can be evaluated by performing simulations with various values of ω and r. In these simulations, the amount of injected charge is fixed at 0.1%. The effect of modifying the width of the injection layer is also examined by modifying the parameter δ in Equation (5.13). In order to examine the thermalization process, the final time value t_{max} used in the simulations is set to be approximately equal to 20 time constants, i.e. $t_{max} \approx 20/(\omega+r)$. The parameters used in thermalization

simulations are listed in Table 5.7. The results of these simulations are shown in Figures 5.28 through 5.32.

Table 5.7. Parameters used in thermalization simulations.

Trap Capture Rate, ω	Trap Release Rate, r	Trap Saturation Coeff., c	Injection Depth, δ	Final Time, t_{max}
90	10	0	0.01	0.2
90	10	0	0.005	0.2
990	10	0	0.01	0.02
990	10	0	0.005	0.02
990	50	0	0.01	0.02

A few general comments can be made about these figures. First, consider the behaviour of dV/dt during thermalization. In each case, dV/dt starts at a value of $(1-\varphi)$ and decays to a value of $\theta(1-\varphi)$. Recall that the pre-transit time value for dV/dt is given by $(1-\varphi)v_p$, where v_p is the velocity of the packet. Initially, all of the charge is moving at a velocity governed by the microscopic mobility, because no trapping has taken place. This corresponds to a normalized velocity of $v_p = 1$, causing dV/dt to take on an initial value of $1-\varphi$. This value drops to the trap controlled value of $\theta(1-\varphi)$ once the thermalization process is complete and the packet velocity v_p has dropped to θ. This argument can be verified by observing the results obtained with ω=90 and r=10, which are shown in Figures 5.28 and 5.29. A visual inspection confirms that the peak of the packet is moving with a velocity that is approximately equal to unity.

An examination of Figures 5.28 and 5.29 reveals that the unthermalized portion of the packet leaves behind a thermalized portion as it moves. Note that it takes a finite time for the packet to thermalize. The longer it takes for the untrapped packet to thermalize, the farther the packet can travel while it thermalizes. As a result, the width of the packet after thermalization is roughly proportional to the duration of the

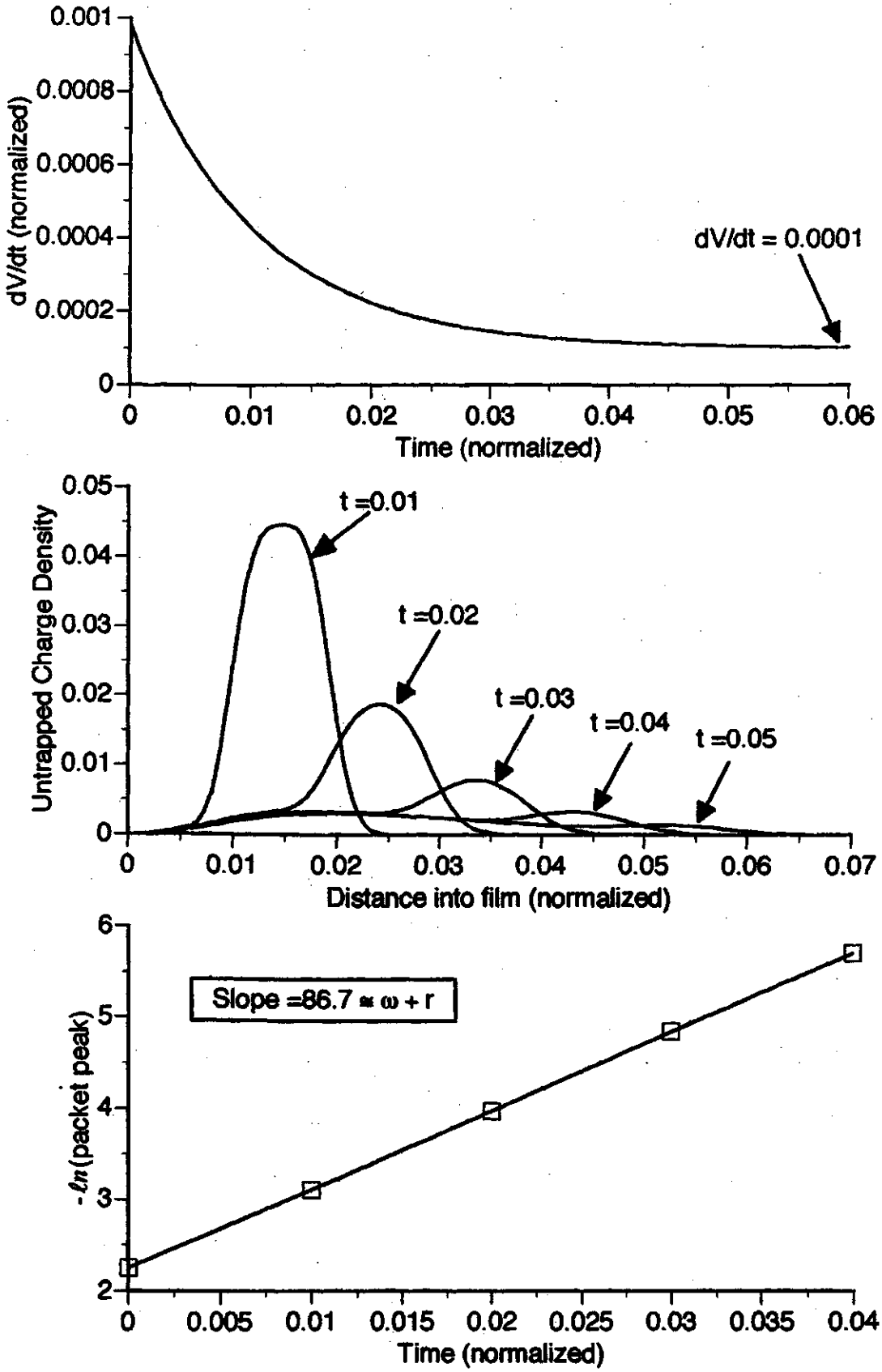

Figure 5.28. Thermalization process under low injection conditions with ω=90, r=10, and δ = 0.01.

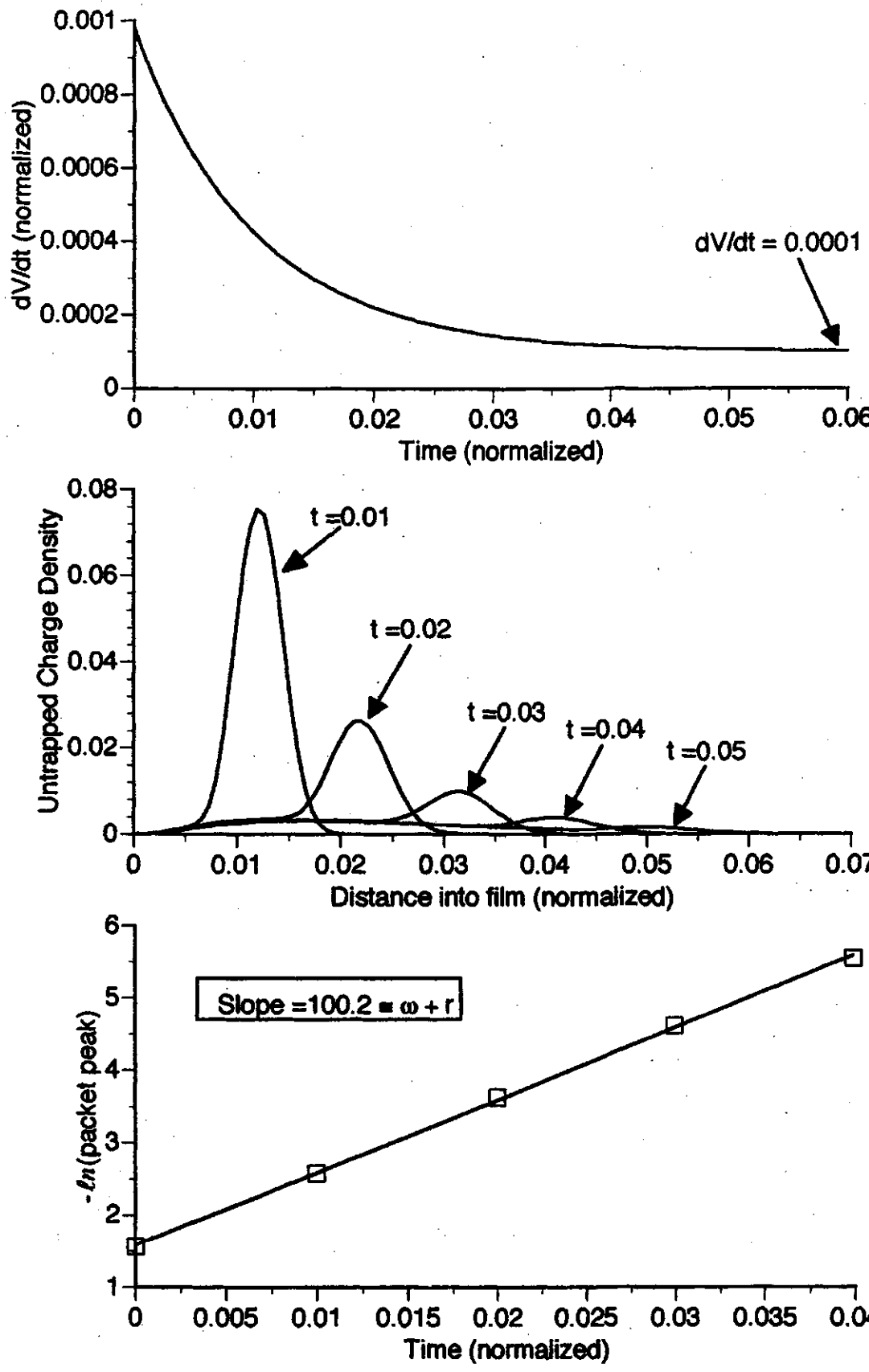

Figure 5.29. Thermalization process under low injection conditions with ω=90, r=10, and δ = 0.005.

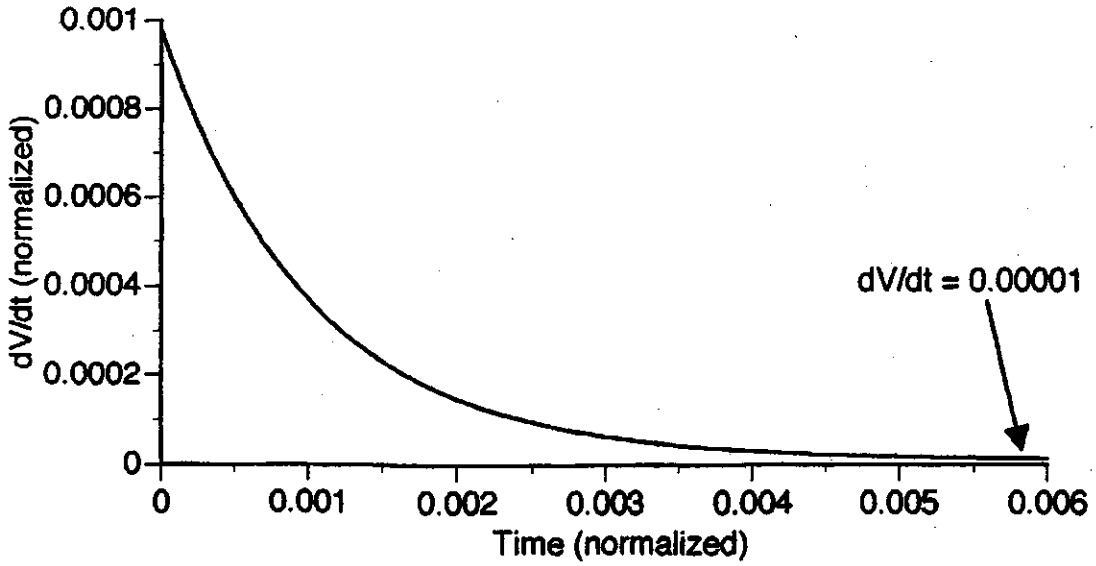

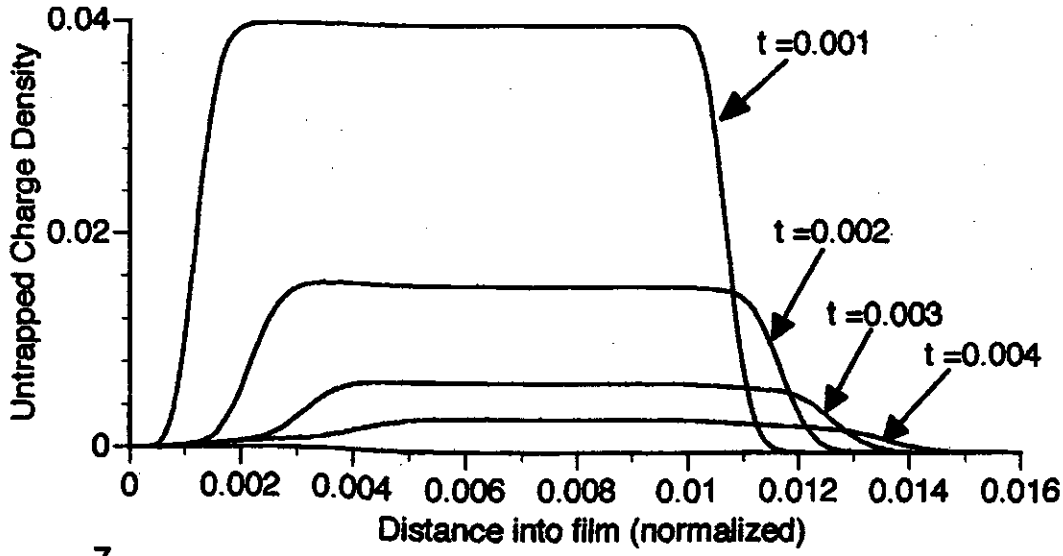

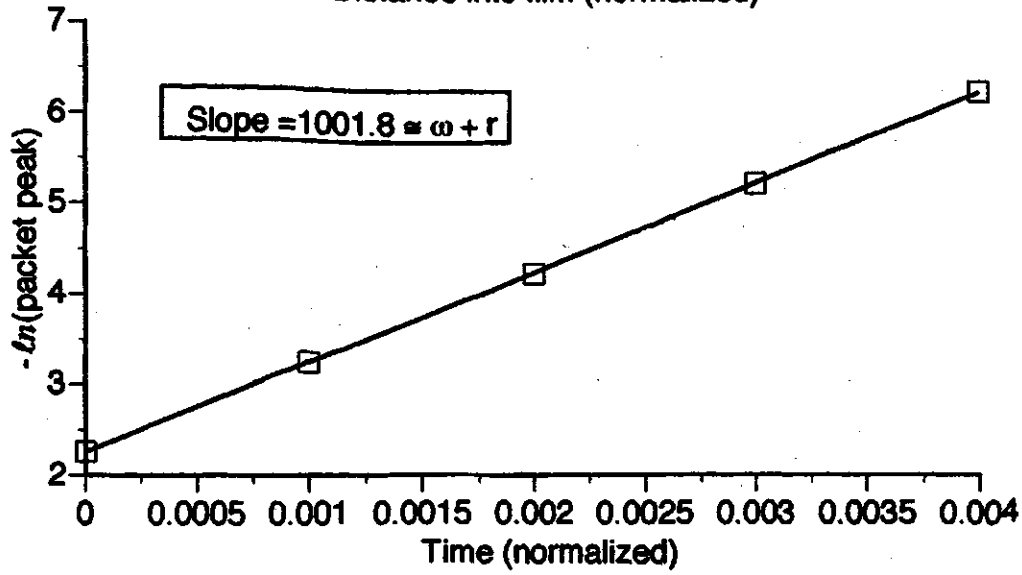

Figure 5.30. Thermalization process under low injection conditions with ω=990, r=10, and δ = 0.01.

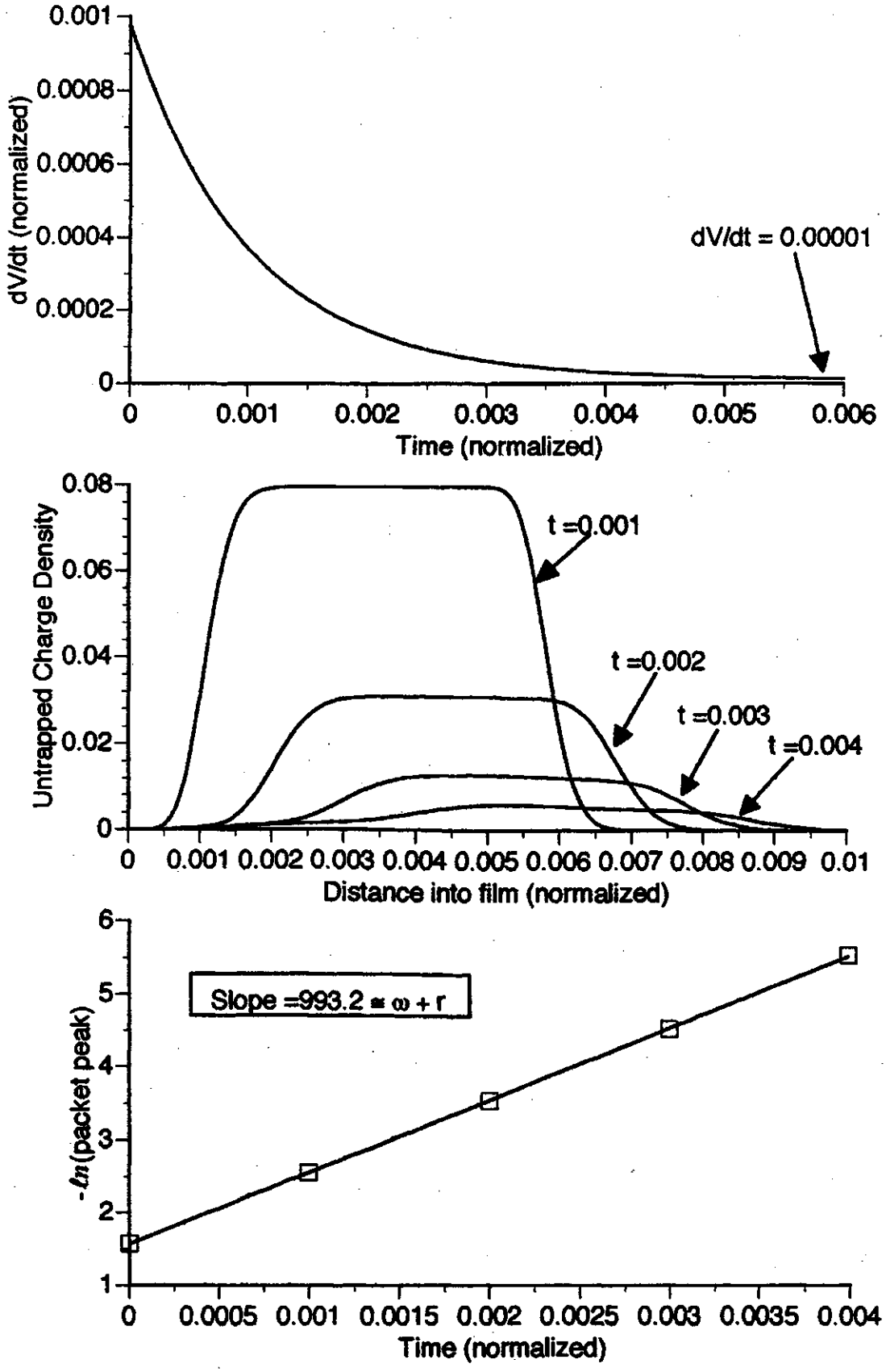

Figure 5.31. Thermalization process under low injection conditions with ω=990, r=10, and δ = 0.005.

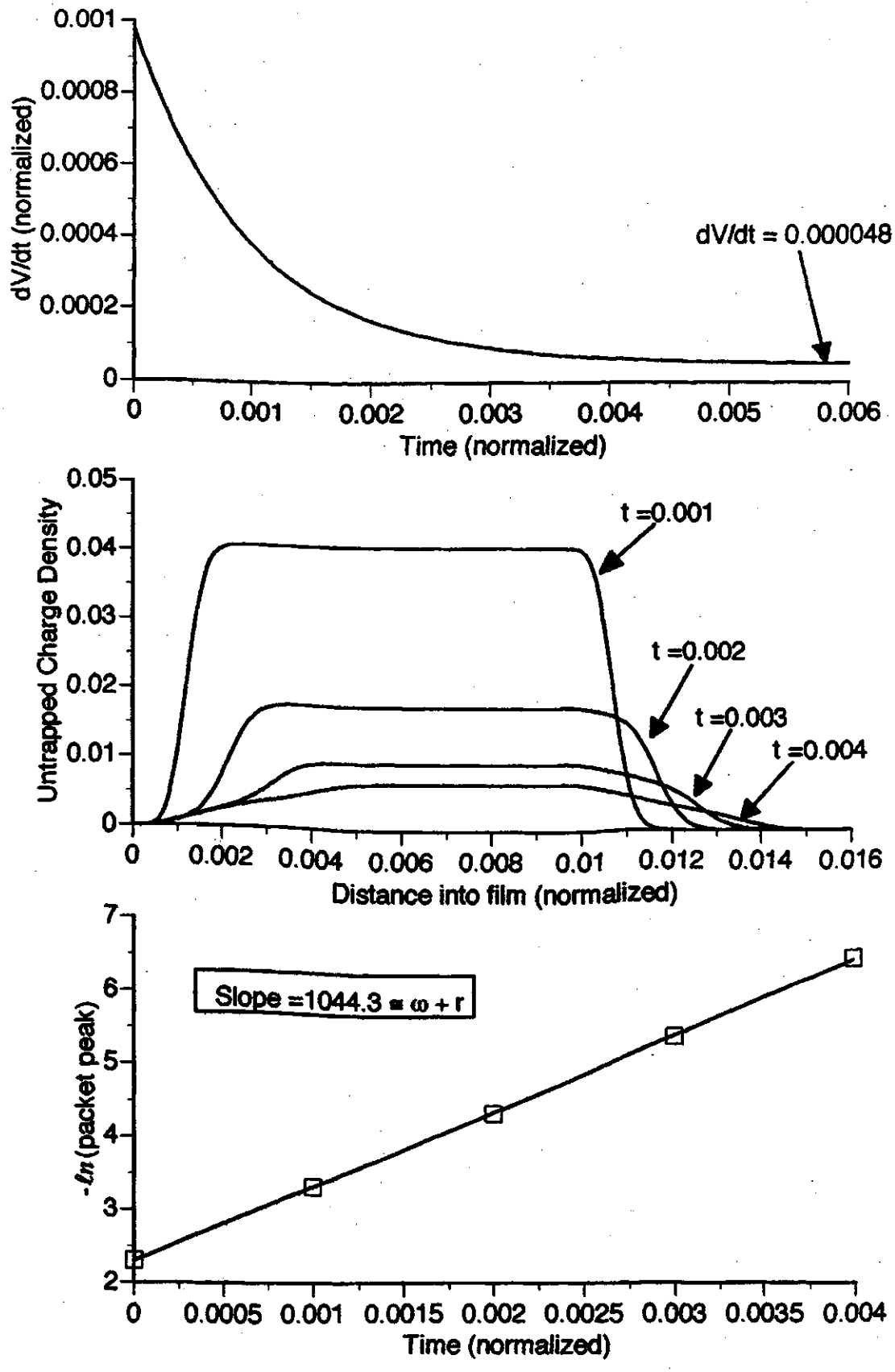

Figure 5.32. Thermalization process under low injection conditions with ω=990, r=50, and δ = 0.01.

thermalization process. It has already been established that the time constant of this process is approximately equal to $1/(\omega+r)$. Therefore, we would expect the width of the post-thermalization packet to be larger for smaller values of ω and r. This prediction can be confirmed visually by comparing two extreme cases, which are shown in Figures 5.28 and 5.30. These results are obtained with $\omega = 90$, r=10 and $\omega = 990$, r=10, respectively. Note that in the case of ω=990, the injected packet does not move very far before it becomes thermalized. In the case of ω=90, however, we saw that the unthermalized packet moved a fair distance before becoming completely thermalized.

The simplified thermalization model presented earlier predicted that the thermalization process would obey an exponential law similar to the one given in Equation 5.18. This assertion can be tested by plotting the natural logarithm of the packet peak value minus the steady state packet peak value versus time. These plots are shown at the bottom of Figures 5.28 through 5.32. The slope of a straight line run through the points is shown in each of the figures. In each case, the slope is approximately equal to $-(\omega+r)$, as expected. The slopes are in better agreement in cases where thermalization occurs more quickly, i.e. where $\omega+r$ is larger. This can be explained by recalling that the simplified analysis presented earlier did not take spatial effects in account. If $\omega+r$ is large, the packet does not move very far during thermalization. The packet is essentially thermalized in one position, and spatial effects are minimized. If $\omega+r$ is smaller, however, the packet moves as it thermalizes and spatial effects are not insignificant. This explains why the slopes are not in good agreement for results obtained with ω=90, r=10.

The effect of changing the injection depth parameter δ can be gauged by comparing results obtained with $\delta = 0.01$ to results obtained with $\delta = 0.005$. If the ω and r values are relatively low, as shown in Figures 5.28 and 5.29, changing the injection depth parameter from δ=0.01 to δ=0.005 decreases the width of the unthermalized

packet but does not significantly affect the width of the post-thermalized packet. However, if ω and r are large, as shown in Figures 5.30 and 5.31, decreasing δ has a direct influence on the width of the post-thermalized packet.

In previous discussions, various phenomena have been said to be caused by the thermalization process. The results presented in this section can explain 1) why transit times obtained from simulations with small values of ω and r have transit times that are significantly smaller than the predicted trap controlled transit time of $1/\theta$ (see Table 5.2), 2) why the width of the packet increases with decreasing ω and r, and 3) why the Schmidlin equation and simulation results are in better agreement for small values of ω (see Table 5.4). These three phenomena will be addressed in turn.

It has been shown that smaller values of ω and r cause the unthermalized packet to move farther during the thermalization process. This explains why the transit times are significantly smaller than the predicted value of $1/\theta$ for small values of ω and r. During thermalization, the packet moves with a velocity that is close to unity. This causes the packet to spread out, giving the packet peak less distance to travel before it exits the sample. For larger values of ω and r, the charge thermalizes in a very thin region near the surface, and the charge essentially has to traverse the entire thickness of the film.

The smearing effect that occurs during thermalization also explains why the packet width increases with decreasing ω and r. The unthermalized packet smears over a greater distance if ω and r are small, giving rise to a wider packet width. If ω and r are large, very little smearing takes place, and the packet width is approximately equal to the width of the injected charge packet, which is relatively small. The dependence of post-thermalization packet width on the trapping parameters ω and r and the injection depth δ

is summarized in Table 5.8. The packet width listed is the FWHM of the untrapped charge packet at a normalized time equal to $20/(\omega+r)$.

Table 5.8. FHWM of the untrapped charge packet after thermalization.

Trap Capture Rate, ω	Trap Release Rate, r	Injection Depth, δ	FWHM after thermalization
90	10	0.01	0.0482
90	10	0.005	0.0481
990	10	0.01	0.00947
990	10	0.005	0.00487
990	50	0.01	0.00953

The discrepancy between the Schmidlin equation and results obtained from simulations for large values of ω (refer to Table 5.4) can be explained by these results. Table 5.8 illustrates that the width of the packet is essentially equal to the initial injection depth δ for large values of ω. The Schmidlin analysis assumes an injected charge sheet that is infinitesimally thin. Therefore, results obtained from simulations will have a larger temporal spread because the initial charge distribution has a finite width. For smaller values of ω, however, the post-thermalization packet width is determined by the smearing effect. Since the Schmidlin [14,15] analysis includes this effect, the simulations results are in good agreement with the Schmidlin equation for smaller values of ω and r.

6. SUMMARY AND CONCLUSIONS

The xerographic process is the basis of many modern copying devices, including laser printers and photocopiers. Central to this process is a thin-film device called the photoreceptor. When a copy is being made, this photoreceptor is initially sensitized by charging it with a corona device. The image of the original is then focused on the surface of the photoreceptor. The photoreceptor converts the optical image into an electrostatic image by discharging the surface in regions where light strikes the surface. This phenomena is called photo-induced discharge.

The central characteristics of an ideal photoreceptor are 1) high resistivity in the dark, 2) high conductivity in the presence of light, and 3) reliable manufacturability. Many amorphous materials, amorphous selenium for example, approximate these properties and have been successfully used as xerographic photoreceptors. Their disordered structure allows for ease of manufacture and gives rise to a high dark resistivity. The photoconductive properties of these materials, although not as pronounced as their crystalline counterparts, allow them to be used effectively as xerographic photoreceptors.

Photo-induced discharge is achieved through the following basic steps. First, the surface of the photoreceptor is positively charged using a corona device. The surface of the photoreceptor is then exposed to light.. The light is strongly absorbed in a thin layer located near the surface, generating mobile carriers. This process is called photogeneration. The photogenerated electrons drift towards the surface and cancel out a fraction of the positive surface charge. The photogenerated holes drift through the

photoreceptor towards the metal substrate, thereby discharging the photoreceptor. This process, called transport, is especially important because the speed and efficiency of this process play a large role in determining the performance of the photoreceptor.

The importance of transport process in photoreceptor materials has led to extensive research in this area. In amorphous materials, the transport process has been shown to be greatly affected by the presence of localized trapping centers, which are created by the disordered nature of the material. Various theoretical analyses have been constructed that incorporate the effects of trapping. However, the mathematical complexity of the problem prevents a rigorous and general solution from being obtained. The goal of this work was to create a general computer model that can be used to investigate how trapping affects the characteristics of a photo-induced discharge.

In order to achieve this goal, a detailed understanding of transport mechanisms in amorphous solids is required. The electronic band theory of solids has been very successful in predicting the electronic behaviour of crystalline semiconductors. This theory can also be applied to amorphous semiconductors if the disordered nature of these materials is taken into account. Two bands of extended states, the conduction and valence bands, are still present. However, the disordered nature of these materials creates tails of localized states near the band edges. The presence of significant densities of defects creates defect states deep in the region between the bands. This region, which is called the band gap in the case of crystalline semiconductors, is called the mobility gap because the mobility is reduced but still non-zero for the localized states residing between the bands.

As in crystalline semiconductors, transport primarily takes place in the extended states. The total conductivity is due to the motion of two types of carriers, holes and electrons, which drift in the valence and conduction bands, respectively. The

conductivity in the extended states is determined by the hole and electron carrier densities and mobilities. The conductivity in amorphous materials is much lower than in crystalline materials because the mobilities and thermally governed carrier densities are much lower. This gives rise to a high dark resistivity, which allows these materials to be used as photoreceptors.

Light incident on the surface of a photoreceptor increases the carrier densities in the extended states by generating electron-hole pairs. If the photoreceptor is positively charged, the electrons immediately travel to the surface and cancel out the positive charge. The holes drift towards the substrate, thereby discharging the photoreceptor. As they drift, they interact with the tail and defect localized states located in the mobility gap. These localized states are called "traps" because they can temporarily capture a carrier and prevent it from drifting. Traps created by the localized tail states are called shallow traps. Traps created by the defect states located deep in the mobility gap are called deep traps.

Associated with each type of trap, shallow and deep, are a capture and release lifetime. The shallow trap capture and release lifetimes are much shorter than the time scale of the discharge, causing the carrier be captured and released many times as it traverses the photoreceptor. This has the effect of reducing the apparent mobility by an amount given by

$$\theta = \frac{t_c}{t_c + t_r} \tag{6.1}$$

This has the effect of increasing the discharge time by a factor of $1/\theta$. Deep traps have much longer release lifetimes because they lie deeper in the mobility gap. The release time of deep traps is often much longer than the time scale of the discharge. Therefore, carriers captured by deep traps are often viewed as being permanently trapped when viewed against the time scale of the discharge. This permanently trapped charge

prevents the photoreceptor from fully discharging. Instead, the surface voltage discharges to a value known as the residual potential. If the photoreceptor manufacturing process is not well controlled, the number of deep traps can become too large and the residual potential will be too large for the sample to be usable.

The band theory interpretation of photo-induced discharge can be used to construct detailed mathematical models of photo-induced discharge in the presence of trapping. If the incident light is assumed to be strongly absorbed, electron transport can be neglected. Also, the number of thermally generated carriers can be neglected at room temperature. These assumptions imply that only photogenerated holes need to be considered. If the film properties are assumed to be homogeneous, a one-dimensional model can be used. If only one set of traps is considered, a relatively simple theoretical model of photo-induced discharge can be constructed.

Several theoretical models based on these assumptions exist in the literature. These models are obtained by considering the detailed relationships between the charge densities, the conduction current, and the electric field. These relationships are given by the one-dimensional point form versions of Ohm's Law, Gauss' Law, and Maxwell's equation for the total current. The interaction between the single level of traps and the extended states is described by a trapping rate equation, which describes the relationship between the trapped and untrapped charge densities. Kanazawa and Batra [8] presented an analytical solution to these equations that considered capture into a single set of traps under weak illumination conditions. The trapping rate equation used in this model, however, neglected the effects of release and trap saturation. A later model described by Okuda et al. [7] incorporated of release. The model presented by Kasap et al., uses a complete form of the rate equation which includes trapping, release, and trap filling. It provides a complete description of photo-induced discharge in the presence of a single set of traps. This model is the basis of this work.

Algebraic manipulation of Ohm's Law, Gauss' Law, Maxwell's equation for the total current, and the trapping rate equation presented by Kasap et al. results in a second order partial differential equation for the electric field. This equation, which contains the trapping parameters ω, r, and c as parameters, can be solved using suitable boundary and initial conditions and a numerical solution algorithm, both of which are described in detail in this work. Boundary and initial conditions for the cases of weak step illumination and pulse illumination have been presented. The weak step illumination case is of interest because it is often used in experimental arrangements in an attempt to determine material properties. The pulsed illumination case, also called Xerographic Time-of-Flight (XTOF), is of more interest however, because this is the scenario used in practical devices such as laser printers. In this case, the time scale of the discharge is solely dependent on trapping effects and the intensity of the light source, which determines the amount of injected charge. In particular, there is great interest in modeling the characteristics of photo-induced discharge in the presence of trapping and under extremely high injection conditions, because little work has been done in this area. This topic has been examined in this work.

In order to obtain a numerical solution to the PID differential equation, a grid is superimposed over the (x,t) domain. The derivatives at the grid points can be approximated in terms of the electric field values at neighboring grid points using the forward and backward Euler approximations. If the resolution of the grid is chosen appropriately, the error in these approximations will be marginal. The approximations can then be substituted into the PID differential equation, reducing it to a difference equation. This difference equation can then be applied to every point in the grid, starting from the grid boundaries. This yields a complete solution for the electric field, E(x,t), over the entire grid. Other quantities, such as the surface voltage and the trapped and

untrapped charge densities can then be calculated from this data, allowing a comprehensive analysis of the discharge.

Two methods based on this approach have been described in detail in this work. The first method, called the hybrid method, is constructed using both the forward and backward Euler approximations. This method has been used successfully in previous work[10, 13]. However, it has been found to be unstable under extremely high injection conditions. To address this problem, a second method called the cubic method has been devised by the author. This method, which is based solely on the backward Euler approximation, has been found to be stable under high injection conditions. Results obtained using both methods have been presented in this work.

The results presented in this work were divided in three categories: low injection, high injection, and thermalization. The low injection scenario is of importance because it is representative of XTOF experiments performed on xerographic materials. It also allows an unbiased examination of the effects of trapping, as injection related effects will not be significant. The high injection case is of interest because it is representative of practical situations where very intense beams are used. Thermalization results are those obtained at the very beginning of the discharge. These are important because thermalization explains a variety of phenomena observed in the low injection results, such as the dispersion of the injected charge packet.

The relationship between the shape, charge content, velocity of the charge packets and the rate of decay of the surface voltage was established. It was shown that the rate of decay before the transit time is given by $(1-\varphi)v_p$ if the entire packet moves with a constant velocity equal to v_p. The width or dispersion in dV/dt near the trap controlled transit time was shown to be directly related to the width of the charge packet as it exits the sample.

Results obtained under low injection (0.1%) conditions were presented. Values for the capture and release rates ω and r were selected that are representative of shallow traps. Trap saturation was neglected. The values of ω and r were selected to allow an examination of the effect of changing the mobility reduction factor θ and the magnitude of the trapping parameters. The packet velocity was found to be in excellent agreement with the mobility reduction factor. The transit time was found to be in good agreement with $1/\theta$ for large values of ω and r. Smaller values of ω and r caused the transit time to be as much as 5% smaller than the value predicted by $1/\theta$. This fact was said to be due to thermalization effects. The pre-transit time value of dV/dt was found to be in excellent agreement with the value of $\theta(1-\varphi)$, confirming the analytically established relationship between the charge densities and dV/dt.

The dependence of the width of the charge packet and hence the dispersion of dV/dt on ω, r, and θ was examined. The % dispersion in dV/dt was found to increase with increasing values of θ. It was also found to increase with decreasing values of ω and r if θ was held constant. An explanation for the dependence of packet width and dV/dt dispersion on θ was obtained by considering the statistical nature of the trapping process. It was hypothesized that the rate of dispersion with respect to time is proportional to the mobility reduction factor. This implies that the rate of dispersion with respect to distance is constant. This fact was confirmed by plotting the rate of packet growth with distance for various values of θ. The rate of packet growth was seen to be the same for all values of θ, confirming the hypothesis. It was also found that the rate of packet growth with distance did not depend on the values of ω and r chosen. This observation, however, did not explain why smaller values of ω and r yield greater absolute dispersion. This fact is explained by the effects of thermalization.

The dispersion in dV/dt was also characterized by examining the FWHM of its derivative, d^2V/dt^2. Results obtained using this method were compared to the Schmidlin

equation, which predicts the temporal spread in charge arrival times as a function of the trap capture and release lifetimes. The simulations results were found to be in excellent agreement with the Schmidlin equation for small values of ω and r. Larger values of ω and r were in poorer agreement. This was shown to be due to the finite width of the initial charge packet.

Results obtained under high injection conditions were presented. Injection strengths of 10%, 50%, and 99% were used. The effects of changing the capture and release rates, ω and r, were examined. The effect of trap saturation under high injection conditions was examined by using non-zero values of the trap saturation constant, c.

The dispersion in dV/dt was seen to increase dramatically as the injection was increased. This is because the packet is moving primarily due to its self-field under high injection conditions. The field seen by the leading edge of the packet is much higher than the field at the trailing edge, causing the leading edge to move at a higher average velocity. This causes the packet to spread significantly, creating significant dispersion in dV/dt. Also, since different portions of the packet are not traveling at the same velocity, the pre-transit time of dV/dt is not given by $\theta(1-\varphi)$. However, dV/dt still starts to drop near the transit time predicted by $1/\theta$. This is because the leading edge of the packet sees the full field, and hence travels at a velocity given by θ.

As in the low injection case, the dispersion was seen to increase with increasing values of θ and with decreasing values of ω and r. At extremely high injection levels, the effect of trapping on dispersion was seen to be small in comparison with the portion caused by the amount of injection. This allows one to conclude that the effects of shallow trapping are not as significant under high injection conditions.

The effect of increased trap saturation was investigated by setting the trap saturation parameter c equal to 1, 5, and 10. As the parameter was increased, the peak

value of the charge packets was seen to decrease and the packet was seen to become flatter and more spread out. This is because the number of available traps at a given position is finite for any non-zero value of c. Once the traps become filled at a given position, the remaining untrapped charge moves forward to a position where more traps are available. This causes the packet to become more spread out with increasing values of c. This behaviour was reflected in the pre-transit time behaviour of dV/dt. Significant decay in dV/dt was observed before the transit time for large values of c. This is because it takes more time for the untrapped charge to come into equilibrium with the traps under high saturation conditions. The post transit-time behaviour of dV/dt was not seen to be greatly affected by the trap saturation parameter. This is because most of the charge packet dispersion is caused by the large amount of injection.

The thermalization process that occurs at the beginning of the discharge was investigated under low injection conditions. A simplified analytical model of the thermalization process was obtained by neglecting trap saturation and variation with distance. This analysis predicted that the untrapped charge would decrease exponentially with a rate given by $\omega+r$. This predicts that the thermalization time will be smaller for larger values of ω and r. The validity of this analysis was tested by performing simulations of the thermalization region for various values of ω and r. Also, different values for the injection depth parameter δ were used to gauge the effect of injection depth.

The simplified thermalization analysis was tested by plotting the untrapped packet peak value as a function of time. An exponential fit to this data confirmed that the rate of decay is approximately equal to $\omega + r$. The decay rate was in better agreement when the decay was swift enough to cause the packet to thermalize in place. This condition is met for larger values of ω and r. The width of the charge packet after thermalization was found to be proportional to the length of the discharge because the

packet moves as it thermalizes. This implies that the post-thermalization packet width will increase with decreasing ω and r. This result explains why low injection results obtained with lower values of ω and r have more dispersion. For large values of ω and r, the post-thermalization packet width was seen to be approximately equal to the initial injection depth, δ. This result explains why the Schmidlin equation predicts a smaller spread in the charge arrival times for larger values of ω and r, since the Schmidlin analysis assumes an infinitesimal initial packet width.

6.1 Suggestions for Future Work

The characteristics of photo-induced discharge under a wide range of conditions have been investigated in this work. However, some scenarios have not been fully addressed or have been omitted entirely. The effects of trap saturation under high injection conditions have been examined, but have not been exhaustively investigated. An investigation of the thermalization process under high injection conditions and in the presence of trap saturation would provide more insight into the mechanics of the discharge under these conditions.

The trapping and release rates chosen in this work were representative of shallow traps, i.e. the carrier was trapped and released many times throughout the course of the discharge. Parameters representative of deep traps were not considered. This situation is also of interest, because the amount of charge remaining in deep traps at the end of the discharge determines the value of the residual potential, V_r, which is an important xerographic parameter. It would be instructive to perform simulations with trapping parameters that are typical of deep traps under high injection conditions and in the presence of trap saturation. Trap saturation is of particular interest because the concentration of deep traps is directly related to the defect density. This would allow a

direct examination of how the defect density affects the characteristics of the discharge and the value of the residual potential.

The ω and r values chosen in this work were selected arbitrarily to allow an examination of how the magnitude of the trapping parameters affects the characteristics of the discharge. No attempt to make these parameters representative of specific materials was made. If ω and r were chosen with a particular material in mind, the simulation results could be directly compared to experimental results.

The theoretical model presented in this work only considers the effect of a single level of traps. This model is somewhat limiting in that it does not allow shallow and deep traps to be modeled simultaneously. If deep traps are being modeled, shallow traps can be incorporated using the mobility reduction factor. However, this work has demonstrated that this is only a valid approximation under certain circumstances. A two-trap model would allow a simultaneous examination of deep and shallow traps.

7. REFERENCES

[1] Mort J., *The Anatomy of Xerography: Its Invention and Evolution*, McFarland & Company Inc., Jefferson, 1989, pp. 48-83.

[2] Madan A. and Shaw M. P., *The Physics and Applications of Amorphous Semiconductors*, Academic Press Inc., San Diego, 1988, pp. 4-10, 471-476.

[3] Warter P. J., "Factors Determining Xerographic Photoreceptor Performance", Applied Optics:Supplement 3, on Electrophotography, 1969, pp. 65-75.

[4] Schaffert R. M., *Electrophotography*, Focal Process, London, 1975, pp. 278-285.

[5] Anderson D. A., Acta Chem. Scand., **8**, 1959, pp. 1599.

[6] Kasap S. O., *Principles of Electrical Engineering Materials and Devices*, Irwin McGraw-Hill, Boston, 1997, pp. 106-109, 315-316.

[7] Okuda M., Motomura K., Naito H., Matsushita T., and Nakua T., "A Theoretical Investigation of the Residual Voltage on Electrophotographic Plates", Japanese J. of Appl. Phys., **21**, 1982, pp. 1127-1134.

[8] Kanazawa K. K. and Batra I. P., "Deep-Trapping Kinematics", J. Appl. Phys., **43**, 1972, pp. 1845-1853.

[9] Kasap S.O., Aiyah V., Polischuk B., Bhattacharyya A., and Liang Z, "Deep-trapping kinematics of charge carriers in amorphous semiconductors: A theoretical and experimental study", Phys. Rev. B, **43**, No. 8, 1991, pp. 6691-6705.

[10] Kasap S.O., "Charge-carrier deep-trapping kinetics in high-resistivity semiconductors", J. Phys. D: Appl. Phys., **25**, 1992, pp. 83-93.

[11] Kasap S.O., Bhattacharyya A. and Liang Z., "Decay of Electrostatic Surface Potential on Insulators via Charge Injection, Transport and Trapping", Jpn. J. Appl. Phys., **31**, 1992, pp. 72-80.

[12] Strang G., *Introduction to Applied Mathematics*, Wellesley-Cambridge Press, Wellesley, 1986, pp. 562-564.

[13] Liang Z., M. Sc. Thesis, *Computation of the Electrostatic Field in Photoreceptors During Photodischarge*, University of Saskatchewan, Saskatoon, Canada, 1991.

[14] Schmidlin F. W., "Theory of trap-controlled transient photoconduction", Physical Review B, **16**, 1977, pp. 2352-2385.

[15] Schmidlin F.W., "Theory of multiple trapping", Solid State Communications, **22**, 1977, pp. 451-453.

APPENDIX A

ANALYTICAL METHOD USED TO FIND THE ROOTS OF A CUBIC EQUATION

A.1 Analytical Method

Consider a cubic equation of the form given by equation

$$AE_{l,m}^3 + BE_{l,m}^2 + CE_{l,m} + D = 0 \tag{A.1}$$

Dividing by A and letting $x=E_{l,m}$ gives a general cubic equation of the form:

$$x^3 + a_2x^2 + a_1x + a_0 = 0 \tag{A.2}$$

Where $a_0 = D/A$, $a_1 = C/A$, and $a_2 = B/A$. This equations has three roots x_1, x_2, x_3, given by:

$$x_1 = (s_1 + s_2) - \frac{a_2}{3} \tag{A.3}$$

$$x_2 = -\frac{1}{2}(s_1 + s_2) - \frac{a_2}{3} + \frac{j\sqrt{3}}{2}(s_1 - s_2) \tag{A.4}$$

$$x_3 = -\frac{1}{2}(s_1 + s_2) - \frac{a_2}{3} - \frac{j\sqrt{3}}{2}(s_1 - s_2) \tag{A.5}$$

where

$$s_1 = \sqrt[3]{r + \sqrt{q^3 + r^2}} \tag{A.6}$$

$$s_2 = \sqrt[3]{r - \sqrt{q^3 + r^2}} \tag{A.7}$$

$$q = \frac{1}{3}a_1 - \frac{1}{9}a_2^2 \tag{A.8}$$

$$r = \frac{1}{6}(a_1 a_2 - 3a_0) - \frac{1}{27}a_2^3 \tag{A.9}$$

Since x in this case represents a normalized physical quantity ($E_{l,m}$), we only need the real roots. Equations (A.3) through (A.9) can give one, two, or three real roots, depending on the value of the determinant, $q^3 + r^2$. Three cases for the determinant are considered below:

i) $q^3+r^2 > 0$

In this case, there is one real root and two complex-conjugate roots. The real root is given by Equation (A.3)

$$x_1 = (s_1 + s_2) - \frac{a_2}{3} \tag{A.3}$$

ii) $q^3+r^2 = 0$

Here, there are two real roots given by

$$x_1 = (s_1 + s_2) - \frac{a_2}{3} = 2 \cdot \sqrt[3]{r} - \frac{a_2}{3} \tag{A.3}$$

$$x_1 = (s_1 + s_2) - \frac{a_2}{3} = -\sqrt[3]{r} - \frac{a_2}{3} \tag{A.3}$$

iii) $q^3+r^2 < 0$

Here, there are three real roots given by Equations (A.3) through (A.5).